Applied Research Laboratory

DTIC FILE COPY

Technical Report

INFLUENCE OF PROCESS PARAMETERS
ON LASER WELD CHARACTERISTICS
IN ALUMINUM ALLOYS

by

Nagesh Sonti

DTIC
ELECTE
AUG 1 9 1988
S   D
    H

PENNSTATE

1 8 5 5

88 8 17

The Pennsylvania State University
APPLIED RESEARCH LABORATORY
P. O. Box 30
State College, PA   16804

INFLUENCE OF PROCESS PARAMETERS
ON LASER WELD CHARACTERISTICS
IN ALUMINUM ALLOYS

by

Nagesh Sonti

DTIC

S ELECTED

AUG 1 9 1988

H

Technical Report No. TR 88-011

August 1988

N00024-85-C-6041

L. R. Hettche, Director
Applied Research Laboratory

Unclassified

A197 29?

SECURITY CLASSIFICATION OF THIS PAGE

REPORT DOCUMENTATION PAGE

1a. REPORT SECURITY CLASSIFICATION Unclassified		1b. RESTRICTIVE MARKINGS			
2a. SECURITY CLASSIFICATION AUTHORITY		3. DISTRIBUTION / AVAILABILITY OF REPORT Unlimited			
2b. DECLASSIFICATION / DOWNGRADING SCHEDULE					
4. PERFORMING ORGANIZATION REPORT NUMBER(S)		5. MONITORING ORGANIZATION REPORT NUMBER(S)			
6a. NAME OF PERFORMING ORGANIZATION Applied Research Laboratory The Pennsylvania State University	6b. OFFICE SYMBOL (If applicable) ARL	7a. NAME OF MONITORING ORGANIZATION Naval Sea Systems Command Department of the Navy			
6c. ADDRESS (City, State, and ZIP Code) P. O. Box 30 State College, PA 16804		7b. ADDRESS (City, State, and ZIP Code) Washington, DC 20362			
8a. NAME OF FUNDING / SPONSORING ORGANIZATION Naval Sea Systems Command	8b. OFFICE SYMBOL (If applicable) NAVSEA	9. PROCUREMENT INSTRUMENT IDENTIFICATION NUMBER			
8c. ADDRESS (City, State, and ZIP Code) Department of the Navy Washington, DC 20362		10. SOURCE OF FUNDING NUMBERS			
		PROGRAM ELEMENT NO.	PROJECT NO.	TASK NO.	WORK UNIT ACCESSION NO.

11. TITLE (Include Security Classification)
Influence of Process Parameters on Laser Weld
Characteristics in Aluminum Alloys

12. PERSONAL AUTHOR(S)
Nagesh Sonti

13a. TYPE OF REPORT Ph.D. Thesis	13b. TIME COVERED FROM ___ TO ___	14. DATE OF REPORT (Year, Month, Day) August 1988	15. PAGE COUNT 177

16. SUPPLEMENTARY NOTATION

17. COSATI CODES			18. SUBJECT TERMS (Continue on reverse if necessary and identify by block number)
FIELD	GROUP	SUB-GROUP	aluminum alloy welding, CO_2 laser welding, numerical modeling, weld defects

19. ABSTRACT (Continue on reverse if necessary and identify by block number)

Multi-kilowatt CO_2 lasers are increasingly being used for welding applications
due to their capability of producing deep penetration welds at high welding speeds.
Although most metals are being successfully welded, laser welding of aluminum
alloys is proving to be very difficult. Combination of high thermal diffusivity
and optical reflectivity to CO_2 laser radiation causes difficulty in coupling the
laser energy to the material. Much higher laser intensities are required to ensure —

20. DISTRIBUTION / AVAILABILITY OF ABSTRACT ☒ UNCLASSIFIED/UNLIMITED ☐ SAME AS RPT. ☐ DTIC USERS	21. ABSTRACT SECURITY CLASSIFICATION Unclassified	
22a. NAME OF RESPONSIBLE INDIVIDUAL	22b. TELEPHONE (Include Area Code)	22c. OFFICE SYMBOL

DD FORM 1473, 84 MAR 83 APR edition may be used until exhausted. All other editions are obsolete.

SECURITY CLASSIFICATION OF THIS PAGE
Unclassified

coupling and to form the keyhole, than to maintain the keyhole and obtain smooth fusion, as absorption of laser energy improves dramatically with the keyhole formation. Laser welds in aluminum alloys contain extensive porosity, and excessive vaporization of alloying elements occurs from the fusion zone. The welds have severe undercuts and large discontinuous cavities on the bead surface. A more precise control of the weld heat input and a better understanding of the influence of process parameters and the alloying content on the weld characteristics is required to improve the laser weldability of aluminum alloys.

High power laser welds in aluminum alloys were characterized in terms of the weld shape and dimensions, the nature and amount of porosity, loss of elements from the fusion zone, and the microstructures in and around the welds. A two-dimensional finite element heat conduction model was developed to numerically simulate the melting and solidification phenomena in keyhole laser welds. Significant variations in weld dimensions were observed among the different aluminum alloys with marked difference in the welding process efficiencies. The magnesium containing 5xxx series alloys showed the highest weld penetrations, as well as periodic variation in the penetration along the weld length, evidently caused by an unstable and oscillating keyhole. Alloy 2219 contained large shrinkage cavities in the welds, but showed the minimum amount of voids among the alloys investigated. Laser welds in the 5xxx series alloys had excessive amount of spherical porosity and large irregular shaped cavities. Significant vaporization of magnesium and aluminum from the weld, and the entrapment of parts of the unstable cavity in the solidifying metal, are believed to cause the excessive amount of voids observed in the 5xxx series alloys.

ABSTRACT

Multi-kilowatt CO_2 lasers are increasingly being used for welding applications due to their capability of producing deep penetration welds at high welding speeds. Although most metals are being successfully welded, laser welding of aluminum alloys is proving to be very difficult. Combination of high thermal diffusivity and optical reflectivity to CO_2 laser radiation causes difficulty in coupling the laser energy to the material. Much higher laser intensities are required to ensure coupling and to form the keyhole, than to maintain the keyhole and obtain smooth fusion, as absorption of laser energy improves dramatically with the keyhole formation. Laser welds in aluminum alloys contain extensive porosity, and excessive vaporization of alloying elements occurs from the fusion zone. The welds have severe undercuts and large discontinuous cavities on the bead surface. A more precise control of the weld heat input and a better understanding of the influence of process parameters and the alloying content on the weld characteristics is required to improve the laser weldability of aluminum alloys.

High power laser welds in aluminum alloys were characterized in terms of the weld shape and dimensions, the nature and amount of porosity, loss of elements from the fusion zone, and the microstructures in and around the welds. A two-dimensional finite element heat conduction model was developed to numerically simulate the melting and solidification phenomena in keyhole laser welds. Significant variations in weld dimensions were observed among the different aluminum alloys with marked difference in the welding process efficiencies. The magnesium containing 5xxx series alloys showed the highest weld penetrations, as well as periodic variation in the penetration along the weld length, evidently caused by an unstable and oscillating keyhole. Alloy 2219 contained large shrinkage

cavities in the welds, but showed the minimum amount of voids among the alloys investigated. Laser welds in the 5xxx series alloys had excessive amount of spherical porosity and large irregular shaped cavities. Significant vaporization of magnesium and aluminum from the weld, and the entrapment of parts of the unstable cavity in the solidifying metal, are believed to cause the excessive amount of voids observed in the 5xxx series alloys.

QUALITY INSPECTED 2

Accession For

NTIS GRA&I	☑
DTIC TAB	☐
Unannounced	☐
Justification	

By
Distribution/
Availability Codes
Avail and/or
Dist   Special

A-1

TABLE OF CONTENTS

TABLE OF CONTENTS (continued)

TABLE OF CONTENTS (continued)

LIST OF TABLES

LIST OF FIGURES

LIST OF FIGURES (continued)

LIST OF FIGURES (continued)

ACKNOWLEDGEMENTS

I wish to express my sincere gratitude to Professor Maurice F. Amateau for giving me the opportunity to work on this project. His support, guidance and advice during this research program have been invaluable.

I also wish to thank my doctoral committee members – Professors Richard P. McNitt, Joseph C. Conway, Richard A. Queeney, and Tarasankar DebRoy – for their advice and comments throughout the course of the investigation. My thanks are also due to all the members of the Engineering Materials Department at Applied Research Laboratory for their suggestions and help during the study.

Finally, I deeply appreciate the sacrifices that my family has so patiently endured through these long years of my education.

Chapter 1

INTRODUCTION

Multi-kilowatt CO_2 lasers are increasingly being used for welding applications because of their capability of producing deep penetration welds at high welding speeds. The advantages of laser welding over the comparable electron beam welding are that welding can be carried out without vacuum and without the generation of x-rays, and that the raw laser beam can be optically transported and shared by different work-stations. For power levels up to 5 kw, laser welding is also more economical than electron beam welding.[1] However, weld penetrations in laser welding have been significantly lower than in electron beam welding.

CO_2 lasers generate radiation at 10.6 micron wavelength in the infrared range. Two techniques of laser welding are possible – conduction mode and keyhole mode of welding. In the conduction mode, limited to thin-section welding, melting of the metal occurs by the absorption of laser radiation on the plate surface and heat conduction into the material. In the keyhole mode for deep penetration welding at higher intensities, a vapor column or a keyhole is formed in the material as shown in figure 1.1.[2] The vapor column is in hydrodynamic equilibrium with the surrounding molten metal, and as the material is traversed relative to the laser beam, molten metal flows via the sides of the column to the rear of the weld pool where solidification occurs.

1.1 Factors Affecting Aluminum Laser Weldability

Although most metals are being successfully welded using the laser beam, aluminum alloys have proved to be very difficult to laser weld.[3] These alloys combine high thermal diffusivity with high optical reflectivity to CO_2 laser
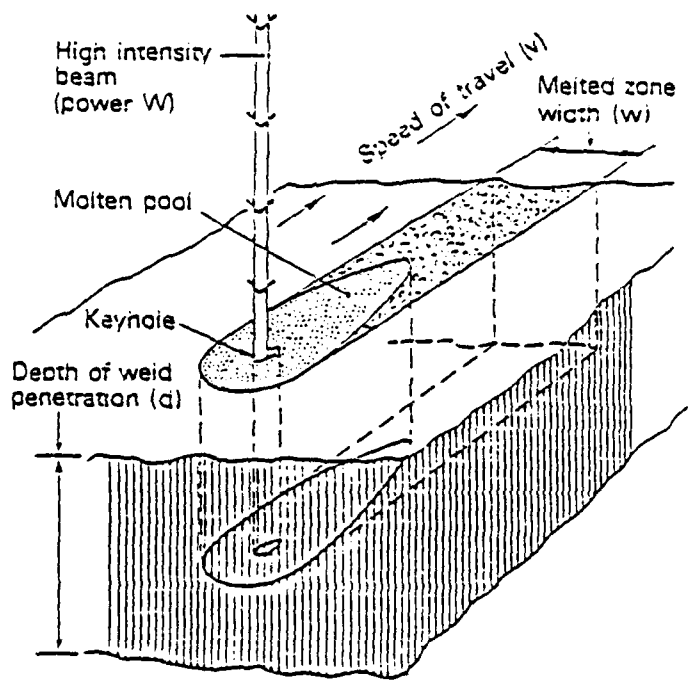
Figure 1.1   Keyhole mode of welding at high laser power
intensity.[2]

radiation, causing difficulty in coupling the laser energy to the material. Reflectivity of aluminum at 10.6 micron wavelength is over 95% as seen in figure 1.2.[4] Although reflectivity decreases with increase in temperature, the change is minimal for aluminum alloys as shown in figure 1.3.[5] To ensure coupling, much higher intensities are required for aluminum alloys than for steels, and at such intensities, welding occurs in the keyhole mode. However, absorption of laser energy improves dramatically with the keyhole formation due to the black body absorption characteristics of the cavity by way of multiple reflections (see figure 1.4).[6] Thus, much higher laser intensities are required to ensure coupling and to form the keyhole, than to maintain the keyhole and obtain smooth fusion.

Laser welds in aluminum alloys are prone to extensive porosity. Aluminum welds in general are prone to porosity caused by the differential solubility of hydrogen between the molten and the solidified metal.[7] Porosity in arc welds can be avoided with proper surface cleaning procedures to remove any sources of hydrogen.[8] However, such precautions have not reduced the excessive porosity observed in aluminum laser welds. Further, laser welds in these alloys have severe undercuts and, in some cases, large discontinuous cavities on the weld bead surface.[9,10] In addition, significant amount of vaporization of elements occurs from aluminum laser welds which in turn affects the weld microstructures and the mechanical properties of the weldments.[11] Presence of volatile alloying elements like magnesium and zinc can further influence the weld metal characteristics in the vaporization dominated keyhole mode.

Due to the poor laser weldability of aluminum alloys, not much information is available on the influence of laser welding parameters on weld bead shape and dimensions, nature, amount and distribution of porosity, loss of elements due to vaporization, etc. A detailed parametric study is therefore necessary to gain a
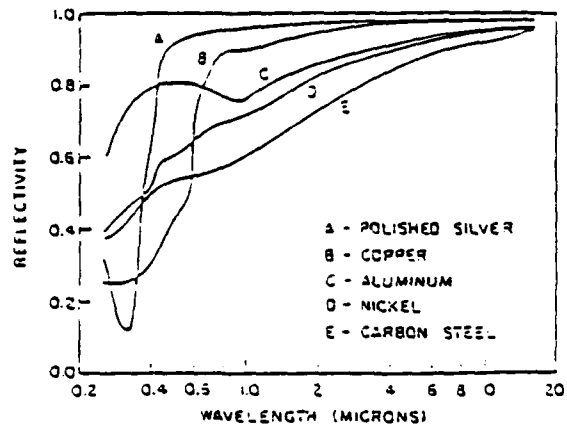
Figure 1.2   Reflectivity of metals as a function of
wavelength.[4]
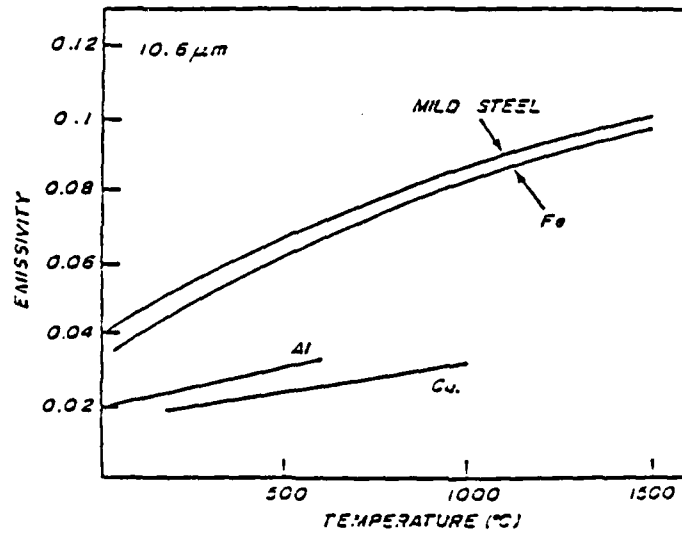
Figure 1.3   Emissivity of metals as a function of
temperature.[5]
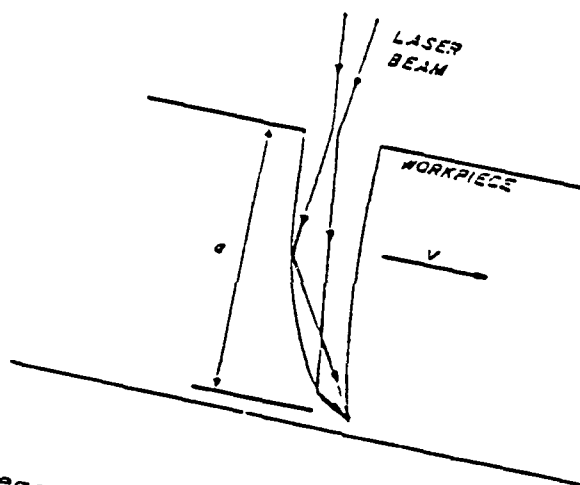
Figure 1.4 Increase in absorption of laser energy in the keyhole mode due to multiple reflections.6

better understanding of the problems involved in order to improve the quality of aluminum laser welds with improved process controls.

Further, predictive models analyzing the thermal behavior of aluminum laser welds can be very helpful in understanding the role of welding heat input parameters on the final weld bead characteristics. In the thermal energy balance, the convective terms can significantly influence the temperature profiles. However, Oreper and Szekely[12] have shown that for buoyancy dominated fluid flows at low Reynold's number, the convective terms may be neglected without unduly affecting the weld thermal profiles. The laser welds in aluminum alloys were generally found to satisfy such conditions, and heat conduction analysis is adequate to reliably predict the weld profiles. In laser welding, there is also the phenomenon of plasma generation at the plate surface.[13] The plasma formation can result in partial absorption of the laser energy. However, the influence of the plasma and its interaction with the laser beam and the material is not yet well understood. Its effect on the welding process is empirically incorporated in the form of overall absorptivity of the material.

Surface heat sources have been effectively used for the numerical simulation of arc welding processes.[14] However, these sources are not valid for deep penetration electron beam and laser welding where the energy is deposited deep inside the keyhole. In electron beam welding with high aspect ratios (ratio of weld penetration to top bead width), cylindrical heat source models of constant temperature boundaries[15,16] have been used. Mazumder et al.[17] and Chande et al.[18] have attempted the simulation of the keyhole using the Beer-Lambert's law using an absorptivity coefficient. Other researchers have used the weld profile to adjust the welding heat source distribution for the modeling. For instance, Goldak et al.[19,20] used a model with up to eight parameters which were selected based on

the experimental weld geometry. Further research is required both on the physical phenomenon of energy transfer in laser welds as well as the numerical simulation of keyhole laser welds.

1.2 Objectives

Aluminum alloys are very sensitive to high energy intensity, but require such an intense laser beam to ensure coupling and form the keyhole. The energy input at various stages of the laser weld cycle must be optimised to improve the quality of laser welds in aluminum alloys. Present investigation was therefore conducted to study the influence of process parameters on the laser weld characteristics in aluminum alloys. Following were the main objectives of the investigation :

i. To characterize the bead shape and dimensions of laser welds in aluminum alloys in terms of the weld penetration, top bead width, aspect ratio, weld cross-sectional area and the process efficiency for the different welding conditions.

ii. To develop a two-dimensional non-linear transient finite element heat conduction model for simulating the melting and solidification phenomena in keyhole laser welds.

iii. To predict the laser weld pool dimensions in aluminum alloys using the finite element heat conduction model developed.

iv. To characterize the nature, amount and distribution of porosity in laser welds in aluminum alloys in terms of the input power, power intensity, welding speed as well as the alloying content.

v. To analyze the laser welds in aluminum alloys with regards to the vaporization of alloying elements and the microstructures in and around the welds.

Aluminum alloys 2219, 5083, 5456 and 6061 were studied considering their good weldability by conventional arc welding processes.

1.3 Scope and Outline of Thesis

Present investigation consisted of an experimental program to study the influence of the process parameters on the weld metal characteristics in laser welds in aluminum alloys. A two-dimensional finite element transient heat transfer model was also developed to simulate the melting and solidification phenomena in keyhole laser welds. Following is the layout of the thesis which describes both the experimental and the modeling aspects of the investigation.

Chapter 2 describes the literature reviewed on specific problems associated with the laser welding of aluminum alloys followed by the nature and causes of porosity in aluminum welds. The significance of vaporization of alloying elements is discussed with regards to the keyhole laser welding. Finally, the thermal modeling of welds is explained with emphasis on the problems associated with the finite element heat transfer models.

Chapter 3 describes the experimental details regarding the welding parameters and the testing procedures used in laser welding of aluminum alloys. The analytical procedures for the selective vaporization studies in aluminum laser welds are also presented here.

In chapter 4, the finite element model is described in terms of the variational formulation, the program THERM developed, and the testing and verification of

the model for stability and accuracy.

In chapter 5, the results of the experimental program are presented and discussed in terms of the weld bead dimensions, the nature and amount of porosity, loss of elements due to vaporization from the weld pool, and the metallurgical structures in and around the weld. Numerical predictions of laser weld pool dimensions in aluminum alloys and local solidification times are also presented here.

Finally, the important conclusions of the investigation are presented in chapter 6.

Chapter 2

LITERATURE REVIEW

Laser welding has drawn considerable attention among the researchers with regard to the mechanical properties of laser welds, interaction of laser beam with the material, and the plasma plume generated at the surface of the material. However, not much information exists regarding the laser welding of aluminum alloys as these alloys have proved very difficult to laser weld. In this chapter, a literature review of some aspects of laser welding of aluminum alloys and the modeling of heat conduction in laser welding is presented.

2.1 Laser Welding of Aluminum Alloys

Factors affecting the laser weldability of aluminum alloys are discussed in the following sections in terms of the high reflectivity to CO_2 laser radiation, high proneness to porosity, and the vaporization of volatile alloying elements.

2.1.1 Laser Material Interactions

Laser irradiation of the material surface results in the heating of the substrate surface due to the absorption of the quanta of light energy by the electrons. These energised electrons rapidly release the energy by a process of collisions resulting in lattice vibrations and thereby heating. The absorption of the laser energy by the surface of the material follows the relationship[21]

$$E(x) = E_0(1 - R)e^{-\alpha x}, \tag{2.1}$$

where E_0 and $E(x)$ are the laser intensities at the surface and at depth x respectively, R the optical reflectivity of the material to laser radiation and α the absorption coefficient. For metallic surfaces, α is of the order of 10^{-4} to 10^{-5}

cm^{-1}, and therefore the energy absorption is limited to a very small depth of 10^{-5} to 10^{-4} cm at the surface. The absorbed energy is transferred into the material by heat conduction. The rate of absorption must be sufficient to initiate melting and for the solid-liquid interface to move progressively to required depths.

Reflectivity R of the material depends on many factors. Figure 1.2 shows the high optical reflectivity of many metallic substances to infra-red radiation. For CO_2 laser radiation at 10.6 micron wavelength, the reflectivity for aluminum is over 95%; less than 5% of the incident energy is therefore used for heating the material surface. Reflectivity is also a function of the surface condition and the chemical composition of the surface. Huntington and Eager[22] studied the effect of the surface preparation on the absorptivity in aluminum alloy 5456. They found anodized and sandblasted surfaces to have improved absorptivity and the electropolished surface with decreased absorptivity as compared to the as-received surface. They also found that for welding applications, the joint geometry had a more pronounced effect on absorptivity than the surface preparation. Jergensen[23] observed an increase in weld penetration when a reactive mixture of argon and oxygen was used as the shielding gas. He related the increased penetration to a decrease in reflectivity of the oxide layer formed on the surface. McLachlan[24] applied a polymer coating on aluminum surfaces to improve the absorption of CO_2 laser radiation.

Reflectivity also depends on temperature as seen in figure 1.3. As a surface is irradiated, the absorptivity improves with interaction time due to the heating and subsequent melting of the surface. By direct measurement of surface reflectivity, Ready[21] found that the spectral reflectivity decreased to about 80% of its initial value for stainless steel.

At high laser intensities, other mechanisms begin to operate which dramatically improve the energy absorption by the material surface. At intensities sufficient to cause localized vaporization of the material, a vapor column or a keyhole is formed as described in figure 1.1. Huntington and Eager[22] found that the increase in absorptivity does not occur at melting, but is associated with the keyhole formation. The marked increase in the absorptivity results from the black body characteristics of the keyhole because of multiple reflections with progressive amounts of energy absorbed at each interaction (see figure 1.4). Effective absorption of up to 90% is possible in some cases.[25]

Further, Marcus et al.[13] have reported that at higher laser intensities sufficient to cause the breakdown of the air at the material surface, the coupling efficiency is considerably improved. For an aluminum target surface, they observed a coupling efficiency of over 30%, or an order of magnitude improvement from the initial absorptivity level. Such enhancement is related to the formation of a plasma, consisting of electrons, ions and neutral atoms, which can partially absorb the laser radiation. The high temperature plasma in turn can transfer the energy to the material at a lower wavelength, thereby improving the effective absorptivity of the material. However, the nature of interactions between the CO_2 laser radiation and the plasma generated at the surface of aluminum alloys is not known. Therefore, quantitative evaluation of the energy transfer from the plasma to the material during keyhole laser welding is not feasible. The enhancement of absorption of laser energy due to the plasma effects can only be incorporated empirically as increased absorptivity coefficients.

Lewis and Dixon[26,27] have shown that at sufficiently high intensities, the plasma ignites and absorbs the incident laser energy. This ignition is associated with the formation of a laser supported absorption wave. During laser radiation, a

series of laser supported combustion waves are initiated, propagated and decayed. As the laser supported absorption wave is opaque, it can prevent the laser energy from reaching the plate surface. It can also result in enhanced coupling by way of reradiation as mentioned earlier. However, the laser supported absorption waves are generated at intensities greater than 10^7 w/cm^2, higher than the intensities involved in high power laser welding.

2.1.2 Porosity in Aluminum Welds

Aluminum alloys are generally weldable by most conventional welding processes. Common defects that can manifest are porosity, crater and longitudinal cracks, incomplete fusion, and undercuts. Most of these defects are avoided by proper welding technique and/or by using compatible filler materials. Porosity, however, has been a persistent problem.[8] The main cause of porosity in aluminum welds is hydrogen picked up from the absorbed and adsorbed moisture in the surface oxides, oil and grease layers on the surface, moisture in the shielding gases, and the dissolved hydrogen in the base metal as well as the filler wires, the surface sources being the most significant.[7,28,29] Absorption of hydrogen in aluminum welds follows Sievert's law.[30] As seen in figure 2.1 and 2.2, the solubility of hydrogen in aluminum at the liquidus temperature is over 19 times that at the solidus temperature, and the solubility in molten aluminum increases drastically with temperature.[31,32] In particular, the ratio of maximum solubility to the solubility at melting point for aluminum is over 70 as compared to about 1.4 for steels.

The differential solubility of hydrogen in aluminum at the melting point has been widely attributed to be the cause of pore formation, by a process of solute rejection and the resulting solute enrichment at the solid-liquid interface.[30,33,34]
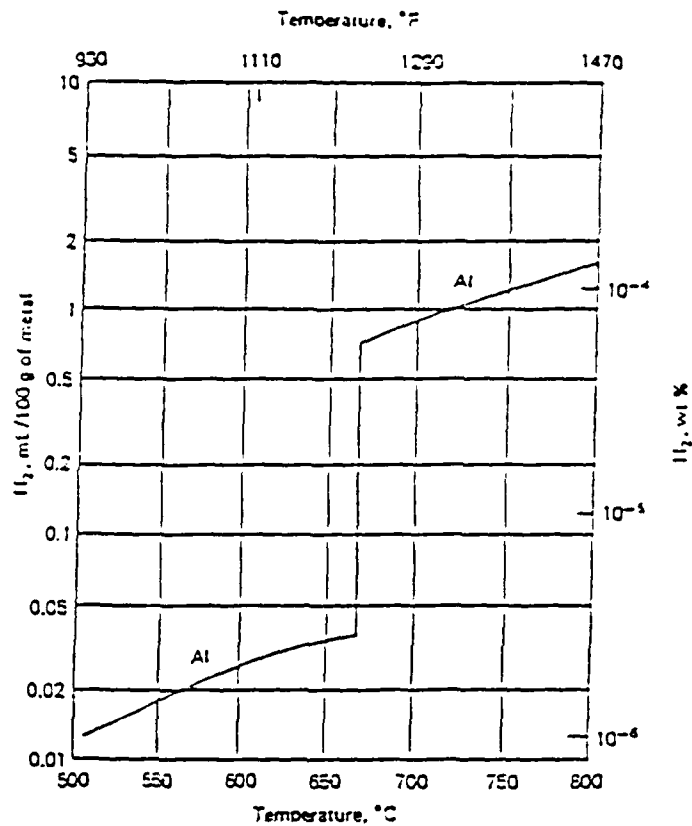
Figure 2.1 Hydrogen solubility in aluminum at
atmospheric pressure showing a sharp jump
at melting point.[31]
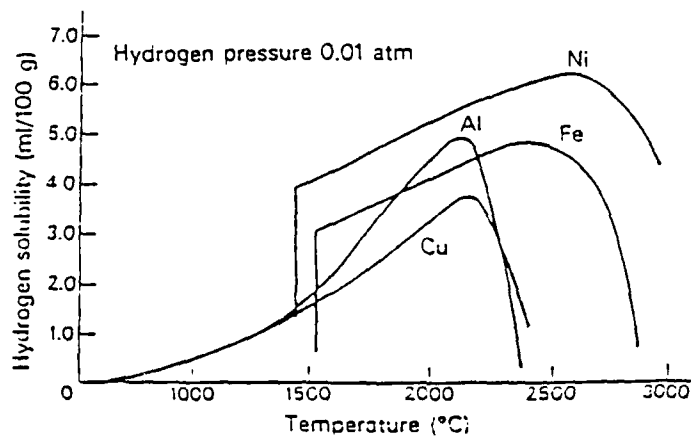
Figure 2.2 Hydrogen solubility in liquid metals showing
high ratio of maximum solubility to melting
point solubility for aluminum.[32]

However, Howden et al.[35] have shown that in welds, the more important factor is the much higher solubility of hydrogen at elevated temperatures. They found that hydrogen is picked up over a small region of the weld pool where temperature may be over 2000 °C. It is then distributed to the rest of the molten pool by convection, thus causing the whole weld pool to attain a higher gas content corresponding to a higher temperature. Thus, bubble nucleation occurs not only at the preferred site of the solid-liquid interface, but also in the molten metal due to its supersaturation. Although homogenous nucleation is not a feasible mechanism for the initiation of pores, heterogeneous nucleation of bubbles in the bulk liquid is possible at numerous inclusions sites available in the molten weld metal. Uda et al.[36] also showed that the driving force for pore formation in aluminum is the high solubility of hydrogen at elevated temperatures resulting in bubble nucleation in the liquid. Nikiforov et al.[37] calculated that in the diffusive redistribution of hydrogen during solidification, hydrogen does not accumulate substantially at the solid-liquid interface, and is not the main mechanism of pore formation in aluminum welds.

Once nucleation has occurred, growth of the pores is a function of the solidification rate, the diffusion rate of hydrogen, overall concentration of hydrogen in the weld metal, and the concentration of the stable nuclei.[34] Porosity in welds is therefore the result of two competing phenomena – nucleation and growth of bubbles in the liquid metal and at the solid-liquid interface due to the rejection of solute hydrogen, and the solidification of the liquid metal. The weld cooling rate and hence the solidification rate and morphology significantly affect the entrapment of bubbles in the solidifying metal.

Porosity can occur in many forms in aluminum fusion welds. The rejected gas can be nucleated both in the liquid during solidification, and in the solid

immediately afterwards.[30,38] The former is called the primary porosity and the latter the secondary porosity. Primary porosity in turn can manifest in two ways. First type is the interdendritic porosity at low to intermediate levels of supersaturation in the molten metal – it is growth substructure controlled and occurs as small spherical pores or as long angular pores. The second type is the large spherical pores which nucleate in highly supersaturated liquids and is surface tension controlled. Secondary porosity usually consists of small spherical pores distributed inside the grains.

Alloying elements like Mg, Zn, Cu and Si have significant effect on the sensitivity to pore formation in aluminum alloys. Opie et al.[39] showed that additions of Cu and Si reduce the solubility of hydrogen, the former being more effective. Woods[40] found that addition of 6% Mg nearly doubles the hydrogen solubility in aluminum. Alloying elements not only affect the solid solubility, but also the rate of absorption of hydrogen. In addition, alloying additions affect the solidification range thereby affecting the bubble escape or entrapment.

Moreover, aluminum has a high volumetric expansion rate of about 6% on melting as compared to iron which has only about 2.2% volume expansion.[41] This manifests as shrinkage cavities or pores during solidification of castings depending on the nature of heat extraction. Kubo et al.[42] have shown that simultaneous occurrence of shrinkage and gas evolution is required for pore formation.

In spite of the high sensitivity, weld metal porosity in aluminum alloys can be minimized by proper surface cleaning procedures. However, laser welds in aluminum alloys are particularly prone to extensive porosity. Although electron beam welding and laser welding are similar processes involving high intensity heat sources and keyhole mode of welding, aluminum alloys are being electron beam

welded, but laser welding is proving so difficult.[43] The electron beam couples easily to aluminum alloys, thus requiring much lower intensities as compared to the laser beam. The high vacuum required in electron beam welding ensures the removal of absorbed moisture and gases from the surface, and also assists in the growth and escape of the bubbles. In keyhole laser welding, the power intensity required to initiate the keyhole in aluminum alloys is much higher than that required to maintain the keyhole.[25] Overheating of molten metal caused by the higher intensity can have deleterious effects like increased hydrogen content in molten aluminum and excessive vaporization of the volatile alloying elements, thereby increasing the probability of porosity formation during solidification.

Snow et al.[9,10] report some qualitative studies in aluminum, but were unsuccessful in obtaining sound welds. They attempted controlled beam spot rotation to disperse the intense input energy that is required for coupling. The beam rotation improved the bead surface appearance and also reduced the violent eruptions that take place on the weld surface in keyhole laser welds in aluminum alloys. However, beam spot rotation requires extensive modification to the laser optics. They also found excessive penetration and drop through in deep penetration laser butt welds in 5xxx series aluminum alloys due to the high fluidity of molten metal. Other researchers also report some success in keyhole laser welds in aluminum alloys, but porosity was not eliminated.[11,22,44]

2.1.2 Alloying Element Vaporization

Alloying elements added to aluminum for improving the mechanical properties and corrosion resistance are Cu, Mn, Mg, Zn, Si, Fe, Ti, etc. Of these, Mg and Zn are an order of magnitude more volatile than aluminum as indicated by the vapor pressure data for these elements. During welding, selective vaporization of

the alloying elements in the aluminum alloys is expected, with significant effect on the mechanical properties of the welds. Moon and Metzbower[11] investigated the redistribution of the solutes and the precipitates in the fusion zone of high power laser welds in aluminum alloy 5456. They found depletion of magnesium in the weld, and vaporization of up to 90% of the precipitates. They also found increased toughness in the weld resulting from the fusion zone purification, but the tensile strength and ductility had decreased.

Block-Bolten and Eager[45] analyzed the selective vaporization of alloying elements like Mn, Cr, Ni, and Al from stainless steel welds using the kinetic theory of gases and the tabulated thermodynamic data for metallic elements and binary alloys. They found Fe and Mn to be the dominant species which vaporized during arc welding of these alloys. Further, using plots of evaporation power vs. inverse temperature, they estimated the maximum weld pool surface temperature to be approximately 2500 °C. Khan and Debroy[46] used a similar analysis and changes in the laser weld compositions in type 202 stainless steels to predict weld pool surface temperatures. They demonstrated that the relative rates of vaporization of any two elements from the molten pool can serve as an indicator of weld pool temperature. Shaurer et al.[47] used a similar approach to confirm the peak temperature measurements they made in electron beam weld cavities using an infrared radiation pyrometer. From the weld cross-sections, they measured the cavity depth h and the base radius of the cavity r to calculate the vapor pressure P_v of the column using the relationship

$$P_v = \frac{2\,\sigma}{r} + \rho\,g\,h, \tag{2.2}$$

where σ is the surface tension of the material, ρ the density, and g the acceleration due to gravity. Equation 2.2 represents the hydrodynamic equilibrium at the bottom of the vapor column. From the calculated vapor pressure, the associated

temperature was determined using the vapor pressure - temperature data for pure metals. An analysis of the selective evaporation of alloying elements in laser welds in aluminum alloys can provide an insight into the phenomena occurring and the work carried out in this investigation is discussed in later chapters.

2.2 Modeling of Heat Flow in Laser Welds

To develop a predictive model for analyzing the thermal behavior of welds, the heat conduction in the solid and the liquid metal, as well as the convective heat transfer in the molten pool must be considered. However, Oreper and Szekely[12] have shown that the effect of convection in the molten pool on the temperature profiles in the weld can be neglected if

$$Re \, \frac{L_z}{L} \, Pr \, k < 1. \tag{2.3}$$

Here, Re is the Reynold's number, L_z the characteristic depth of weld, L the plate thickness, Pr the Prandtl number, and k the characteristic thermal conductivity. In the absence of electromagnetic forces in laser weld pools, the fluid flow is dominated by the buoyancy forces due to the thermal gradients, and to a lesser extent the surface tension driven flows on the liquid surface. Under these conditions, the Reynold's number can be approximated as $Gr \, A^3$, where Gr is Grashof's number and A the aspect ratio of the weld. From the experimental results, most of the laser welds in aluminum alloys were found to satisfy the equation 2.3, and therefore the conduction dominated weld heat flow models neglecting the convective heat transfer terms are adequate. The convection in the molten metal also results in rapid dissipation of the superheat. In numerical solutions, this is usually approximated as artificially enhanced thermal conductivity in the molten pool.[48]

Welding heat transfer is a special class of heat conduction problems – called the Stefen problem – which involve melting and/or solidification. The problem is non-linear due to the moving boundary of the solid-liquid interface whose location is not known a priori, phase change and the corresponding absorption/evolution of the latent heat of fusion, temperature dependent thermal properties, and the convective and radiative boundary conditions. It is a transient three-dimensional problem involving considerable mathematical complexity, and requires numerous simplifying assumptions to obtain a reasonable analytical solution. In the following sections, some of the analytical solutions and the numerical techniques applied to solve these problems are discussed.

2.2.1 Analytical Methods

Rosenthal[49] in his landmark paper "The Mathematical Theory of Heat Distribution during Welding and Cutting" presented a three-dimensional analytical model for determining the temperature profiles surrounding a weld heat source in a semi-infinite media. The main assumptions in his model were

i. A point heat source,

ii. Constant thermal properties,

iii. No latent heat of melting,

iv. No surface heat losses,

v. Resistive heating of the material neglected.

He assumed a quasi-steady state condition in which the isotherms achieve a steady state in a moving coordinate system attached to the heat source. Such

an assumption is valid over the duration of the weld cycle away from the initial transients and end effects. He also presented a two-dimensional line source model applicable for through thickness welding of thin plates. Myers et al.[50] presented numerous solutions based on the above model for spot welding, filler wire additions, thin plate welding, thick plate welding, plates with finite widths, etc. Although, point/line source models give a reasonably good prediction far from the weld, the results near the fusion zone are far from satisfactory. Christensen et al.[51] measured the temperature distribution in steel and aluminum welds, and compared the results with those predicted by the point source model. They observed a systematic deviation from the predicted results both in the weld bead dimensions and in the temperature distribution outside the weld pool. Predictions far from the weld centerline were reasonably accurate.

Subsequent researchers have tried to improve the point/line source model by removing some of the basic assumptions. Malmuth[52] took into account the phase change involved in the melting and solidification of welds. He used the matched asymptotic expansions to solve the problem, and found that the previous empirical method of subtracting the latent heat from the input power overpredicted the effect of phase change on weld penetration. Trivedi[53] incorporated a moving circular cylindrical heat source of finite height and radius. Tong and Geidt[15] used a similar heat source to predict temperatures in deep penetration electron beam welds. Although, the electron beam cavity depth oscillates at a frequency of about 10 - 100 cycles/second, they reasoned that the solid-liquid interface fluctuates only slightly, and justified their assumption of a constant temperature cylindrical boundary heat source. Their results agreed within 20% of the available experimental results. Miyazaki and Geidt[16] solved the heat conduction equation in elliptical coordinates using an elliptically shaped heat source. Swift-Hook and Gick[54] used the line

source theory for predicting penetration in EB and laser welding. Comparison with electron beam welds was good; however, in laser welding an order of magnitude improvement in weld penetration could be expected.

It is clear that for purely analytical solutions, many simplifying assumptions are necessary. Even tackling one or two of the basic assumptions results in enormous complexity. Such solutions, therefore can only have a qualitative appeal closer to the heat source, although some useful information can be derived for locations far from the weld. For instance, the prediction of martensitic formation in the heat affected zone (HAZ) surrounding the fusion welds in high carbon steels is usually done with reasonable accuracy using the analytical models. However, improved models are required for better understanding of the heat flow near the weld source.

2.2.2 Numerical Methods

Numerical techniques – both finite difference and finite element methods – are proving to be more suitable for solving the heat transfer problems with phase change. Time variant meshes which continuously trace the location of the solid-liquid interface are limited to simpler geometries and one-dimensional problems. For such an approach, two sets of partial differential equations with the associated boundary and initial conditions are used, one each for the solid and liquid region. In addition, continuity of temperatures is enforced at the interface, along with a relation for the temperature gradients representing the absorption or liberation of latent heat

$$k_l \frac{\partial T_l}{\partial x} - k_s \frac{\partial T_s}{\partial x} = \rho \ L \ \frac{ds(t)}{dt}.$$

Here, k_l and k_s are the thermal conductivity in the solid and liquid regions whose interface is defined by $x = s(t)$, t being the time parameter, T the temperature,

ρ the density and L the latent heat of fusion. Generally, fixed mesh approaches are used – ie., weak solutions are attempted where only one partial differential equation with the associated boundary conditions is used for the whole region.

Finite difference methods have been widely used for modeling the solidification of castings, and for welding problems. However, finite element methods are increasingly being employed for welding applications as these techniques are readily adapted to problems with non-linearities either due to geometric or material effects. Both methods are equally effective for simpler geometries, but for complex geometries, finite element method is clearly superior. It is also easily coupled to thermal stress problems. Gray et al.[55] compared the two methods with regards to accuracy and efficiency. They concluded that for certain formulations, the finite element method takes less time and is more accurate than the finite difference method. They also found that the finite element method showed a maximum accuracy with increasing number of nodes after which the error and computation time increased due to the round-off error in the Gaussian elimination scheme. The computer core storage required for the finite element method is larger.

The finite element formulation uses either the variational method or the weighted residual methods like the Galerkin method, least square method, or the collocation method. By the usual discretisation procedure, the governing partial differential equation and the associated boundary and initial conditions are transformed into a set of simultaneous differential equations of the form

$$C \dot{T} + K T = R. \tag{2.2}$$

Here, T is the nodal temperature vector and $\dot{T}$ the vector of $\frac{\partial T}{\partial t}$. C describes the heat capacity terms and includes the density, specific heat and the volume of

the elements. K represents the conductivity matrix and includes heat conduction between the various elements and also the convective and radiative boundary conditions if any. The load vector R represents the effects of the specified boundary heat flux, specified temperature conditions, internal heat generation terms, etc.

2.2.2.1 Consistent vs. Lumped C

For linear heat conduction problems, the conductivity matrix K in equation 2.2 is similar for both finite element and finite difference schemes. The heat capacity matrix C is diagonal for the finite difference method. However, C is non-diagonal for the finite element method, and is called the consistent heat capacity matrix. Sometimes, a lumped C matrix is used instead in finite element formulations, which involves unequal distribution of capacitance to each node proportional to the corresponding nodal volume. Fujii[56] has analyzed the finite element method with both the consistent and the lumped C with regards to accuracy and stability. He defined the maximum principle which states that negative temperatures cannot occur when the initial and boundary temperatures are non-negative provided that there is no heat sink. Further, the maximum temperature must occur at the boundary. He concluded that for the maximum principle to hold for the lumped C approach, the time increment must be sufficiently small. The consistent C is more restrictive with both upper and lower limits on the time increment. He also found that the lumped C approach loses its value when high accuracy is required as lumped C does effect overall accuracy.

2.2.2.2 Integration Schemes

Direct integration methods, rather than the mode superposition method, are generally used in heat transfer problems in which the solution to equation 2.2 is

obtained over a number of successive time steps. Thus, in welding heat transfer problems with thermal history dependent behavior, incremental solutions are attempted over many time steps, and due to the non-linearities involved, iterations may also be necessary over each time step to balance the residual 'load' vector. Although finite element discretisation over the time domain is possible,[57] finite difference methods are more widely used. The popular two level methods in use are the Euler's methods, the Crank-Nicholson central difference method, Wilson-θ method etc., and of the three level methods, the Gear's and Lee's methods have been used. The choice of the technique is based on the stability characteristics, the level of accuracy desired, and the largest time step allowed. For problems involving melting and solidification, the above factors are intimately linked to the phase change phenomena. The latent heat of melting or solidification is usually incorporated in the numerical techniques by the following two methods :

i. Specific Heat Method : In this method, the latent heat is incorporated as an apparent increase in the specific heat of the material over the solidification range. Although valid for metallic alloys, the method requires the assumption of an artificial but small solidification range for pure metals with a planar phase change. The method results in a sharp discontinuity in the temperature dependent specific heat for metals and alloys, and can lead to undesirable oscillations of the solidification front. Hsiao[58] used this method with a special algorithm to avoid missing the release or absorption of latent heat and noted some improvement. Friedman[59] used a variation of this method by way of an iteration scheme for incorporating the latent heat directly at each time step.

ii. Enthalpy Method : Comini et al.[60] have shown that the enthalpy H given by

the relationship

$$H = \int \rho c \, dT \qquad (2.3)$$

is a much smoother function of temperature than is the specific heat with the latent heat included over the solidification range. They calculated the volumetric specific heat from the known enthalpy at a point using an averaging technique

$$\rho c = \frac{dH}{dT} = \frac{1}{3}\left(\frac{\partial H}{\partial x}\frac{\partial x}{\partial T} + \frac{\partial H}{\partial y}\frac{\partial y}{\partial T} + \frac{\partial H}{\partial z}\frac{\partial z}{\partial T}\right) \qquad (2.4)$$

where $\frac{\partial x}{\partial T}$, $\frac{\partial y}{\partial T}$ and $\frac{\partial z}{\partial T}$ are approximated as the inverse of the temperature gradients in the x, y and z directions. The method results in a more accurate calculation of the temperature dependent specific heat at any point in the material. Pham[61] has shown that this method is similar to the one proposed by Hsiao.

Explicit methods, in which the heat equilibrium is considered at the present time step to calculate the temperatures at the next time step, usually do not have good stability characteristics. Implicit methods on the other hand allow larger time steps because of their better stability characteristics, although they may require iterations. Myers[62] compared the Euler's explicit method and Crank-Nicholson's central difference method for a two-dimensional transient heat conduction problem. He found the Crank-Nicholson's method to be more stable than the Euler's explicit method at larger time steps than the Euler's explicit method. Bathe[63] analyzed the two level schemes of the type

$$^{t+\alpha\Delta t}\dot{T} = \frac{^{t+\Delta t}T - {}^{t}T}{\Delta t}$$

where

i. $\alpha = 0$ is the Euler's forward or explicit method which is first order accurate in Δt,

ii. $\alpha = 1$ is the Euler's backward or implicit method which is also first order accuarte in Δt, and

iii. $\alpha = 0.5$ is the Crank-Nicholson's central difference method which is second order accuarte in Δt.

By analyzing the integration algorithm of a typical equation in 2.2, he showed that for stability, the following relationship must be satisfied

$$\left| \frac{1 - (1 - \alpha) \ \Delta t \ ^{t+\alpha\Delta t}\lambda}{1 + \alpha \ \Delta t \ ^{t+\alpha\Delta t}\lambda} \right| \leq 1 \tag{2.5}$$

where λ is the eigen value of the equation under consideration. This relationship holds provided the time step satisfies the condition

$$\Delta t \leq \frac{2}{(1 - 2\alpha) \ ^{t+\alpha\Delta t}\lambda}.$$

Thus, the integration scheme is unconditionally stable provided $\alpha \geq 0.5$, and is only conditionally stable for $\alpha < 0.5$. Wood[64] has described the phenomenon of 'noise' or oscillations that can occur in the Crank-Nicholson scheme thereby effecting the accuracy, although the solution is stable. Donea[65] also observed severe oscillations in the Crank-Nicholson scheme and found that for fast varying boundary conditions requiring short time accuracy, an iterative two level Galerkin process with less severe oscillations was more accurate than the Crank-Nicholson method. Comini[60] used the Lee's three level scheme with unconditional stability in his formulation to avoid iterations. However, the formulation results in a recurrence scheme with a solution process involving the inversion of a matrix containing K and C. For large problems with many degrees of freedom, this inversion process can become a big constraint with the resulting loss in accuracy.

The above techniques all used the temperature formulation. The alternative enthalpy formulation has the disadvantage that only explicit schemes can be

used with the related stability problems and the shorter time steps allowed. Pham[61] used a combination approach with the three level Lee's method. However, his formulation precluded the consistent heat capacity approach. The Euler's backward implicit method promises to be the most suitable for welding problems in metallic alloys due to its unconditional stability allowing larger time steps, simplicity of formulation with temperature as the unknown parameter, feasibility of using with either the lumped or the consistent heat capacity matrix, and for both the specific heat or the enthalpy method for the phase change problems. The accuracy of the method is good although it has not been well documented for two-dimensional problems, and therefore was investigated as discussed later in chapter 4.

2.2.2.3 Weld Heat Source Distribution

Analytical models discussed earlier preclude the use of complex welding heat flux distribution, and have been limitted to point/line source or cylindrical heat sources – both circular and elliptical – of constant temperature boundaries. Numerical techniques allow much more flexibility in modeling the distribution of heat flux in the welding arc. Pavelic[14] proposed a gaussian distribution model in which the specific heat flux $q(r)$ at any radius r about a normal circular heat source is given by the expression

$$q(r) = q_0 \, e^{-cr^2}. \tag{2.6}$$

Here, q_0 is the peak specific heat flux which can be determined by integrating the heat flux over the radius r from 0 to ∞, and is equal to $\frac{cQ}{\pi}$ where Q is the effective welding heat input. The constant c in equation 2.6 is determined assuming a finite upper limit of integration r_0 where the specific heat flux $q(r)$ drops to a negligible value. For a value of 5%, the constant c is $\frac{3}{r_0^2}$. Such a gaussian welding

heat source can be included in the numerical model as a boundary heat flux valid over a region of the surface, or as an internal heat source assumed present over a small thickness at the surface. Pavelic's model has been applied to arc welding problems with reasonable accuracy. However, the the model is clearly not valid for deep penetration electron beam and laser welds.

Goldak et al.[19] presented a more complicated double ellipsoidal model for the weld heat source in which the peak flux q is a function of x, y, z and t and is described by the expression

$$q(x, y, z, t) = \frac{6\sqrt{3} f Q}{abc\pi\sqrt{\pi}} e^{\frac{-3x^2}{a^2}} \, e^{\frac{-3y^2}{b^2}} \, e^{\frac{-3(z+v(\tau-t))^2}{c^2}}. \tag{2.7}$$

In equation 2.7, the parameters a, b, c and f can take different values in the front and rear part of the weld pool and Goldak chose these eight parameters based on the experimental weld bead profile. He used the model to analyze the heat flow in a submerged arc weld in a 10 cm thick carbon steel plate, and a deep penetration electron beam weld in 1.95 cm thick steel plate. Although, the predicted weld bead shape in the submerged arc weld was in good agreement with the experimental results, the penetration in the electron beam weld was underpredicted by over 40%.

Majumder et al.[17] and Chande et al.[18] have presented a three-dimensional finite difference model for laser welding. They assumed the Beer-Lambert law of energy absorption for deep penetration laser welds using the relation

$$q_y = q_s e^{-\beta y} \tag{2.8}$$

where β is the absorptivity coefficient, and q_s and q_y the power intensities at the surface and at depth y, respectively. They also assumed that once a particular node reached the boiling point, it became transparent to the laser beam allowing

the next layer to receive the energy with the energy absorption determined by equation 2.8. The model may simulate the creation of the keyhole and thus the initial transient, but is not valid once the keyhole has been established and welding is in the quasi-steady state.

A model which can more accurately simulate the deep penetration keyhole laser welds is required and some of the attempts made in this investigation are discussed in later chapters.

2.5 Summary

Aluminum alloys are not being laser welded due to their proneness to porosity, poor weld bead appearance, and vaporization of alloying elements. Precise control of the energy input seems to be necessary to improve the laser weldability of theses alloys. A detailed parametric study of the influence of welding parameters and alloying content on the weld characteristics , porosity formation and alloying element loss is required to better understand the phenomena occurring. In addition, numerical simulation of the laser weld thermal cycle in aluminum alloys can further enhance the understanding of the mechanisms involved. Present investigation was carried out to meet some of these objectives.

Chapter 3

EXPERIMENTAL DETAILS

A 15 kw AVCO CO_2 laser welding machine with F7 optics was used to weld the aluminum alloys in the down-hand position. Autogenous butt welds were made in the keyhole mode on $20 \times 10 \times 1.27$ cm ($8 \times 4 \times 0.5$ ") plates in aluminum alloys 2219, 5083 and 5456. Bead-on-plate welds were also made in aluminum alloy 6061 on plates of above dimensions in the keyhole mode, and $20 \times 10 \times 0.4$ cm ($8 \times 4 \times 0.16$ ") sheets in the conduction mode. All plates were in the annealed condition prior to welding, except alloy 6061 which was in the T-6 temper. Table 3.1 gives the nominal composition of the aluminum alloys used.

3.1 Surface Preparation

To eliminate probable sources of hydrogen and other contaminants from the welds, following surface preparation scheme recommended by AWS was used prior to welding:

i. Initial washing and scrubbing with detergent to remove dirt followed by drying to remove moisture.

ii. Mechanical brushing using stainless steel brushes to remove oxide layers.

iii. Cleaning with acetone to remove oil and grease layers.

For butt welds, the plate edges were machined prior to above preparation. The surfaces were then characterized by depth profile technique using Secondary Ion Mass Spectrometry (SIMS) for levels of hydrogen, oxygen and carbon in the cleaned and the as-received conditions of the plate. Plates used for off-focus

Table 3.L Nominal composition of aluminum alloys used.

Element	2219	5083	5456	6061
Mg	0.02 max	4.00 – 4.90	4.70 – 5.50	0.80 – 1.20
Cu	5.80 – 6.80	0.10 max	0.10 max	0.15 – 0.40
Mn	0.40 max	0.40 – 1.00	0.50 – 1.00	0.15 max
Si	0.20 max	0.40 max	0.25 max	0.40 – 0.80
Fe	0.3 max	0.4 max	0.40 max	0.70 max
Cr	–	0.05 – 0.25	0.50 – 0.20	0.04 – 0.35
Zn	0.10 max	0.25 max	0.25 max	0.25 max
Ti	0.02 – 0.10	0.15 max	0.20 max	0.15 max
V	0.05 – 0.15	–	–	–
Zr	0.10 – 0.25	–	–	–
Others – each	0.05 max	0.05 max	0.05 max	0.05 max
Others – total	0.15 max	0.15 max	0.15 max	0.15 max
Al	Remainder	Remainder	Remainder	Remainder

keyhole welds and conduction mode welds were spray painted black to ensure coupling.

3.2 Welding Parameters

Laser power, welding travel speed and the location of laser beam focus with respect to the plate surface were the main welding parameters investigated in the welding experiments. Table 3.2 describes the welding parameters used for each of the aluminum alloys. Welds were made at input power levels in the range of 5 to 14 kw. At each power level, two or three appropriate welding travel speeds were used in the range of 0.212 to 3.387 cm/sec (5 to 80 inches per minute (ipm)) to obtain reasonable weld bead dimensions (ie. partial to full penetration welds). In alloys 2219, 5083 and 5456, laser welds were made using two different focus conditions to study the influence of input power intensity on weld characteristics : (1) on-focus keyhole welds – the laser beam was focussed on the plate surface, and (2) off-focus keyhole welds – the laser beam was focussed 0.635 cm above the plate surface. From spot burns on acrylic plates, the beam spot diameters on the plate surfaces for the above two cases were estimated to be 0.08 cm and 0.12 cm respectively. The keyhole mode welds in alloy 6061 were all made with the beam focussed on the plate surface. For the conduction mode welds made in alloy 6061 at a separate facility, the beam cross-section obtained was rectangular (0.6 × 0.1 cm) with considerably lower power density. Further, in this setup, the depth of focus was significantly large compared to the plate thickness, and therefore the location of the focus was not critical.

Helium gas was used for shielding of the molten weld pool as well as for plasma suppression. A constant flow rate of 150 cfh was used during the welding trials. As aluminum welds can result in drop-through due to the high fluidity of the molten

Table 3.2. Welding parameters used.

Alloy	Welding Mode	Power (kw)	Speed (ipm)
2219 5083 & 5456	On-Focus† Keyhole mode	5. 7.5 10.	10., 15. 10., 20. 20., 30., 40.
	Off-Focus‡	4. 5. 6. 7.5 10.	10. 10. 10. 10. 10.
6061	On-Focus† Keyhole mode	10. 11. 12.	30., 40., 50., 60., 70., 80. 40., 60. 30., 40.
	Conduction Mode*	7.5 10. 12. 14.	10., 15., 25. 10., 15., 20. 30. 5., 10.

† : beam focussed on plate surface; plate thickness 1.27 cm.

‡ : beam focussed 0.635 cm above plate surface; plate thickness 1.27 cm.

* : plate thickness 0.4 cm except for 14 kw welds which were made on plates of thickness 1.27 cm.

aluminum, all welds were made using a stainless steel backing plate to support the molten pool.

3.3 Testing

Weld cross-sections were examined using an optical microscope to determine the weld penetration, top bead width, aspect ratio, and the weld cross-sectional area. At least three sections were examined for each weld and averaged results are presented. The weld cross-sectional areas were determined from the macro-photographs of the welds. The weld profiles were cut out from these pictures and weighed. From known magnifications of the macro-photographs and the specific weight of the paper used, the weld cross-sectional areas were calculated.

The nature and distribution of porosity in the laser welds in aluminum alloys was studied by microscopic examination of transverse and longitudinal sections of the welds. To compare the levels of porosity present in the different welds, the volume of weld metal porosity per inch of weld length was determined by density measurements. Three specimen of dimensions 3.81 × 2.54 cm (1.5 × 1.0") were cut and machined from each welded plate, and were then weighed in air and water. Comparing the results obtained with those from control specimen from the base metal of each alloy, the amount of porosity in each specimen was calculated. Assuming the cross-sectional area of the weld to be uniform over the specimen length, the porosity per unit volume of the weld metal was determined. It is to be noted that the density measurements give the total amount of voids present in the weld metal, which may be in the form of gas pores or shrinkage cavities.

Microstructures in the weld metal, the heat affected zone (HAZ) and the parent metal were examined using optical and scanning electron microscopes. Presence of any micro-porosity was also investigated. Electron microprobe analysis were

conducted across the weld cross-sections to evaluate the loss in alloying elements and segregation patterns in the weld, HAZ and the parent metal.

3.4 Vaporization Studies

As mentioned in section 3.3, loss of alloying elements from the laser welds was determined for a limited number of welds using electron micro-probe analyzer. Based on the works described in section 2.2.2,[45−47] an analysis of the vaporization of alloying elements in laser welds in aluminum alloys 2219, 5083, 5456 and 6061 was carried out. A brief description of the methodology used for developing the relevant plots is described in the next few paragraphs.

Assuming Raoultian behavior, the equilibrium vapor pressure P_i of a solute i in solution with solvent j is given by the expression

$$P_i = x_i . P_i^0 \tag{3.1}$$

where x_i is the mole fraction ($x_i + x_j = 1$), and P_i^0 the vapor pressure of pure i at the temperature of the solution. If the component i behaves ideally in the solution,

$$a_i = x_i$$

where a_i is the activity of the specie i in the solution. Using the tabulated vapor pressure data P_i^0 as a function of temperature for metallic elements[66] and the equation 3.1, a plot of equilibrium pressure P_i versus inverse temperature can be developed for each specie in the binary system of aluminum and the relevant alloying elements. Assuming negligible interaction effects, a composite vapor pressure-temperature plot for each of the aluminum alloys 2219, 5083, 5456 and 6061 can be developed. These are shown in figures 3.1(a) to 3.4(a).

Next, the evaporation rates as a function of inverse temperature were determined for each of the species using the following relation given by Dushman[67]

$$V_i = 44.33 \times P_i \cdot \left(\frac{M_i}{T}\right)^{\frac{1}{2}} \tag{3.2}$$

where V_i is the vaporization rate in gm/cm^2sec, M_i the molecular weight in gms, and T_i the temperature in °K. The plots of evaporation rate versus temperature for the four aluminum alloys are shown in figures 3.1 (b) to 3.4 (b). Only alloying elements Cu, Mn, Mg and Zn have been included in these plots along with Al as these have significantly higher activities as compared to other elements in the alloy.

Next, using the method presented by Cobine and Burger,[68] the evaporation power as function of temperature was determined using the relation

$$E_i = V_i \times (L_i - \Delta H_i^M) \tag{3.3}$$

where E_i is the evaporation power in watts/cm^2, L_i the latent heat of vaporization in joules/gm, and ΔH_i^M the heat of mixing in joules/gm given by the expression

$$\Delta H_i^M = \frac{\partial R . ln \; \gamma_i}{\partial(\frac{1}{T})},$$

R being the gas constant and γ_i the activity coefficient $(\frac{a_i}{x_i})$. As the data on the heat of mixing as a function of temperature was not available for the systems under consideration, ΔH_i^M was neglected in the calculation of the evaporation powers; the error involved was determined to be not significant. Plots of evaporation power versus the temperature are shown in figures 3.1 (c) to 3.4 (c) for the four aluminum alloys being studied.

The above vaporization plots when applied to the power intensities involved in aluminum laser welds can give some important information. For instance, using
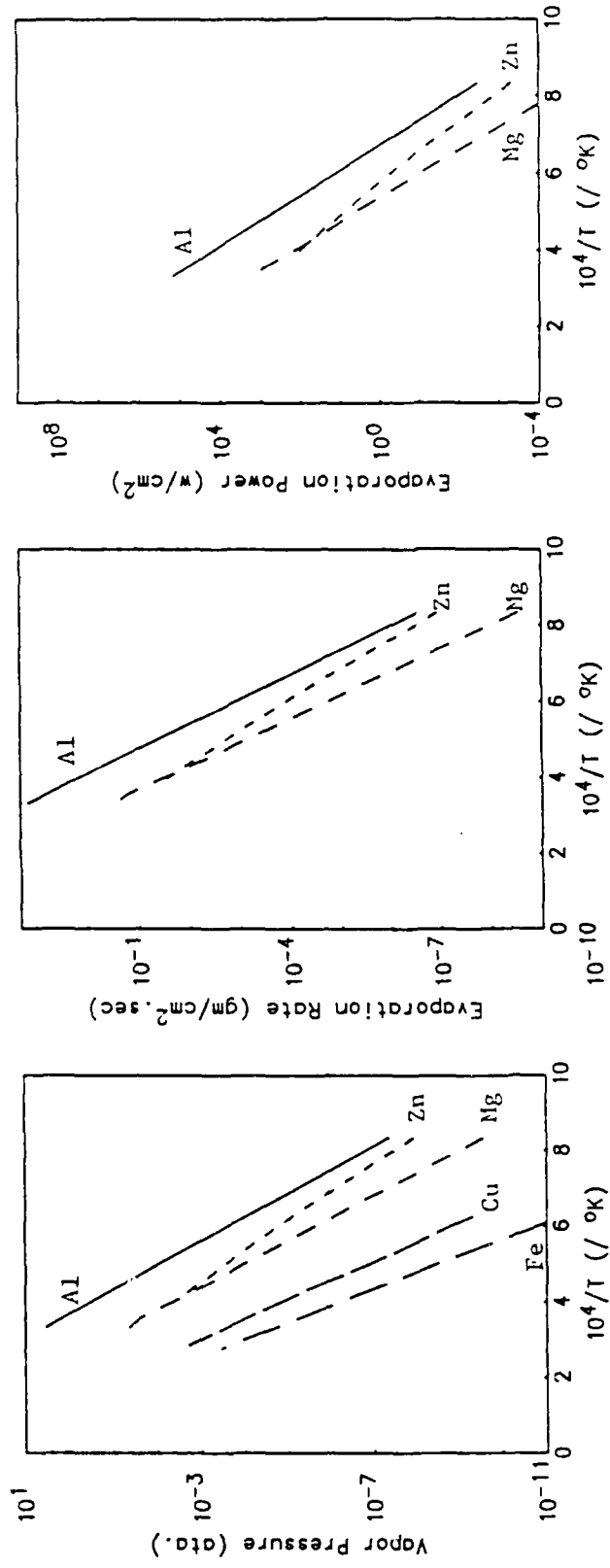
a. Vapor pressure.

b. Evaporation rate.

c. Evaporation power.

Figure 3.1 Vaporization plots for aluminum alloy 2219.
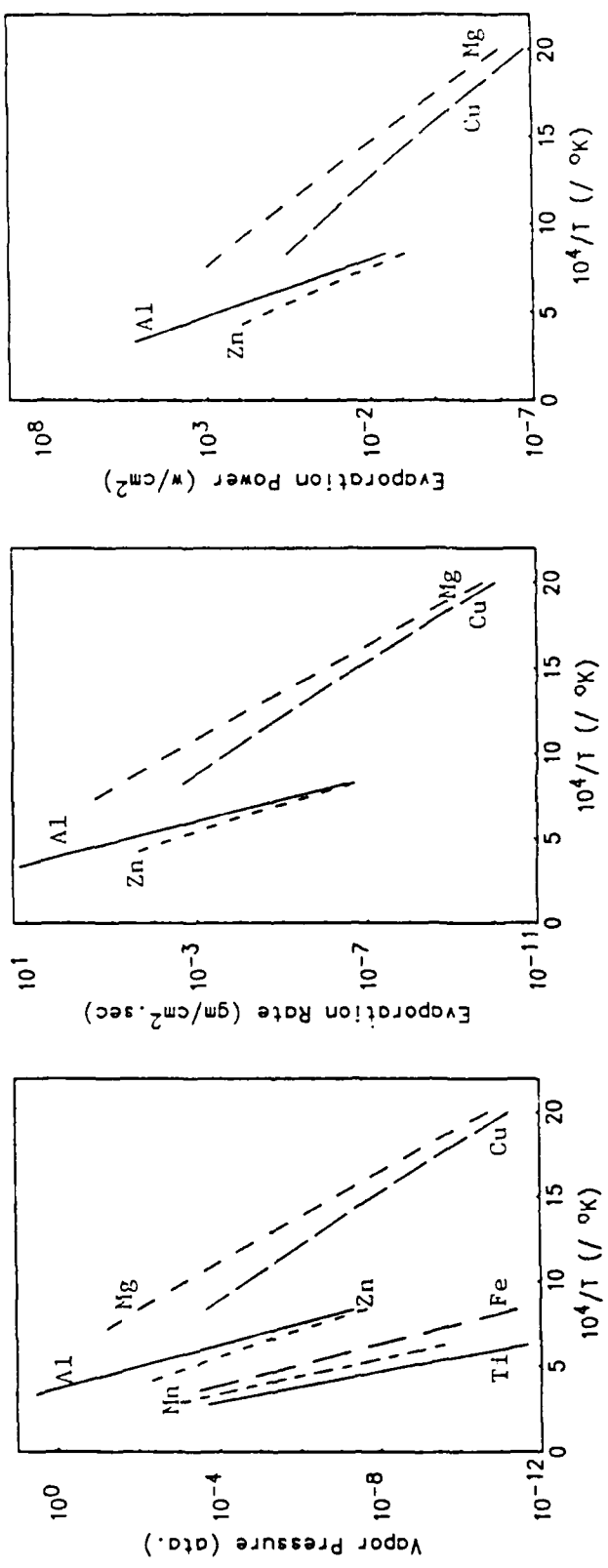
a. Vapor pressure.

b. Evaporation rate.

c. Evaporation power.

Figure 3.2 Vaporization plots for aluminum alloy 5083.
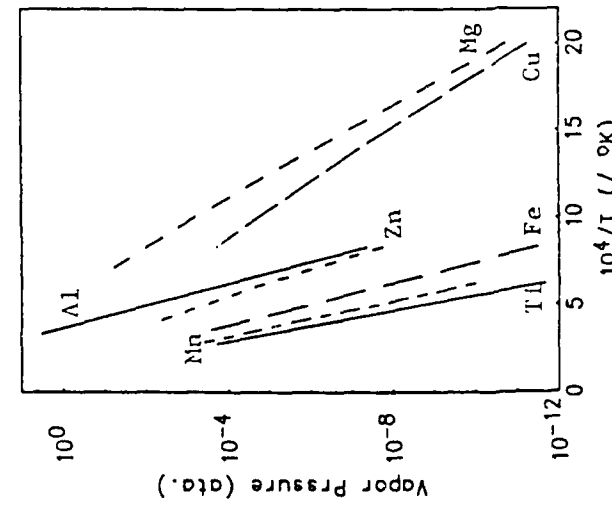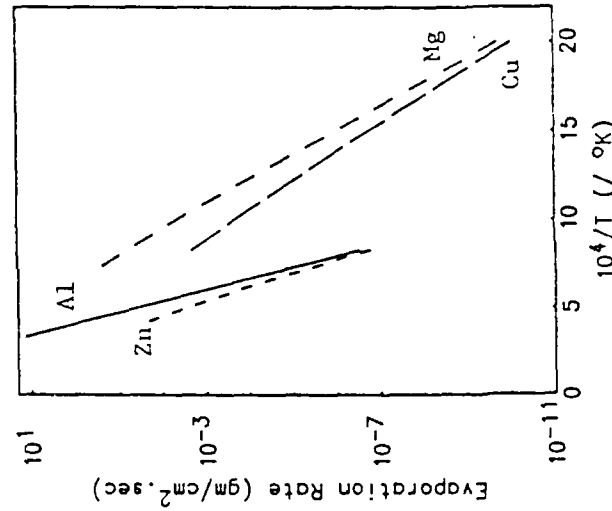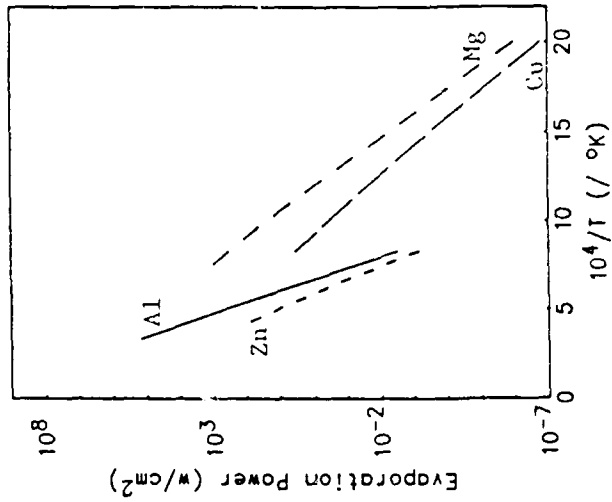
a. Vapor pressure.

b. Evaporation rate.

c. Evaporation power.

Figure 3.3 Vaporization plots for aluminum alloy 5456.

41
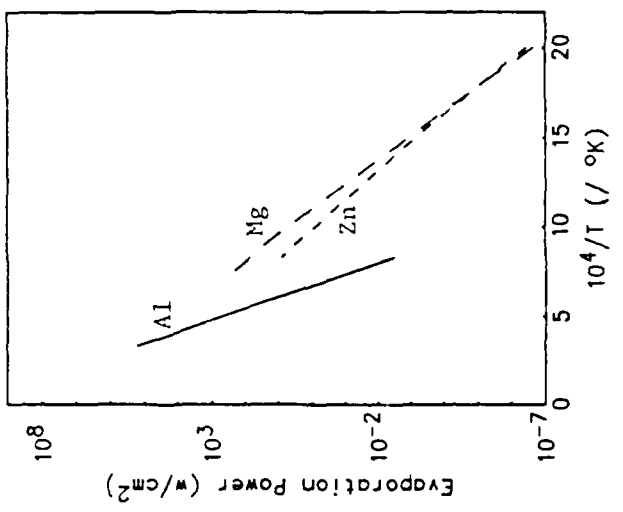
c. Evaporation power.

b. Evaporation rate.

a. Vapor pressure.
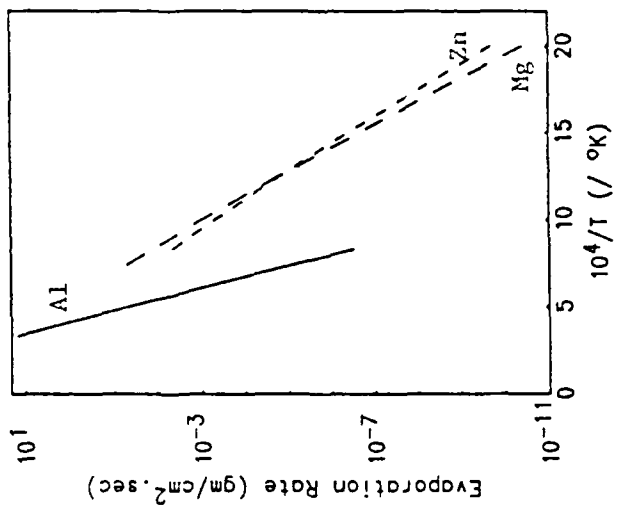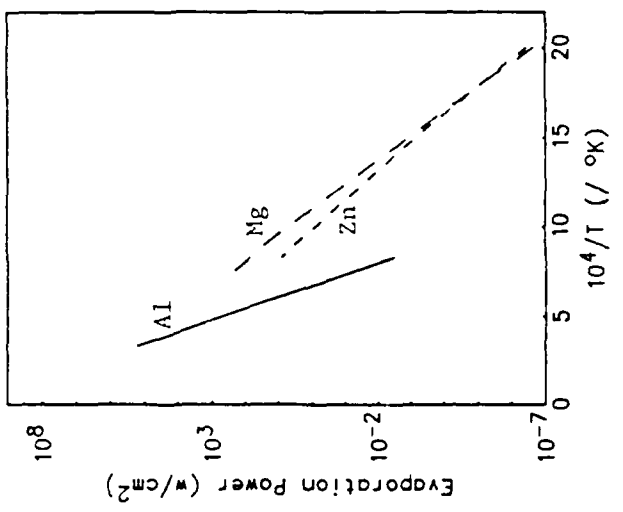
Figure 3.4 Vaporization plots for aluminum alloy 6061.

the plots of evaporation rates vs. temperature as shown in figures 3.1b to 3.4b, peak temperatures on the weld pool surface can be estimated from experimentally determined vaporization rates of any constituents. Khan and Debroy[46] employed a similar technique using ratios of vaporization rates of any two species in the weld pool to predict the peak temperatures in stainless steel welds.

Further, the plots of evaporation power vs. temperature shown in figure 3.1c to 3.4c can be helpful in calculating the temperature profiles around the heat source using known or assumed distribution of energy in the weld heat source, as was done by Block-Bolten et al.[45] The dominant specie in the vapor can also be identified at the power intensities involved. For instance, at power intensities of 3.54×10^5 to 1.95×10^6 w/cm^2 involved in laser welding, the dominant specie vaporizing in alloy 2219 is aluminum as seen in figure 3.1.c. However, for the other three alloys under investigation, there is a transition point where the extrapolated aluminum and magnesium lines intersect as shown in figures 3.2c to 3.4c. At intensities above this transition point, aluminum vaporization decides the temperature. But, at intensities below this transition point, magnesium is the dominant vaporization specie, and will determine the peak temperature. The phenomenon occurring in the weld pool are therefore intimately related to the power intensity as well as the alloy content. The results obtained from the vaporization studies are discussed in chapter 5.

Chapter 4

FINITE ELEMENT WELD HEAT CONDUCTION MODEL

Analysis of heat conduction in keyhole laser welds in aluminum alloys can lead to a better understanding of the influence of laser welding parameters on the weld bead characteristics. As discussed in chapter 2, the effect of convective heat transfer in the weld pool on the weld thermal profiles may be neglected for aluminum laser welds, and heat conduction can be used to predict the weld profiles with reasonable accuracy. A two-dimensional non-linear finite element weld heat transfer model was developed to predict the temperature distributions, thermal gradients and cooling rates in and around the weld. Although finite difference method is widely used in solidification studies in casting, finite element method has been chosen here to solve the weld heat transfer problem as it is more amenable to the non-linearities involved. In the following sections, the problem statement, the finite element formulation, and the results of the test problems solved for verifying the model are presented.

4.1 Problem Statement

The governing partial differential equation for transient heat flow with internal heat generation is

$$\frac{\partial}{\partial x}\left(k_x \frac{\partial T}{\partial x}\right) + \frac{\partial}{\partial y}\left(k_y \frac{\partial T}{\partial y}\right) + \frac{\partial}{\partial z}\left(k_z \frac{\partial T}{\partial z}\right) + \dot{Q} = \rho c \frac{\partial T}{\partial t} \qquad (4.1)$$

where T is the temperature, k_x, k_y and k_z the thermal conductivities in the x, y and z direction respectively, ρ the density, c the specific heat of the alloy, $\dot{Q}$ the internal heat source term, and t the time. In addition, the following relation holds on the surface:

$$k_n \left(\frac{\partial T}{\partial n}\right)_s = q^s, \qquad (4.2)$$

where n is the direction normal to the surface, and q^s the surface heat flux. Surface heat transfer as described by equation 4.2 can take the following three forms for a typical welding heat flow problem :

i. Convection heat transfer from the plate surfaces as given by

$$-q_c^s = h_c(T - T_a)$$

where T_a is the ambient temperature, h_c the convection heat transfer coefficient; h_c can be determined by the relation

$$h_c = N_u \frac{k_g}{L}$$

where N_u is the Nusselt number, k_g the thermal conductivity of air and L the characteristic length of the element.

ii. Radiation heat transfer as given by

$$-q_r^s = h_r(T - T_a)$$

the radiation heat transfer coefficient h_r being

$$h_r = \epsilon\sigma(T^2 + T_a^2)(T + T_a)$$

where ϵ is the emissivity and σ the Stefan-Boltzman constant.

iii. Surface heat flux, eg. the welding heat source, as described in section 2.4.2.3.

The two-dimensional heat transfer model described below can be used to analyze two types of welding problems. Figure 4.1 shows the geometry of the planar and the cross-sectional models that can be used with the corresponding coordinate systems. The planar model is used for full penetration welds in thin plates, and the heat flow in the thickness direction z is neglected. In such problems,
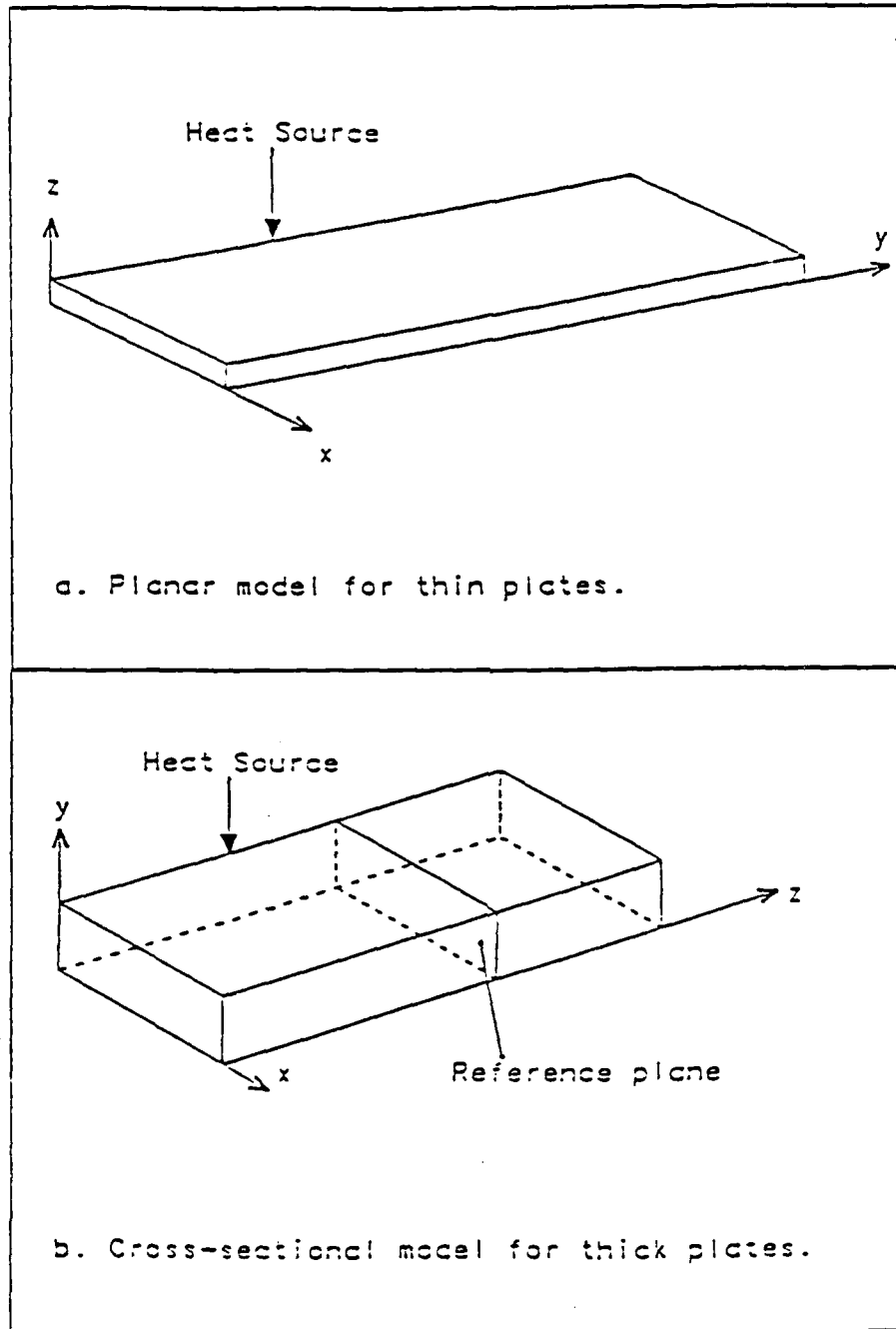
Figure 4.1   Two-dimensional weld geometry modeled.

the complete welding cycle including the initial transients and the end effects can be modeled. However, for partial penetration welds in thick plates, the cross-sectional model is employed in which the heat flow in the welding direction z is neglected. This assumption is valid for high welding speeds relative to the thermal diffusivity of the material.[69] Only the quasi-steady state conditions of the weld cycle – away from the end effects – can be modeled by the cross-sectional approach. Under such steady state conditions, the isotherms reach a steady state around the welding heat source and travel along the material at the speed of welding. In other words, following holds[70]

$$T(x, y, z, t) = T(x, y, z - vt).$$

Thus, a reference cross-sectional plane is modeled as the welding heat source approaches and passes over the plane, and the temperature distribution in the reference plane calculated at each successive time step. The model then allows a composite of the reference plane thermal histories to be assembled, giving a three-dimensional picture of the weld pool.

4.2 Variational Formulation

Although both the differential equation approach and the variational approach can be used for the finite element formulation of the transient heat conduction problem, the variational approach has been selected for developing this model. This formulation allows the complicated boundary conditions to be treated implicitly, and only the geometric or forced boundary conditions like specified temperatures need to be explicitly enforced.[71] The formulation used in the model described below is essentially the same as described by Bathe.[63,72,73] The

applicable functional Π for the variational formulation for the two-dimensional transient heat transfer problem described in section 4.1 is

$$\Pi = \int_v \left(\frac{1}{2} \left(k_x \left(\frac{\partial T}{\partial x} \right)^2 + k_y \left(\frac{\partial T}{\partial y} \right)^2 \right) \right) dV - \int_v T \left(\dot{Q} - \rho c \frac{\partial T}{\partial t} \right) dV$$

$$- \int_{s_1} T^s q^s dS + \int_{s_2} T^s q^s dS, \qquad (4.3)$$

s_1 being the area over which surface heat input occurs, and s_2 the area over which surface heat losses occur. The governing partial differential equation and the associated boundary conditions are derived by considering the stationarity of this functional. Thus, by minimizing the functional, the following integral equation is obtained describing the heat equilibrium at all times :

$$\int_v \delta \mathbf{T'}^{\tau} \, \mathbf{K} \, \mathbf{T'} \, dV = \int_{s_1} \delta T^s q^s dS - \int_{s_2} \delta T^s q^s dS + \int_v \delta T \left(\dot{Q} - \rho c \frac{\partial T}{\partial t} \right) dV, \quad (4.4)$$

where

$$\mathbf{K} = \begin{pmatrix} k_x & 0 \\ 0 & k_y \end{pmatrix}$$

and

$$\mathbf{T'}^{\tau} = \begin{pmatrix} \frac{\partial T}{\partial x} & \frac{\partial T}{\partial y} \end{pmatrix}.$$

Direct integration is used for the solution process whereby the time domain is divided into several small time steps, and the solution is successively obtained at each time step. Step-by-step incremental equilibrium equations are derived from equation 4.4 for the solution process, where knowing the temperature distribution in the material at time t, the new temperatures at the next time increment $t + \Delta t$ are calculated. Euler's backward implicit time integration scheme has been used where the heat flow equilibrium at time step $t + \Delta t$ is considered to solve for temperatures at that time step. This method has been selected as it guarantees

accuracy and unconditional stability. In this time stepping scheme, the time derivative is approximated as

$$^{t+\Delta t}\dot{T} = \frac{^{t+\Delta t}T - {}^{t}T}{\Delta t}. \tag{4.5}$$

The incremental equation described above is non-linear due to the temperature dependent thermal properties and the boundary conditions involved. The equation is linearized using the following definitions

$$^{t+\Delta t}T = {}^{t}T + \Delta T,$$

$$^{t+\Delta t}\mathbf{T}' = {}^{t}\mathbf{T}' + \Delta\mathbf{T}',$$

$$^{t+\Delta t}\mathbf{K} = {}^{t}\mathbf{K} + \Delta\mathbf{K},$$

$$^{t+\Delta t}\rho c = {}^{t}\rho c + \Delta\rho c,$$

$$^{t+\Delta t}h_{c,r} = {}^{t}h_{c,r} + \Delta h_{c,r}, \tag{4.6a}$$

and the following two assumptions :

$$^{t+\Delta t}\mathbf{K} \, {}^{t+\Delta t}\mathbf{T}' = {}^{t}\mathbf{K} \, {}^{t}\mathbf{T}' + {}^{t}\mathbf{K} \, \Delta\mathbf{T}'$$

$$^{t+\Delta t}h_{c,r}\left(^{t+\Delta t}T^{s} - {}^{t+\Delta t}T_{a}\right) = {}^{t}h_{c,r}\left(^{t}T^{s} + \Delta T^{s} - {}^{t+\Delta t}T_{a}\right). \tag{4.6b}$$

Due to the above simplifying assumptions, an iterative scheme has been incorporated for each time step to ensure accuracy. The modified Newton-Raphson iterative scheme has been used in which the coefficient matrices on the left hand side of the equation are not updated for each iteration. Thus, the temperature at the ith iteration is given by

$$^{t+\Delta t}T_{i} = {}^{t+\Delta t}T_{i-1} + \Delta T_{i}.$$

Incorporating the above linearization and the iterative scheme by substituting equations 4.6 and 4.7 into equation 4.4 results in

$$\int_v \delta T' \, {}^tK \, \Delta T'_i \, dV + \int_{S_{c,r}} \delta T^s \, {}^th_{c,r} \, \Delta T^s_i \, dS$$

$$= \int_{s_1} \delta T^s \, {}^{t+\Delta t}q^s \, dS - \int_{S_{c,r}} \delta T^S \, {}^{t+\Delta t}h_{c,r} \left({}^{t+\Delta t}T^s_{i-1} - {}^{t+\Delta t}T_a \right) dS$$

$$+ \int_v \delta T \, {}^{t+\Delta t}\left(\dot{Q} - \rho c \right)_i \, {}^{t+\Delta t}\left(\frac{\partial T}{\partial t} \right)_i \, dV - \int_v \delta T' \, {}^{t+\Delta t}K \, {}^{t+\Delta t}T'_{i-1} \, dV \quad (4.8)$$

Now, the finite element discretisation is introduced whereby the linearized incremental equations are transformed into a set of simultaneous equations. The region under consideration is divided into finite sized elements and the heat equilibrium applied over each of these elements. Two-dimensional quadrilateral isoparametric elements have been used in the model with a choice of four to eight nodes. For any element m, the following discretisation is assumed using space interpolation functions H_m and the gradient factions B_m as defined in table 4.1 :

$$^{t+\Delta t}T_m = H_m \, {}^{t+\Delta t}T,$$

$$^{t+\Delta t}T^s_m = H^s_m \, {}^{t+\Delta t}T,$$

$$^{t+\Delta t}T'_m = B_m \, {}^{t+\Delta t}T. \quad (4.9)$$

Substituting equation 4.9 into equation 4.8 results in a set of simultaneous equations of the form

$$\left({}^tK + \frac{1}{\Delta t} {}^tC \right) \Delta T_i = {}^{t+\Delta t}\tilde{Q}_{i-1} - {}^{t+\Delta t}C_{i-1} \, {}^{t+\Delta t}\dot{T}_{i-1}. \quad (4.10)$$

The individual terms involved in equation 4.10 are described in table 4.2. The integration involved in each of these terms is carried out using the Gaussian quadrature. Temperature dependent material thermal properties are determined

Table 4.1. Interpolation functions used for up to 8 nodes quadrilateral isoparametric elements.
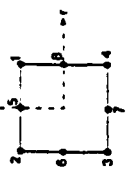
(Note : Only m functions needed for a m nodes element, m = 4 to 8)

	Only for 4 nodes elements	Include for upto 5 nodes elements	Include for upto 6 nodes elements	Include for upto 7 nodes elements	Include for upto 8 nodes elements
H(1)	$\frac{1}{4}(1+r)(1+s)$	$-\frac{1}{4}(1-r^2)(1+s)$	–	–	$-\frac{1}{4}(1+r)(1-s^2)$
H(2)	$\frac{1}{4}(1-r)(1+s)$	$-\frac{1}{4}(1-r^2)(1+s)$	$-\frac{1}{4}(1-r)(1-s^2)$	–	–
H(3)	$\frac{1}{4}(1-r)(1-s)$	–	$-\frac{1}{4}(1-r)(1-s^2)$	$-\frac{1}{4}(1-r^2)(1-s)$	–
H(4)	$\frac{1}{4}(1+r)(1-s)$	–	–	$-\frac{1}{4}(1-r^2)(1-s)$	$-\frac{1}{4}(1+r)(1-s^2)$
H(5)	$\frac{1}{2}(1-r^2)(1+s)$	–	–	–	–
H(6)	$\frac{1}{2}(1-r)(1-s^2)$	–	–	–	–
H(7)	$\frac{1}{2}(1-r^2)(1-s)$	–	–	–	–
H(8)	$\frac{1}{2}(1+r)(1-s^2)$	–	–	–	–
H	$\begin{Bmatrix} \frac{\partial}{\partial x} \\ \frac{\partial}{\partial y} \end{Bmatrix} =$				

50

Table 4.2. Expressions involved in equation 4.10.

Terms	Expressions
${}^{t}\mathbf{K}$	$\int_{v} \mathbf{B}^{\tau}\ {}^{t}\mathbf{K}\ \mathbf{B}\ dv + \int_{s_{c,r}}\ {}^{t}h_{c,r}\ \mathbf{H}_{s}^{\tau}\ \mathbf{H}_{s}\ ds$
${}^{t}\mathbf{C}$	$\int_{v} \mathbf{H}^{\tau}\ {}^{t}\mathbf{C}\ \mathbf{H}\ dv$
${}^{t+\Delta t}\dot{\mathbf{T}}_{i-1}$	$\dfrac{{}^{t+\Delta t}T_{i-1} - {}^{t}T}{\Delta t}$
${}^{t+\Delta t}\bar{\mathbf{Q}}_{i-1}$	${}^{t+\Delta t}\bar{Q}_{v} + {}^{t+\Delta t}\bar{Q}_{s} - {}^{t+\Delta t}\bar{Q}_{c,r,(i-1)} - {}^{t+\Delta t}\bar{Q}_{k,(i-1)}$
where ${}^{t+\Delta t}\bar{\mathbf{Q}}_{v}$	$\int_{v} \mathbf{H}\ {}^{t+\Delta t}\dot{Q}\ dv$
${}^{t+\Delta t}\bar{\mathbf{Q}}_{s}$	$\int_{s_{1}} \mathbf{H}\ {}^{t+\Delta t}q_{s}\ ds$
${}^{t+\Delta t}\bar{\mathbf{Q}}_{c,r,(i-1)}$	$\int_{s_{c,r}}\ {}^{t+\Delta t}h_{c,r}\ \mathbf{H}_{s}^{\tau}\ \mathbf{H}_{s}\left({}^{t+\Delta t}T_{i-1} - {}^{t+\Delta t}T_{a}\right)\ ds$
${}^{t+\Delta t}\bar{\mathbf{Q}}_{k,(i-1)}$	$\int_{v} \mathbf{B}^{\tau}\ {}^{t+\Delta t}K_{i-1}\ \mathbf{B}\ {}^{t+\Delta t}T_{i-1}\ dv$

at the gauss points based on the temperatures at the previous iteration. The set of simultaneous equations are then solved for each time step using Gauss-Siedel method iterating till the maximum temperature increment is within a preset tolerance limit.

4.3 Weld Heat Source Distribution

Numerical welding heat transfer models using Pavelic's surface heat flux model[14] as described by equation 2.6 have been reasonably successful for modeling the arc welding processes. This model is not valid for deep penetration welds where the thermal energy is deposited deep inside the material. Goldak et al.[19] used the double ellipsoid model described by equation 2.7 to solve the thermal flow problem in a submerged arc weld and an electron beam weld. Although, the results for the submerged arc weld were satisfactory, the deep penetration electron beam weld was under-predicted by over 40%. Majumder et al.[17] and Chande et al.[18] used a surface gaussian heat source in their three-dimensional finite difference model for laser welding, with the modification that once a node reached the boiling point, it became transparent and allowed the laser energy to pass through (reflectivity 0). They assumed the energy absorption to follow the Beer-Lambert's law as described by equation 2.8. This model may be a good attempt to simulate the physical phenomenon of the creation of the keyhole. But, it may not accurately represent the conditions when the established keyhole is traversed relative to the laser beam, and the energy is deposited deep inside the keyhole.

A variation of the above two models was used in the present study, in which the laser weld heat input was incorporated as an internal heat source rather than a surface flux using the following relation

$$q(r,y) = q_0 \, e^{-c_1 r^2} \, e^{-c_2 y} \qquad (4.11)$$

Thus, the heat source was assumed to have a gaussian distribution in the radial direction and with exponential decay in the thickness direction. Effective radius and depth of the energy source, r_0 and y_0 respectively, were assumed where the intensity fell to 5% of the peak value. The various constants in the equation 2.8, calculated by limited the integration to r_0 and y_0, are :

$$c_1 = \frac{3}{r_0^2}$$

$$c_2 = \frac{3}{y_0}$$

$$q_0 = \frac{9\,\alpha\,Q}{\pi\,r_0^2\,y_0}$$

where α is the absorptivity of the material to the laser energy, and Q the laser power input. The internal heat source model described above was used to model deep penetration keyhole welds in electron beam and laser welding processes, and the results are presented in later sections.

4.4 Finite Element Program THERM

The two-dimensional non-linear transient heat conduction formulation presented in the previous section was used to develop a non-linear finite element thermal analysis program called THERM. The program has been coded in FORTRAN language and has been developed on a Data General Eclipse MV/10000 system with AOS/VS 7.54 operating system. THERM is also operational on a VAX 11/782 system operating under VMS version 4.6 operating system. The program accommodates temperature dependent thermal properties, a finite weld heat source either as a surface heat flux or as an internal heat source, convection and radiation heat losses, convection in the molten metal treated as an apparent increase in the thermal conductivity, and latent heat of fusion treated either as an apparent increase in the specific heat of the material, or by the enthalpy method.

The program THERM includes a general thermal element library of isoparametric quadrilateral elements with a choice of four to eight nodes to model linear or non-linear heat transfer problems. For the cross-sectional models, the elements allow either individual edges or combination of two adjacent edges to have convective or radiative boundaries. For the planar model, either of the two faces of the elements may have convection or radiation boundaries. The same holds for the surface heat flux.

The program allows the region being modeled to consist of up to five different materials. For each of these materials, the temperature dependent thermal properties like thermal conductivity, volumetric specific heat and the enthalpy may be specified at up to five different temperatures. The program linearly interpolates within each of these temperature regimes. The program therefore can also be used for solving heat transfer and solidification problems in composite materials, which in addition may have non-isotropic properties.

An example of the program input data set giving the welding conditions and the material properties is described in the appendix A. Also described is an example of the input mesh data set with explanation about the automatic generation features for nodal coordinates as well as element connectivity in the finite element mesh.

4.5 Testing and Verification of the Model

The finite element program THERM was tested for accuracy by solving several general heat transfer problems, one and two-dimensional solidification problems in castings, heat transfer in different welding processes like arc welding, submerged arc welding, electron beam welding and laser welding. The results obtained from THERM were compared with published analytical, numerical or experimental

results. Following sections present the results of some of the relevant test problems solved.

4.5.1 Integration Scheme

As mentioned in chapter 2, the time marching scheme most widely used for the transient heat flow problems is the Crank-Nicholson (central difference) scheme. However, at large time steps, this method can result in stability problems. Bathe[63] has shown that the Euler's backward implicit method results in unconditional stability. However, he did not present any numerical results to confirm this fact and the accuracy of this method. Myers[62] has compared the finite difference and the finite element methods using the Crank-Nicholson and the Euler's forward explicit method with respect to the largest time step allowed, accuracy of the results and the stability of the time marching scheme. He used a transient heat conduction problem of a square slab of sides l with unequal initial temperature distribution as described by the equation

$$t(x,y,0) = \begin{cases} T_0\left(\frac{l-x}{l}\right) & for \quad x \geq y \\ T_0\left(\frac{l-y}{l}\right) & for \quad x \leq y \end{cases}$$

The same problem has been used to test the Euler's backward method used in THERM, and the results compared with those obtained by Myers. The time marching schemes compared are described by the following expressions :

i. Euler's forward (explicit) method :

$$T_{i+1} = T_i + \dot{T}_i \times \Delta t. \tag{4.12a}$$

ii. Euler's backward (implicit) method :

$$T_{i+1} = T_i + \dot{T}_{i+1} \times \Delta t. \tag{4.12b}$$

iii. Crank-Nicholson's (central difference) method :

$$T_{i+1} = T_i + (\dot{T}_i + \dot{T}_{i+1}) \times \frac{\Delta t}{2}. \qquad (4.12c)$$

After the usual discretisation procedure of equation 4.1 by either the finite difference or the finite element method, the following set of simultaneous differential equations are obtained :

$$C\,\dot{T} + K\,T = R. \qquad (4.13)$$

Incorporating the time stepping schemes shown in equation 4.11 into equation 4.12 results in a set of simultaneous equations of the form :

$$A\,T_{i+1} = B\,T_i + R \times \Delta t \qquad (4.14)$$

where the matrices A and B for each of the time marching techniques being tested are described in table 4.3 below.

Table 4.3. Expressions involved in equation 4.13.

Integration Scheme	A	B
Euler's explicit	C	$C - K\,\Delta t$
Euler's implicit	$C + K\,\Delta t$	C
Crank-Nicholson	$C + K\,\frac{\Delta t}{2}$	$C - K\,\frac{\Delta t}{2}$

The vector R in equation 4.12 is a null vector as there is no nodal heat flux in this problem and the boundary conditions are homogeneous. The time step used for the different schemes was determined from the relationship

$$\Delta t = \frac{l^2}{k\,\alpha}$$

where k is a constant, α the thermal diffusivity assumed constant, and l the element-dimension – in this case of one element problem, the dimension of the slab. Myers has shown that the time step depends not only on the integration scheme used, the material thermal properties and the mesh size, but also on the type of element used and the boundary conditions applied.

The solution obtained by the finite element method using the consistent C are shown in figure 4.2 for the Euler's implicit and the Crank-Nicholson methods. The figure shows the temperature response at the four corners of the slab as a function of time for $k = 36$. The Euler's implicit method shows excellent matching with the exact solution whereas the Crank-Nicholson's method has a much faster time response. This tendency is further enhanced for larger time steps represented by smaller k of 18. For this case, the Euler's explicit method showed severe instability, whereas the Euler's implicit as well as the Crank-Nicholson were still stable. However, at $k = 9$, even the Crank-Nicholson started to become unstable as seen in figure 4.3, while the Euler's implicit is still stable, although the time response is slower than at $k = 36$ or 18.

All solutions using the finite element formulation converged to a nodal temperature of $\frac{T_0}{3}$ for all four corners just as the exact solution does. But, the finite difference solutions converged to the inaccurate solution of $\frac{T_0}{4}$. Further, the time response of the finite difference solutions is much slower than the exact solution as shown in figure 4.4 even for a small time step corresponding to $k = 36$. The Crank-Nicholson and the Euler's implicit methods give identical solutions for the finite difference formulation. At larger time steps, the solutions deviate slightly from each other, although they are always stable. Only the Euler's explicit solution became unstable at $k = 4$.
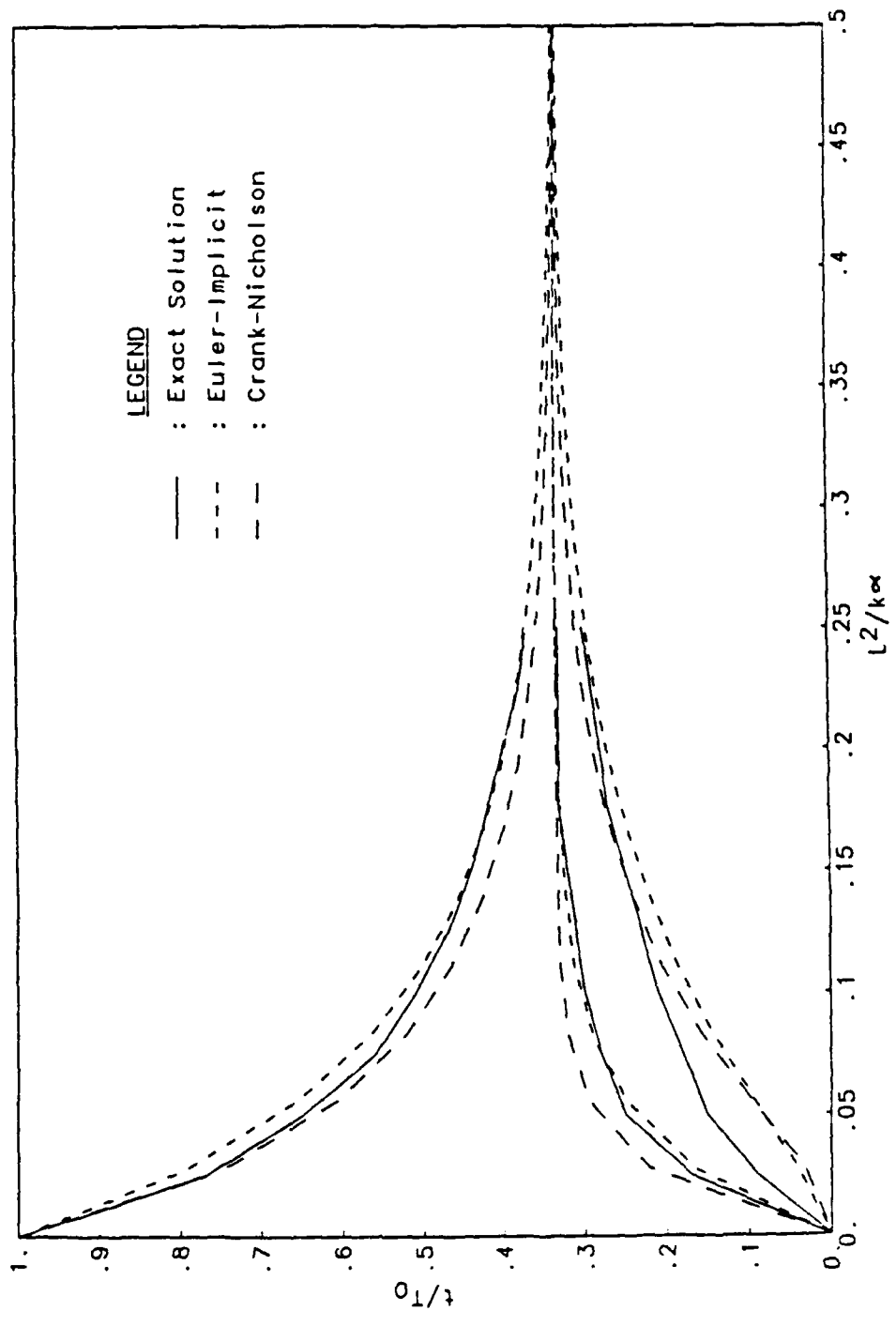
Figure 4.2 Temperature response in slab using consistent C (k=36).
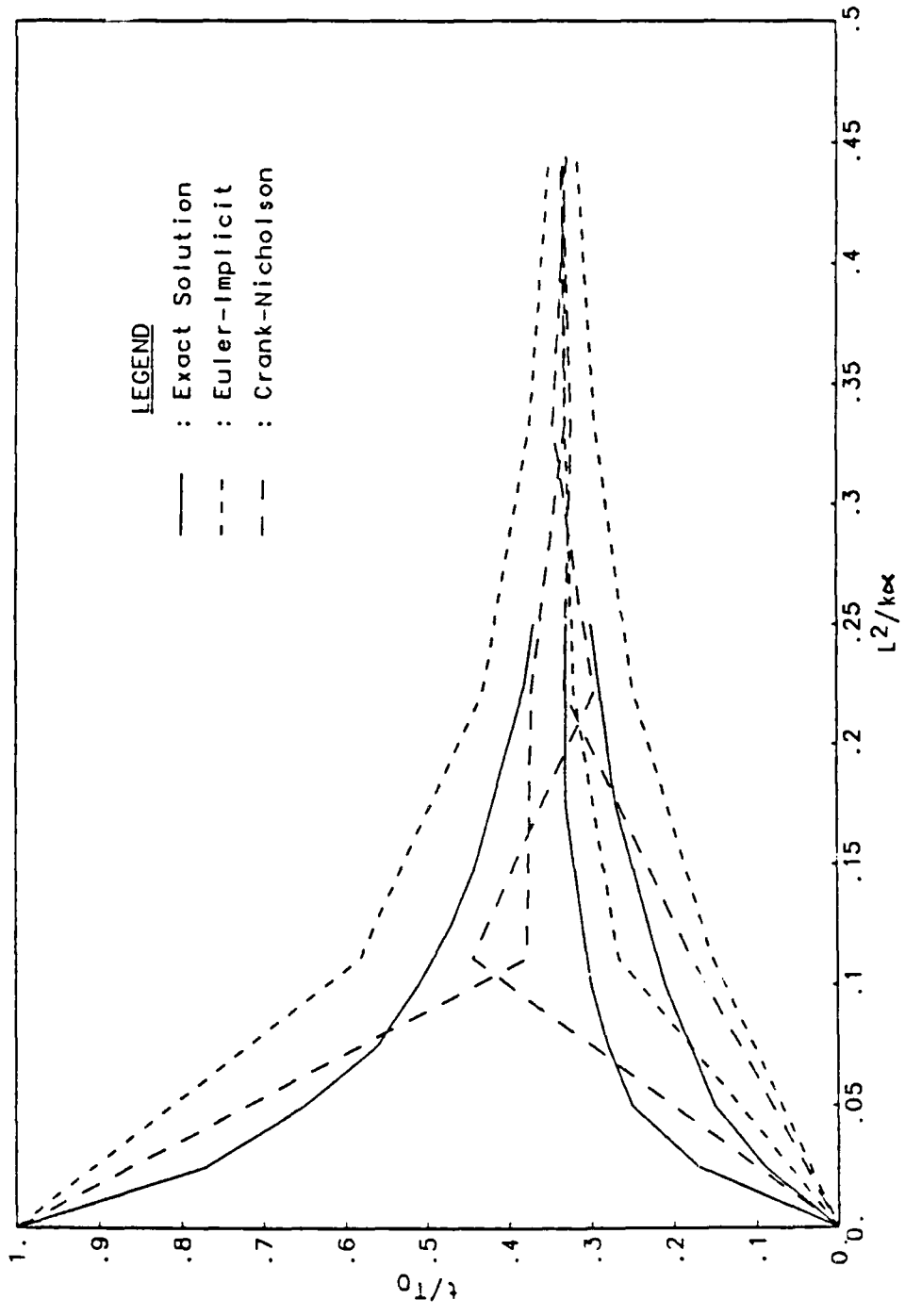
Figure 4.3 Temperature response in slab using consistent C (k=9).
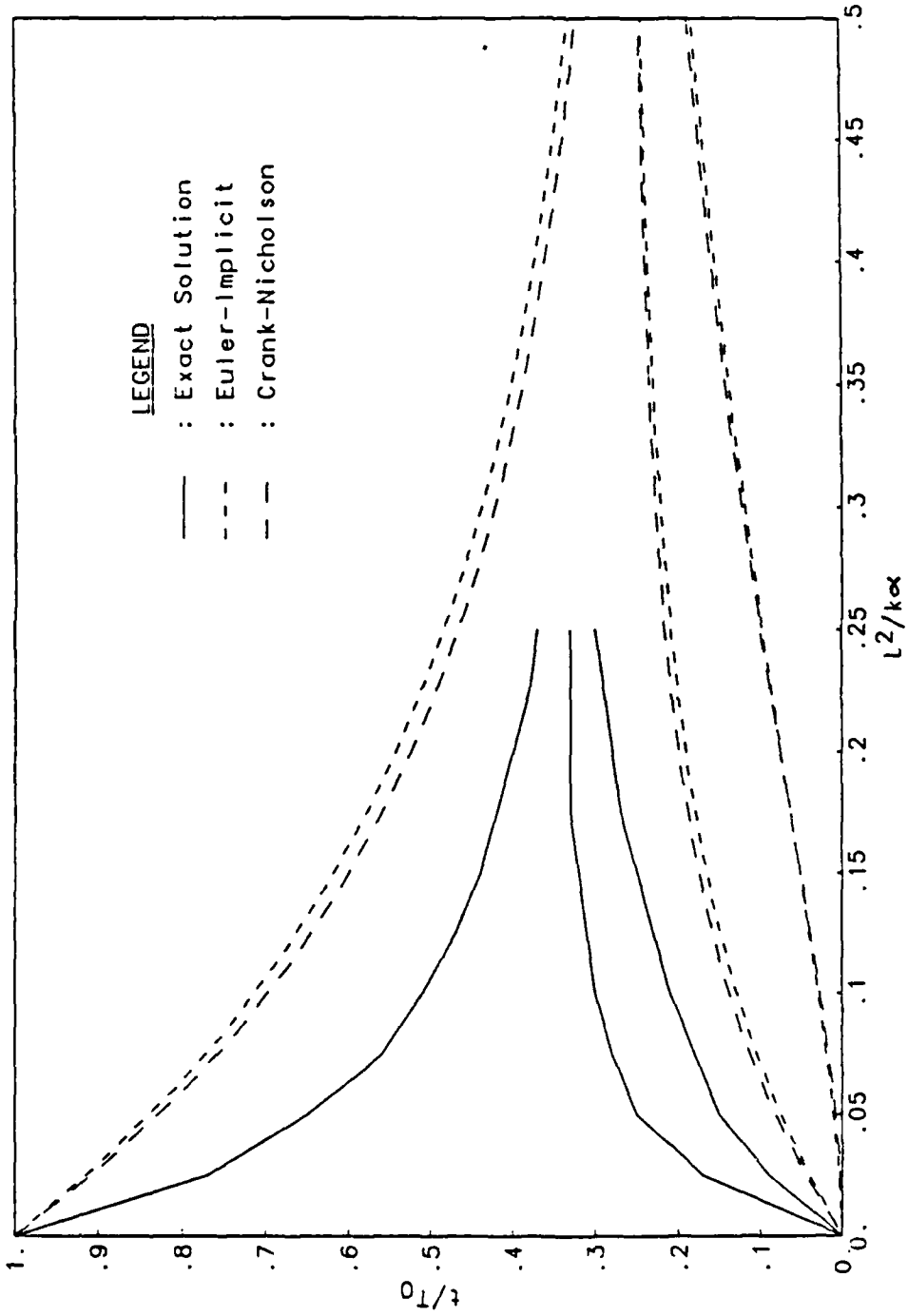
Figure 4.4   Temperature response in slab using lumped C (k=36).

Thus, the Euler's implicit method combined with the finite element method was found to be accurate and unconditionally stable as compared to the Euler's explicit or the Crank-Nicholson's methods. For the finite difference formulation with the lumped heat capacity matrix, both the Euler's implicit and the Crank-Nicholson's methods performed equally well.

4.5.2 One-Dimensional Solidification

Weiner[74] presented the analytical solution for a one-dimensional solidification of a molten half space, which has been used by many researchers for testing and verifying their numerical heat transfer models. For instance, Comini[60] solved the freezing of water, Hsiao[58] presented the solution for solidification of a superheated liquid, and Hibbit[75] solved the Weiner's problem of solidification of molten steel. THERM was tested by solving each of these problems with excellent results matching with the analytical solutions. Here, the comparison with the Weiner's problem of steel solidification is presented as it models a simple but realistic freezing problem. A half space of molten steel initially at a uniform temperature of 2845 °F is suddenly brought into contact with a half space of chill at a uniform temperature of 70 °F made of the same material. The geometry of the problem and the finite element mesh of 33 elements and 68 nodes used to model the problem is shown in figure 4.5. The material thermal properties and the initial conditions assumed are as follows :

Thermal Conductivity (solid)	: 4.26×10^{-4} btu/in sec °F;
Thermal Conductivity (liquid)	: 2.13×10^{-4} btu/in sec °F;
Vol. Specific Heat (solid)	: 4.47×10^{-2} btu/in^3 °F;
Vol. Specific Heat (liquid)	: 5.21×10^{-2} btu/in^3 °F;
Latent Heat of Fusion	: 33.56 btu/in^3;
Solidus Temperature	: 2600 °F;

*** ONE DIMENSIONAL SOLIDIFICATION -- WEINER ***

Mesh Used for Finite Element Analysis.

Alloy : 0.   Power (kw): 0.   Eff : 0.   Time   (sec): 0.
Focus : 0.   Speed (cm/s): 0.   Yo : 0.   Position (cm): 0.
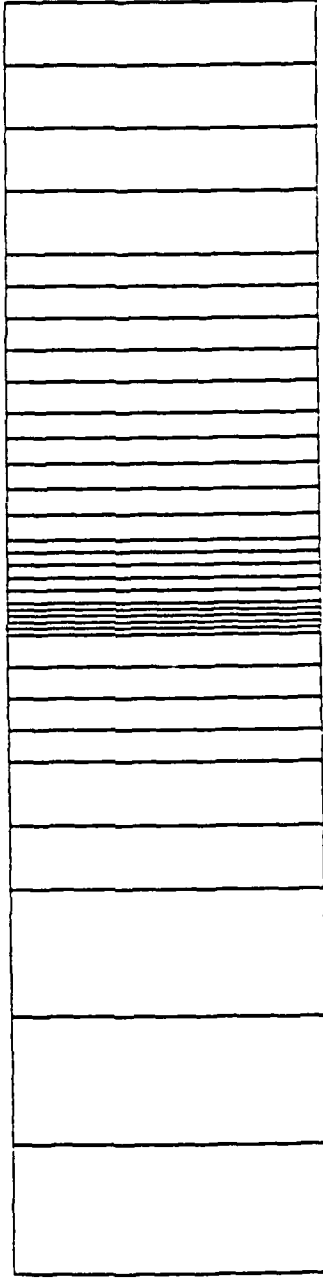
Figure 4.5 Mesh used for analyzing 1-dimensional solidification.

Liquidus Temperature	: 2700 °F;
Initial Temperature of Cast	: 2845 °F;
Initial Temperature of Chill	: 70 °F.

Figure 4.6 shows the location of the solidification front as a function of time. The prediction of the front by THERM is seen to be in good agreement with the analytical solution of Weiner as well as the finite element solution of Hibbit. Further refinement of the mesh to 44 elements and 90 nodes did not improve the solution indicating that the solution has converged. The lumped and the consistent heat capacity approaches were tested using the medium mesh with no significant difference. Also, the modified Newton-Raphson's iterative scheme was compared with the full Newton-Raphson' scheme where the coefficient matrices are updated for each iteration, again with no significant difference.

Figure 4.7 shows the temperature profiles in the cast and the chill close to the interface at different times. Weiner's analytical solution requires an assumption of temperature continuity as well as a gradient condition at the interface. The finite element solution needs no such boundary conditions, but the temperature profiles show that the assumption is predicted by the model although the constant temperature point has shifted slightly into the cast. As the solution must start with the molten element in contact with the chill to be at same temperature as the chill, the solidification front initiates some distance from the interface. Over-prediction of the solidus at the initial stages is therefore unavoidable as seen in figure 4.6. At larger times, the error decreases considerably.

4.5.3 Two-Dimensional Solidification

The next problem with increased complexity is the two-dimensional solidification of ingots. A cross-section of the ingot is modeled to predict the location of the
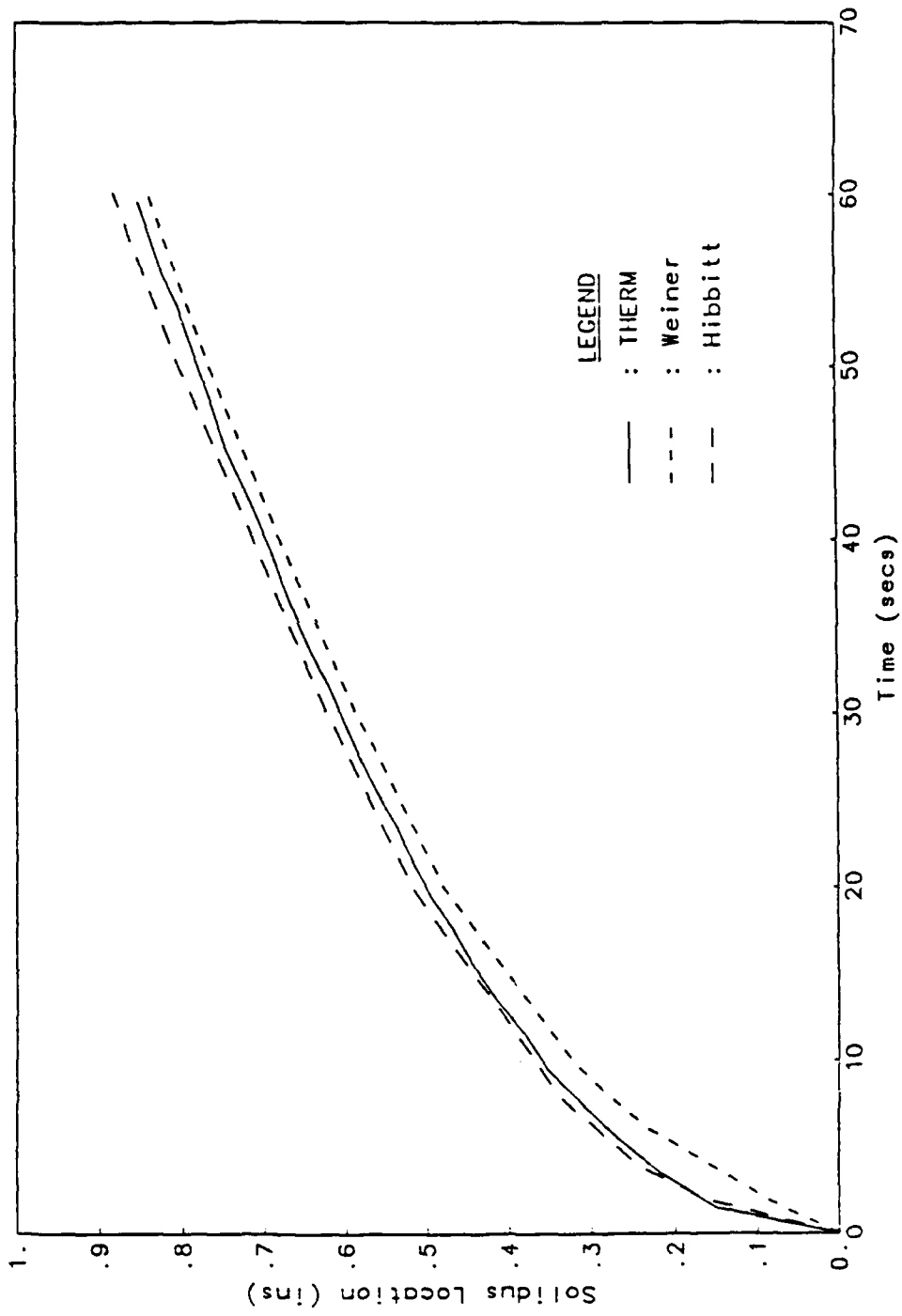
Figure 4.6 Location of solidus in 1-dimensional solidification.
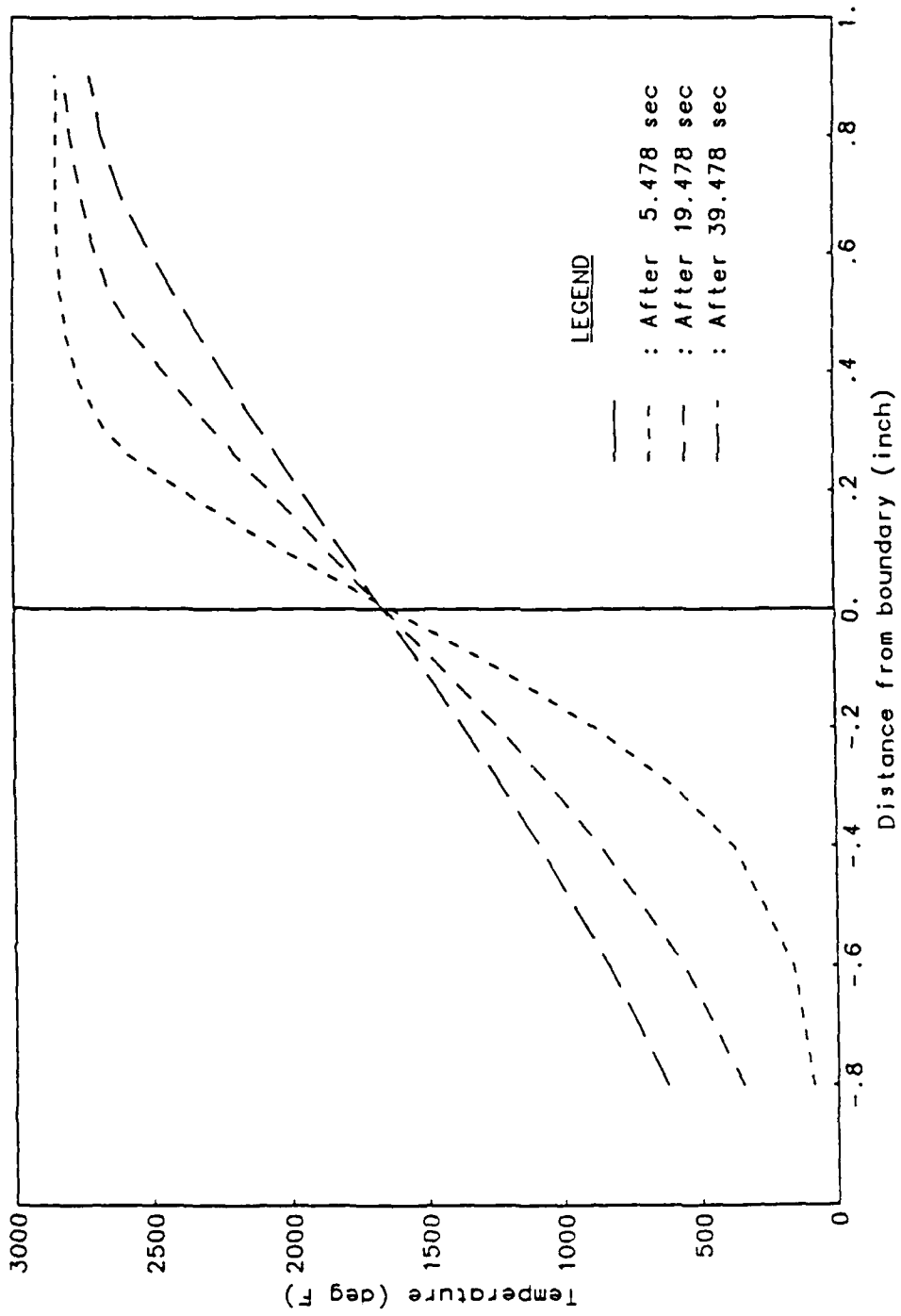
Figure 4.7 Temperature distribution in chill and melt.

solidification front as a function of time for a superheated liquid with convective boundaries. Lazardis[76] has presented a finite difference solution to this problem in which the location of the interface is determined by methodically enforcing the continuity of temperatures in the solid and liquid regions, and a relation for temperature gradients involving the latent heat of fusion. Hsiao[58] presented a finite difference solution to the same problem without such a rigorous approach. THERM was used to solve the problem with excellent matching and the results are presented below.

A $5' \times 5'$ square quadrant of a large ingot was modeled utilizing the symmetry in x and y direction. Two different meshes were attempted – one a uniform mesh of 10×10 elements, and the second a non-uniform mesh of 10×10 elements, with smaller elements near the ingot boundary. The material thermal properties and initial conditions assumed are presented below :

Thermal Conductivity (solid)	: 1.0×10^{-4} btu/in sec °F;
Thermal Conductivity (liquid)	: 0.9×10^{-4} btu/in sec °F;
Vol. Specific Heat (solid)	: 1.0×10^{-2} btu/in^3 °F;
Vol. Specific Heat (liquid)	: 1.0×10^{-2} btu/in^3 °F;
Latent Heat of Fusion	: 350 btu/in^3;
Convection Heat Transfer Coeff.	: 2 btu/in^2 sec °F;
Solidus Temperature	: 799 °F;
Liquidus Temperature	: 801 °F;
Initial Temperature of Cast	: 1000 °F;
Ambient Temperature	: 100 °F.

Figure 4.8 shows the location of the solidification front at times 0.4, 1.0 and 2.0 seconds as predicted by THERM using the non-uniform mesh, as well as the
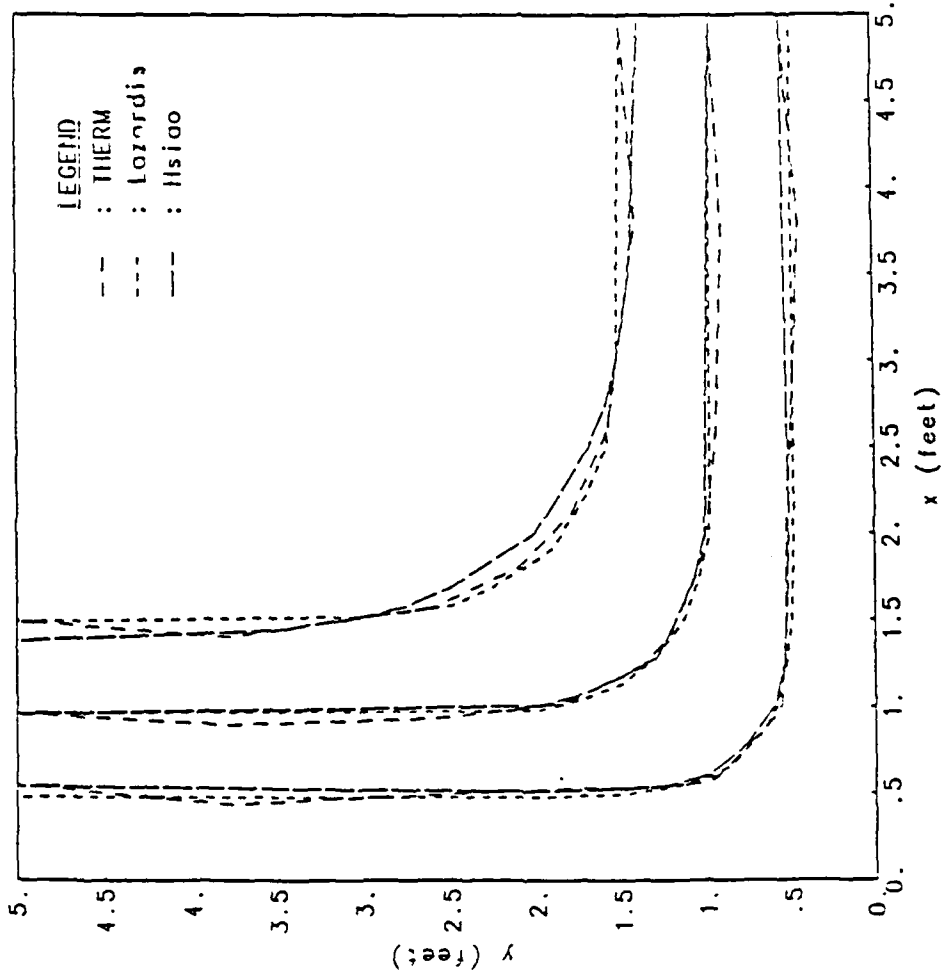
Figure 4.8 Location of solidus in 2-dimensional solidification.

solutions of Lazardis and Hsiao. The predicted results are in good agreement with those of Lazardis and Hsiao.

4.5.4 Thermal Analysis of an Arc Weld

The problem of heat flow and solidification in an arc weld was next solved to test THERM – especially the routines involving welding heat flux over a section of the boundary. Friedman[70] has presented a finite element solution for the longitudinal butt weld in 0.254 cm × 4.0 cm plates of inconel alloy 600 with a heat input of 703 watts and welding speed of 0.212 cm/sec. A mesh of 67 elements and 100 nodes, shown in figure 4.9 was used for analyzing the weld; it ensured at least six elements within the effective radius of the heat source. A uniform time step of 0.01 sec was used from the start of the thermal analysis till the end. No iterations were necessary within the time step before melting, and convergence was achieved usually within three iterations after melting occurred. The temperature dependent thermal properties and the initial conditions assumed are

Thermal Conductivity at 300 °K	:	0.1465 w/cm °K;
Thermal Conductivity at 1690 °K	:	0.3756 w/cm °K;
Thermal Conductivity at 1690 °K	:	0.1878 w/cm °K;
Vol. Specific Heat at 300 °K	:	3.7678 j/cm^3 °K;
Vol. Specific Heat at 1690 °K	:	6.2057 j/cm^3 °K;
Latent Heat of Fusion	:	2604.87 j/cm^3;
Emissivity	:	0.95;
Solidus Temperature	:	1630 °K;
Liquidus Temperature	:	1690 °K;
Initial and Ambient Temperature	:	300 °K.

*** TEMPERATURE DISTRIBUTION IN FUSION WELDS ***

Contour Values : 1690.

| Alloy : 600. | Power (kw): .703 | Eff : 1. | Time (sec): 4.09 |
| Focus : 0. | Speed (cm/s): .212 | Y0 : 0. | Position (cm): .3571 |

Figure 4.9 Mesh used for thermal analysis of arc weld.

Friedman used Pavelic's disk model of surface heat flux, and assumed the effective radius r_0 of the arc to be 0.508 cm. He used a simplified approach to incorporate the heat flux on the relevant element boundaries – he applied the welding heat as a uniform 'pressure' composed of two parts, one constant and the other varying with time.[77] Further, he assumed that the heat flux was applied for times $\pm \frac{r_0}{v} \times 1.5$ where v is the welding speed. In the present analysis by THERM, the heat flux is incorporated more accurately by determining the intensities at each gauss point of the elements concerned, and using the gaussian quadrature as shown in table 4.2. Also, as the arc influences the reference plane only when it is $\pm r_0$ distance from the plane, the heat flux was applied only for the duration $\frac{r_0}{v}$ seconds before and after the heat source crosses the reference plane. Thus, Friedman's temperature response is expected to be spread out over a longer duration, and have lower peak temperatures. Figure 4.10 shows the temperature response at 0. and 0.254 cm from the weld centerline at the top and bottom surface of the plate. The peak temperature predicted by THERM is higher by 280 °K at the arc center and slightly varying elsewhere.

As mentioned in section 4.1, the cross-sectional model allows the weld cross-sectional profiles to be calculated at successive time steps as the welding heat source approaches and passes over the reference plane. From a composite of these thermal histories, a three-dimensional shape of the molten pool can be obtained. Using such a composite, the weld pool shapes at the top and bottom surfaces of the plate was determined and are shown in figure 4.11. Here, the z-axis represents the longitudinal axis of or the weld travel axis with the origin of the coordinate system attached to the center of the weld heat source. Thus $z = 0$ represents the location of the arc center with the arc travelling in the negative z direction. It is to be noted that the maximum bead width occurs slightly behind the arc center,
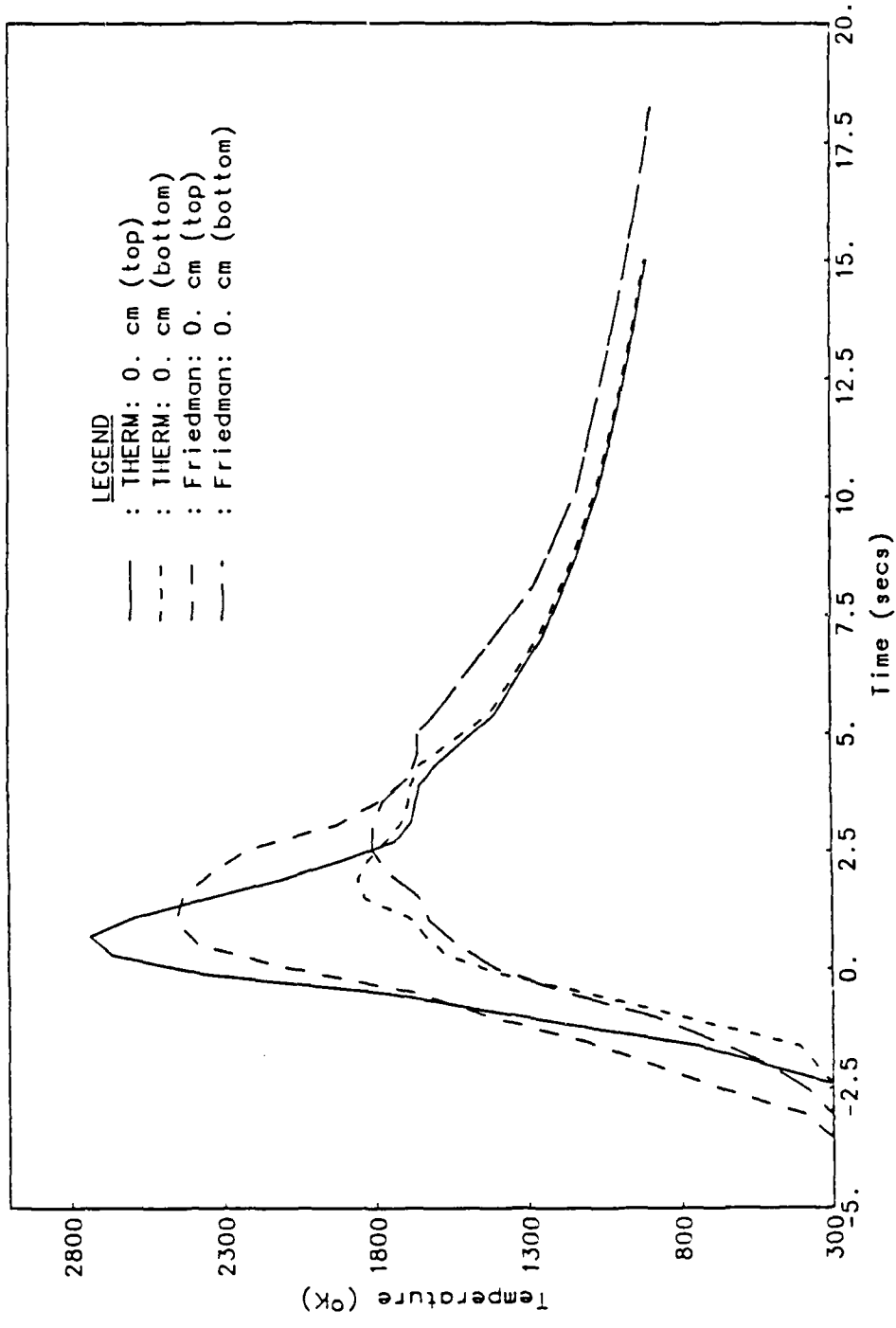
Figure 4.10   Temperature response in arc weld.
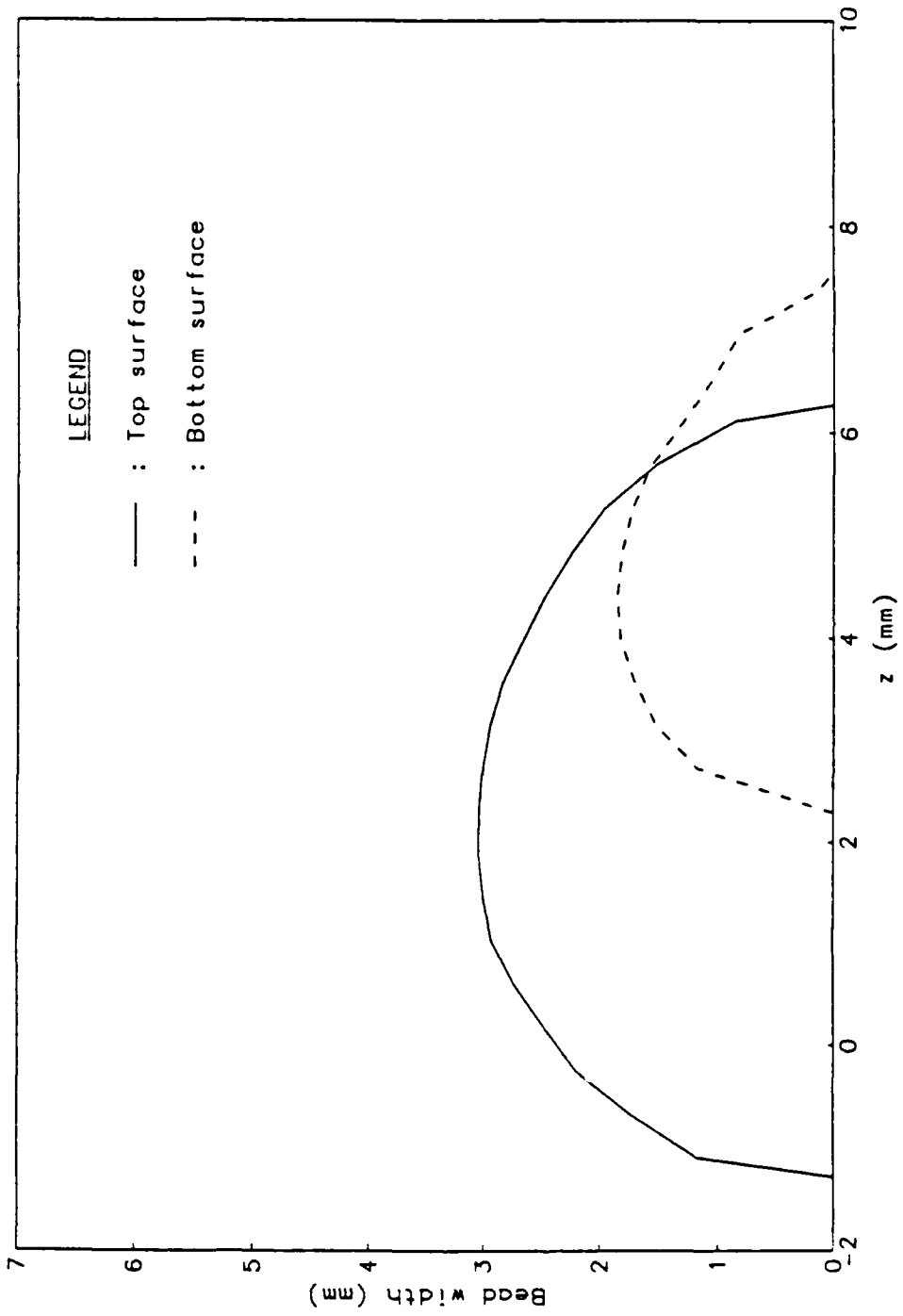
Figure 4.11 Predicted bead shape in arc weld.

and the maximum bead widths at the top and bottom surface do not occur in the same plane. Figure 4.12 compares the weld profile (liquidus isotherm) predicted by THERM and Friedman; prediction by THERM differs from Friedman's solution at most by 9%.

4.5.5 Heat Transfer in a Submerged Arc Weld

A submerged arc weld in a 10 cm thick carbon steel plate was modeled using THERM. Christensen et al.[51] has presented experimental temperature measurements at different locations in and around the fusion zone, as well as the weld and heat affected zone profiles. The problem has also been solved using the finite element method by Goldak et al.[19] using the double ellipsoid model and by Krutz[78] using Pavelic's disk model. The welding conditions are 38.5 kw power, 0.5 cm/sec welding speed with an efficiency of 0.95. For modeling this shallow weld with a maximum penetration of about 1.3 cm, the surface heat flux model was used in the THERM analysis with an effective radius r_0 of 2.0 cms. Thermal properties used are

Thermal Conductivity at 25 °C	: 0.515 w/cm °C;
Thermal Conductivity at 570 °C	: 0.379 w/cm °C;
Thermal Conductivity at 820 °C	: 0.249 w/cm °C;
Thermal Conductivity at 1482 °C	: 0.317 w/cm °C;
Thermal Conductivity at 1482 °C	: 1.268 w/cm °C;
Vol. Specific Heat at 25 °C	: 3.476 j/cm^3 °C;
Vol. Specific Heat at 450 °C	: 4.667 j/cm^3 °C;
Vol. Specific Heat at 750 °C	: 6.619 j/cm^3 °C;
Vol. Specific Heat at 940 °C	: 5.070 j/cm^2 °C;
Vol. Specific Heat at 1550 °C	: 5.863 j/cm^3 °C;
Latent Heat of Fusion	: 2100 j/cm^3;
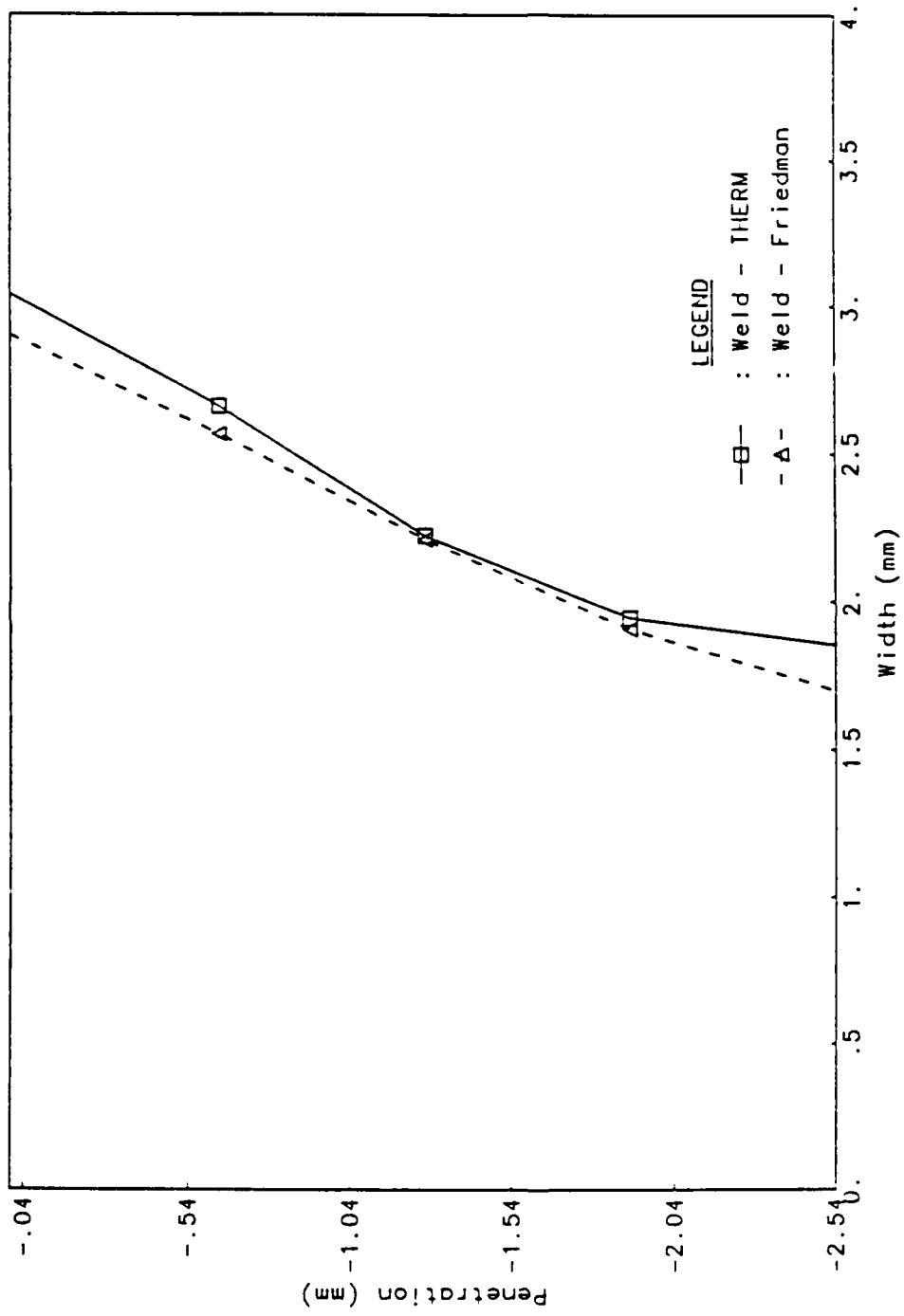
Figure 4.12   Predicted cross-section of arc weld.

Emissivity : 0.9;

Solidus Temperature : 1427 °C;

Liquidus Temperature : 1482 °C;

Initial and Ambient Temperature : 25 °C.

Figure 4.13 compares the calculated weld and HAZ profiles with the experimental results of Christensen; the predictions are in good agreement with the experimental results. Figure 4.14 shows the temperature profiles on the top surface of the plate 11.5 seconds after the arc has passed the reference plane. Again, the calculated temperature profile compares favorably with the experimental results.

4.5.6 Weld Profile in an Electron Beam Weld

The next problem analyzed was an electron beam weld in 1.95 cm thick carbon steel plate, and results compared with those of Goldak et al.[19] with the double ellipsoid model and the experimental results of Chong[79]. The power used was 2.8 kw, the welding speed was 0.53 cm/sec, with a process efficiency of 0.95. The effective radius of the gaussian electron beam was assumed to be 0.0508 cm, and the effective depth of the internal heat source model was assumed equal to the plate thickness. A finite element mesh of 137 elements and 172 nodes was used for modeling the 6.8 cm wide plate, with a finer mesh of element size 0.02 cm near the weld source, and a progressively coarser mesh away from the weld zone. Same temperature dependent material properties as assumed for the submerged arc weld were used in this problem.

Figure 4.15 and 4.16 show the weld profiles and the heat affected zone profiles as predicted by THERM compared to the predictions of Goldak and the experimental results. It is seen that the THERM predictions match well compared
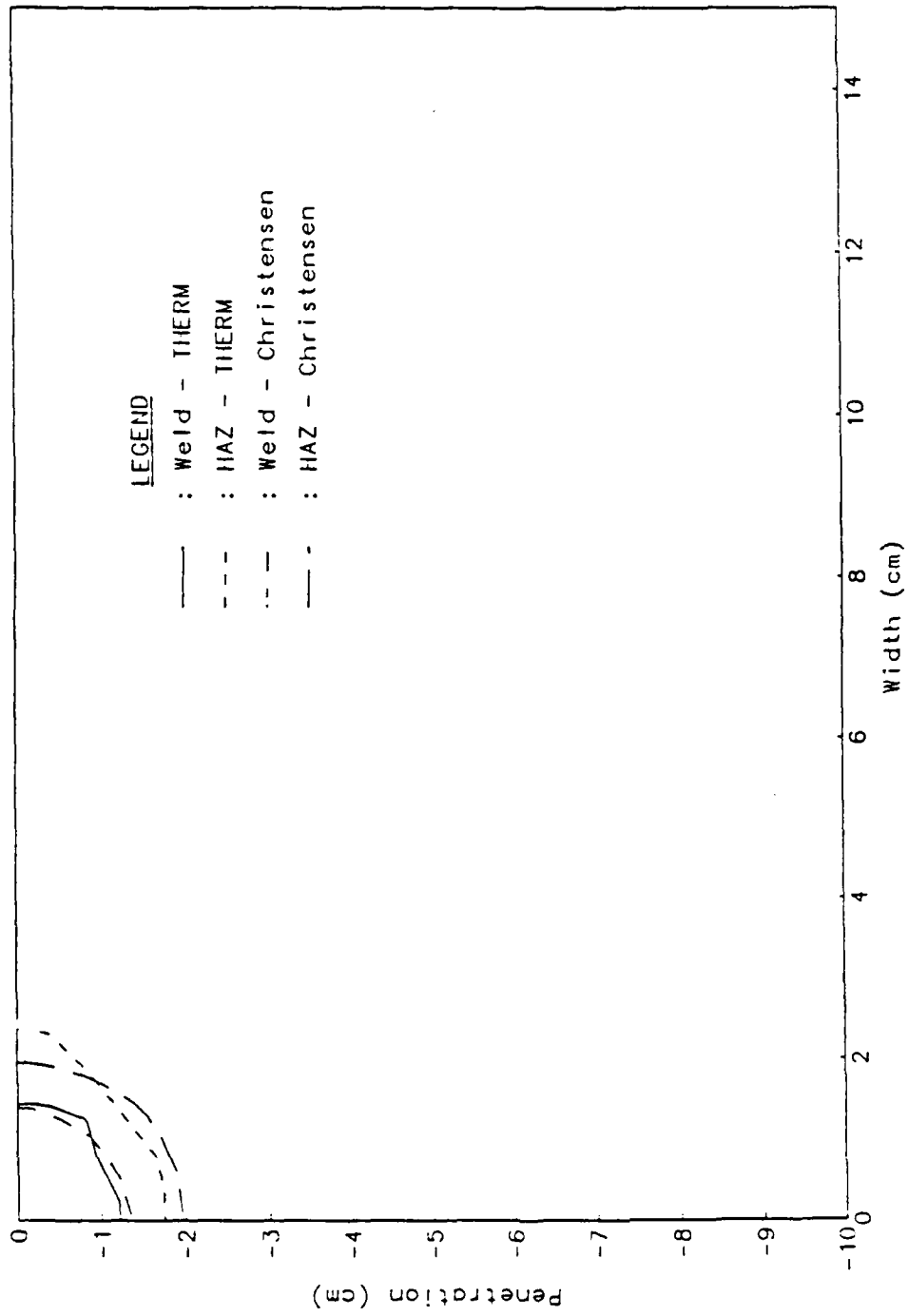
Figure 4.13 Bead shape in submerged arc weld.
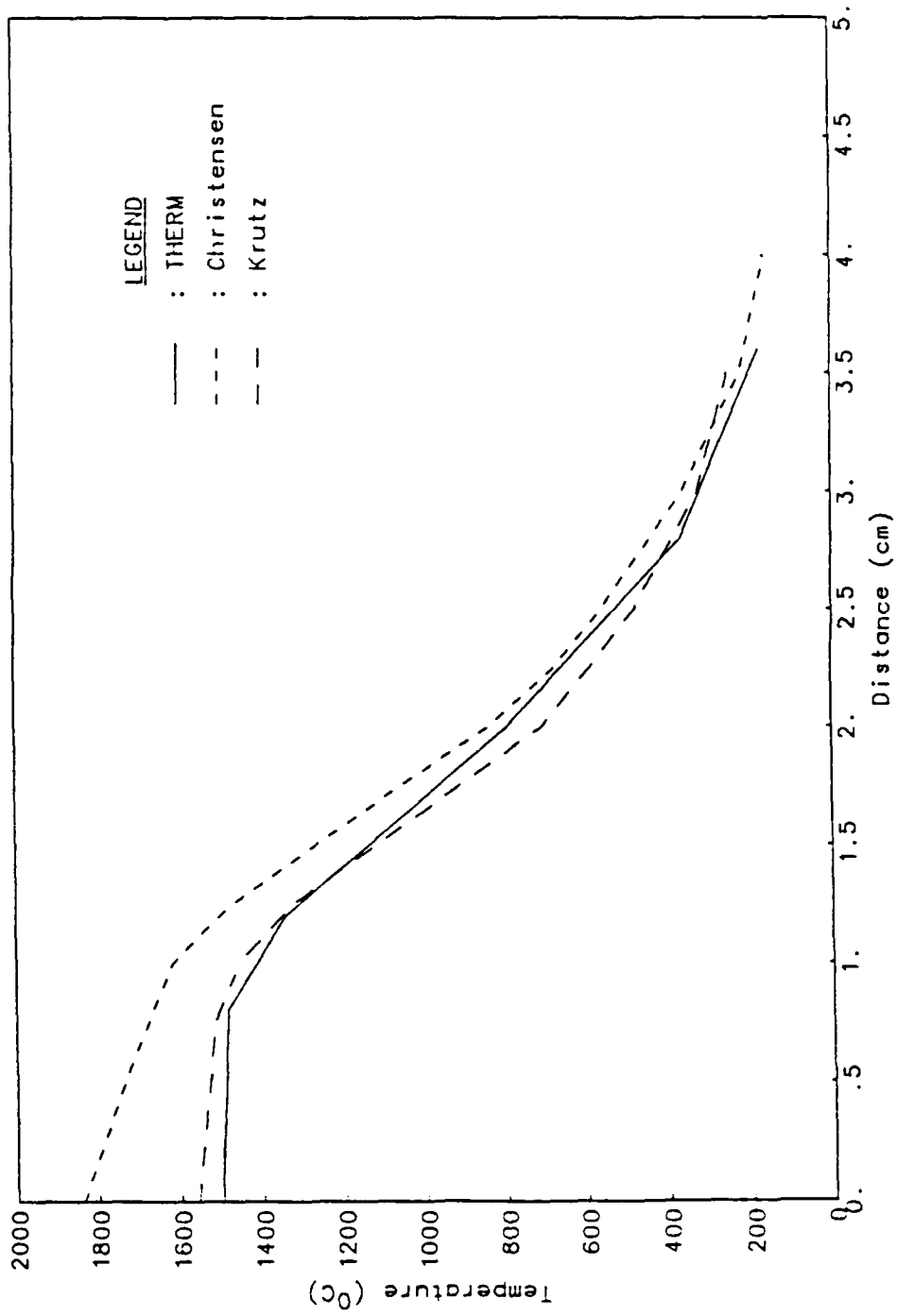
Figure 4.14   Temperature distribution on top surface after 11.5 sec (SAW).
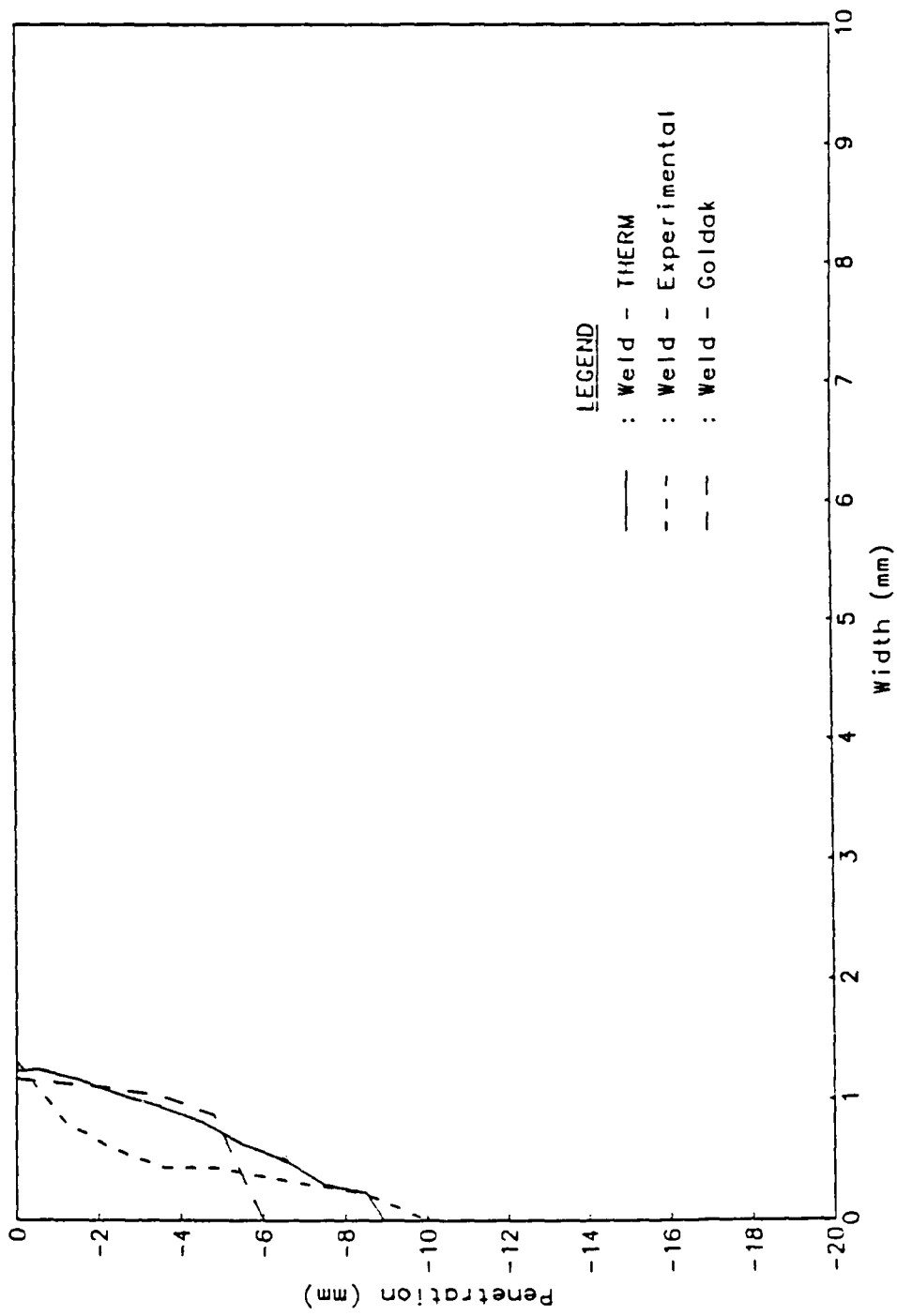
Figure 4.15   Bead shape in electron beam weld.
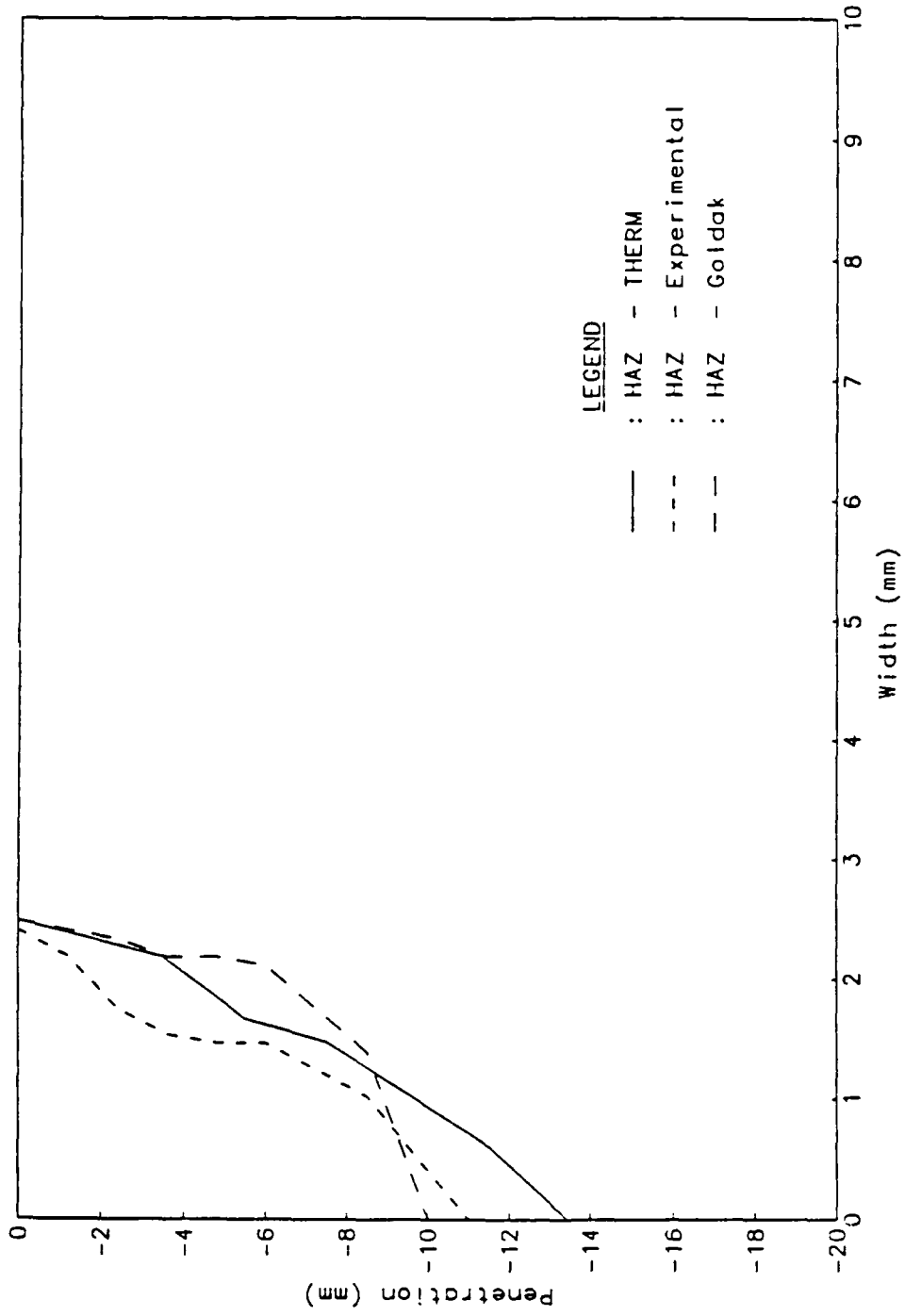
Figure 4.16 HAZ shape in electron beam weld.

to the experimental results with regards to the weld penetration, top bead width as well as the HAZ profiles.

4.5.7 Laser Weld in Stainless Steel

Locke et al.[80] have presented experimental results of high power deep penetration laser welds in type 304L stainless steels over a wide range of power settings. THERM was used to model one of these welds made with 8 kw laser power and 1.27 cm/sec (30 ipm) welding speed on a $\frac{3}{8}$ inch plate. The effective radius of the laser beam was assumed to be equal to the beam spot radius of 0.0508 cm as reported by Locke. A finite element mesh of 136 elements and 170 nodes consisting of four and five node elements was used for modeling the 10.0 cm wide and 1.0 cm thick plate. The material properties used are

Thermal Conductivity	:	0.189 w/cm °K;
Vol. Specific Heat	:	4.000 j/cm^3 °K;
Latent Heat of Fusion	:	1997 j/cm^2;
Emissivity	:	0.9;
Solidus Temperature	:	1673 °K;
Liquidus Temperature	:	1723 °K;
Initial and Ambient Temperature	:	300 °K.

Thermal conductivity in the molten pool was assumed to be four times that in the solid material to approximate the convection in the molten pool. An effective energy absorption factor of 50% was used for this weld. The weld cross-section as predicted by THERM is compared with the experimental result of Locke in figure 4.18. The weld penetration as well as the top bead width predicted in very good agreement with the experimental results. The model does not exactly predict the
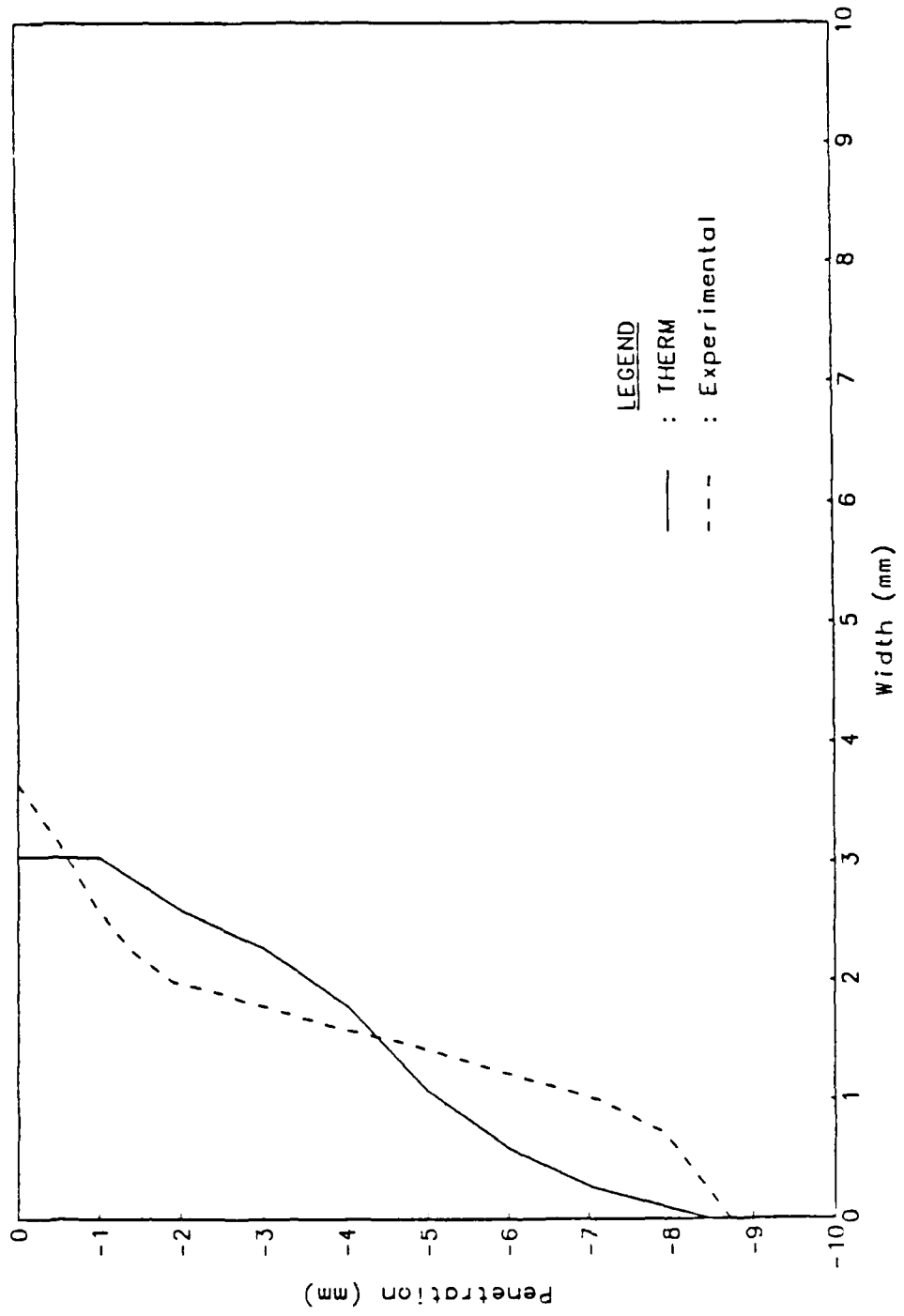
Figure 4.17 Cross-section of laser weld in 304 steel.

nail-head shape of the actual weld, but the cross-section predicted is reasonably close.

4.6 Summary

The finite element weld heat transfer model THERM has been tested for accuracy by solving many problems in heat transfer and solidification as well as by analyzing numerous welding problems. The welding heat transfer problems solved covered a wide range of input power levels as well as power intensities, and varied from thin section full penetration welds to partial penetration welds in thick plates. The results predicted by THERM match well with the published experimental and numerical results. The model has been used for analyzing the laser welds in aluminum alloys and the results are presented in the next chapter.

Chapter 5

RESULTS AND DISCUSSION

High power CO_2 laser welds were made in the four aluminum alloys over a wide range of welding parameters as described in chapter 3. Generally, laser welding of aluminum alloys was found to be very erratic with poor reproducibility. In the 5xxx alloys, violent eruptions frequently occurred during welding, and the weld cycle was accompanied by an intense plasma at the plate surface. In the conduction mode welds in alloy 6061 and the lower power off-focus welds in alloys 2219, 5083 and 5456, the coupling between the laser beam and the material was sometimes lost during welding. Therefore, all the conduction mode and the off-focus welds were made with the plate surface spray painted black to ensure coupling. Defects mainly observed in the laser welds were porosity, shrinkage cavities and undercuts. Solidification cracks were occasionally found in the laser welds in 1.27 cm thick 6061-T6 plates both in the conduction and keyhole modes. This alloy is prone to solidification cracking due to the low melting point intermetallic compounds containing Mg and Si. The problem is usually avoided using a proper filler metal of the type 4083 with high Mg, and this aspect was not investigated.

Laser welds in aluminum alloys were characterised with regards to the weld bead shape and dimensions, the nature and amount of porosity, alloying element loss from the weld fusion zone, and the weld microstructures using the testing procedures described in section 3.3. The melting and solidification phenomena in the laser welded aluminum alloys were also simulated using the two-dimensional finite element heat transfer program THERM described in chapter 4. The results of the experimental characterization and the numerical simulation of the laser welds are discussed in this chapter.

5.1 Weld Bead Shape and Dimensions

The weld bead shape and dimensions described by the weld penetration, weld top bead width, aspect ratio, weld cross-sectional area, and the overall process efficiency are presented in the following sections in terms of the welding parameters for each of the alloys and the laser welding modes investigated.

5.1.1 Weld Penetrations

Weld penetrations obtained in the laser welds in aluminum alloys are shown in figure 5.1. As expected, weld penetration increases with increasing laser power and power intensity, and with decreasing welding speed. However, considerable variation in the weld penetration was observed in the laser welds among the different aluminum alloys. Alloy 2219 had the minimum weld penetration (figure 5.1a), and the 5xxx alloys the maximum (figure 5.1b and 5.1c) for similar welding conditions. For instance, as shown in figure 5.1a and 5.1b for the on-focus laser welds, weld penetration in alloy 2219 was 0.31 to 0.41 cm at 5 kw and 0.74 to 0.88 cm at 10 kw, as compared to alloy 5083 which had 0.83 to 1.03 cm at 5 kw and 1.14 to 1.21 cm at 10 kw. The decrease in the weld penetration with reduction in laser power from 10 kw to 5 kw was rather pronounced for alloy 2219. Further, the weld penetration was not uniform throughout the weld length, the average standard deviation (ASD) being 0.05 cm for alloy 2219 and 0.12 cm for the 5xxx alloys. The variation in penetration along the weld length showed some periodicity in the 5xxx alloys as seen in the longitudinal sections shown in figure 5.10. In addition, on-focus laser welds in alloy 6061 showed considerable scatter in the weld penetration data as seen in figure 5.1d.

The conduction mode welds in alloy 6061 showed a strong dependence of weld penetration on the plate thickness as shown in figure 5.1e. In the 0.4 cm sheets,

85
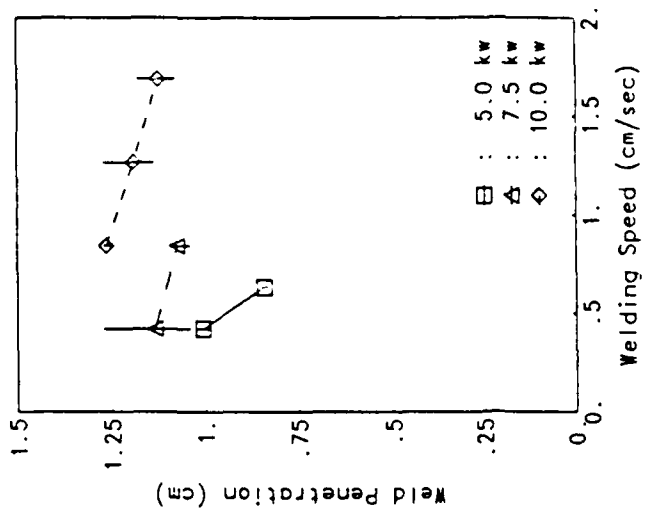
a. Alloy 2219
(on-focus welds)
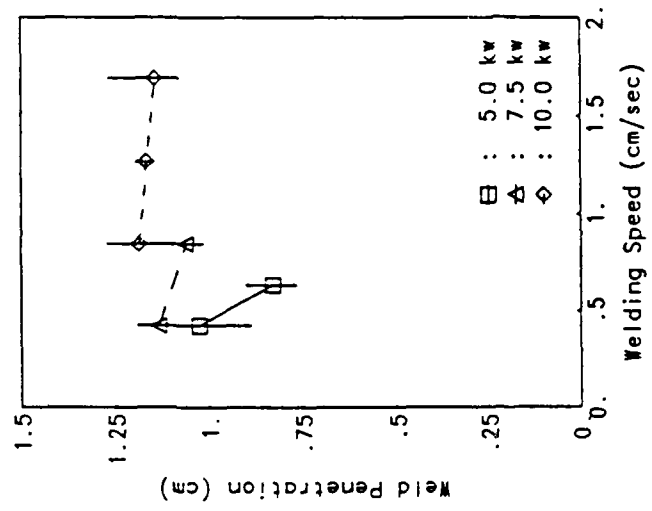
b. Alloy 5083
(on-focus welds)
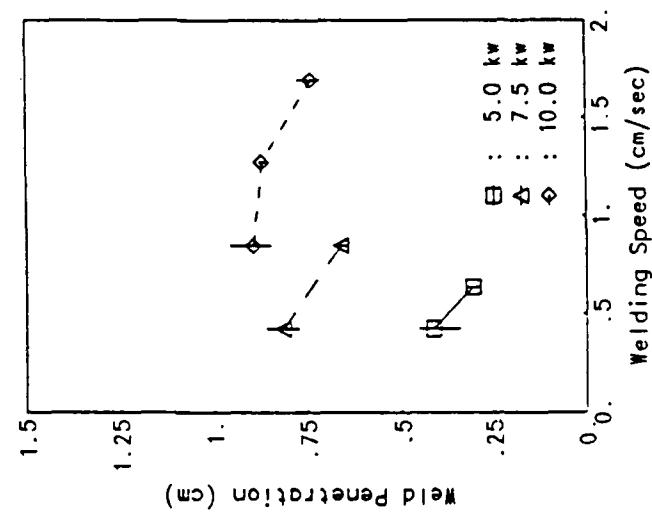
c. Alloy 5456
(on-focus welds)

Figure 5.1 Weld penetration in laser welds in aluminum alloys.
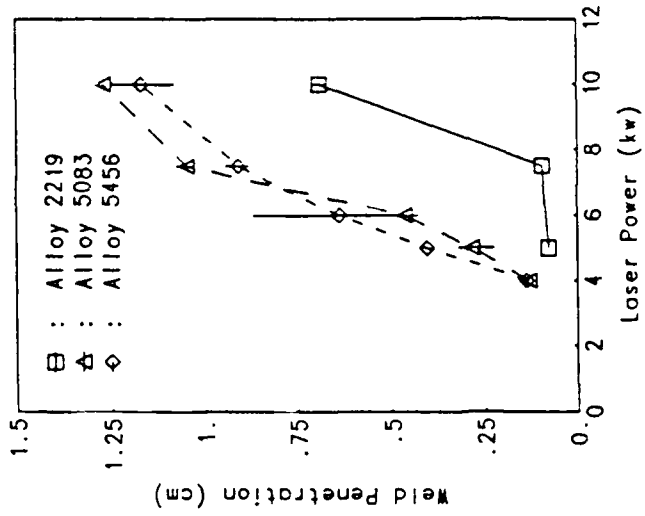
c. Off-focus welds
(speed 0.423 cm/sec)
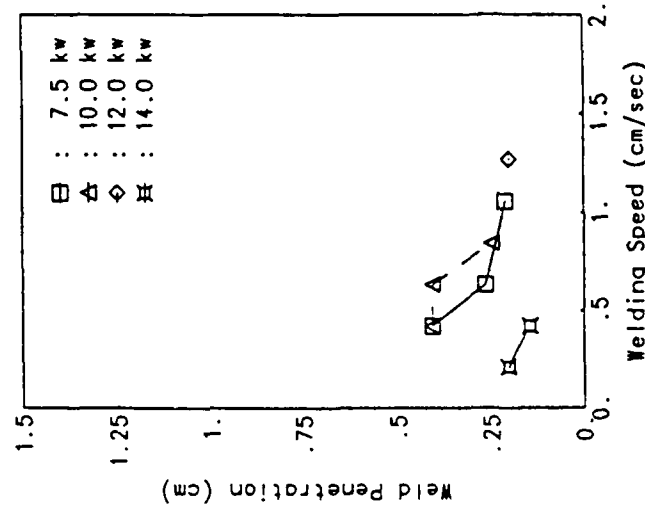
d. Alloy 6061
(on-focus welds)
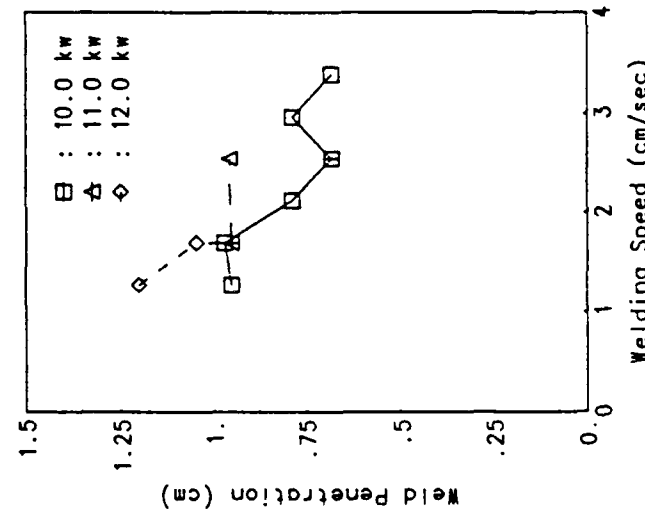
e. Alloy 6061
(conduction welds)

Figure 5.1 (continued).

the weld penetration was in the range of 0.2 to 0.4 cm for power levels of 7.5 to 12.0 kw and welding speeds of 0.423 to 1.27 cm/sec (10 to 30 ipm). The weld penetration levelled off to about 0.2 cm at the higher welding speeds. However, for the conduction mode welds on 1.27 cm plates, the weld penetration obtained was only 0.15 to 0.2 cm even at a higher power level of 14 kw and lower welding speeds of 0.212 to 0.423 cm/sec (5 to 10 ipm).

The off-focus welds in alloys 2219, 5083 and 5456 were made at different power levels using a constant welding speed of 0.423 cm/sec (10 ipm). These welds provided some information regarding the transition from conduction mode to keyhole mode of welding in aluminum alloys. From figure 5.1f, it is seen that the weld penetration in alloy 2219 increased from less than 0.1 cm at 7.5 kw to 0.69 cm at 10 kw, indicating such a transition. For the 5xxx alloys, no keyhole was formed at 4 kw for which the weld penetration was 0.13 cm. At power levels greater than 5 kw, the weld penetration increased to almost full penetration at 10 kw.

5.1.2 Weld Top Bead Widths

The weld top bead widths in laser welds in aluminum alloys are shown in figure 5.2, and the data generally follows the trends observed for weld penetration. The bead widths were found to be in the same range for alloys 2219, 5083 and 5456 at laser power levels of 7.5 and 10.0 kw as seen in figures 5.2a to 5.2c. However, at 5.0 kw, the bead widths in alloy 2219 are considerably smaller. The variations in bead widths along the weld length were of the same order for all alloys (ASD of about 0.07 cm). The on-focus welds in alloy 6061 showed the minimum bead width as seen in figure 5.2d. The scatter in the bead width data was also considerably less than in the penetration data for this alloy.

Figure 5.2 Weld top bead width in laser welds in aluminum alloys.
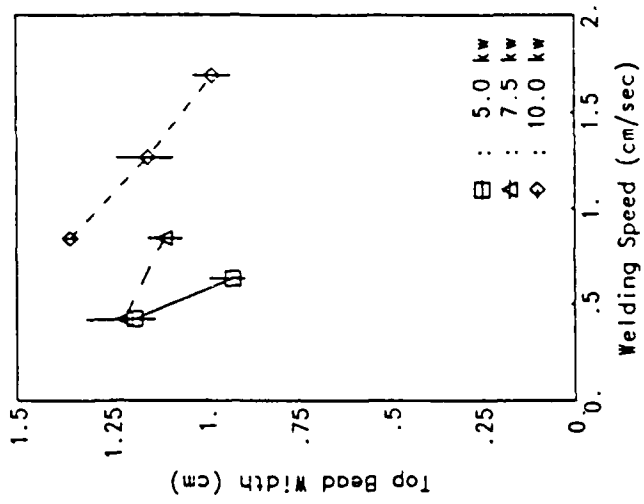
a. Alloy 2219
(on-focus welds)
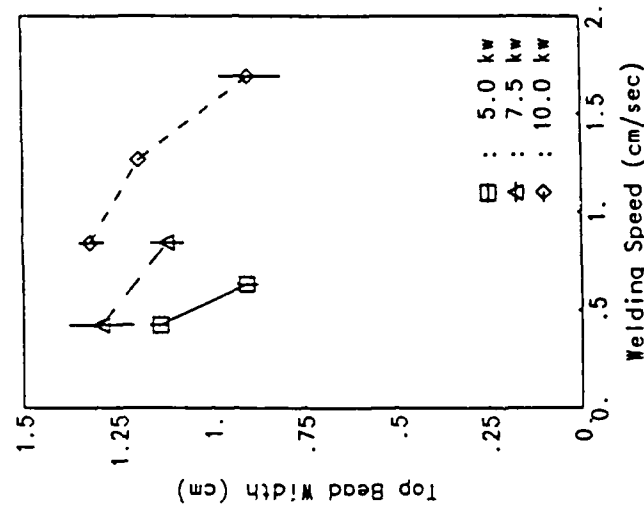
b. Alloy 5083
(on-focus welds)
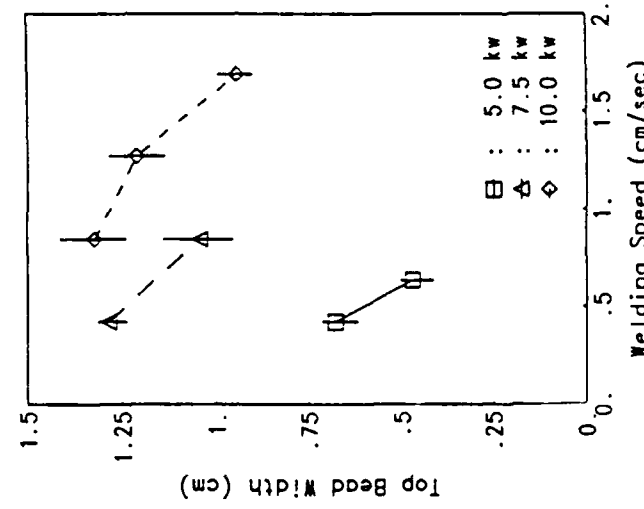
c. Alloy 5455
(on-focus welds)

f. Off-focus welds
(speed 0.423 cm/sec)
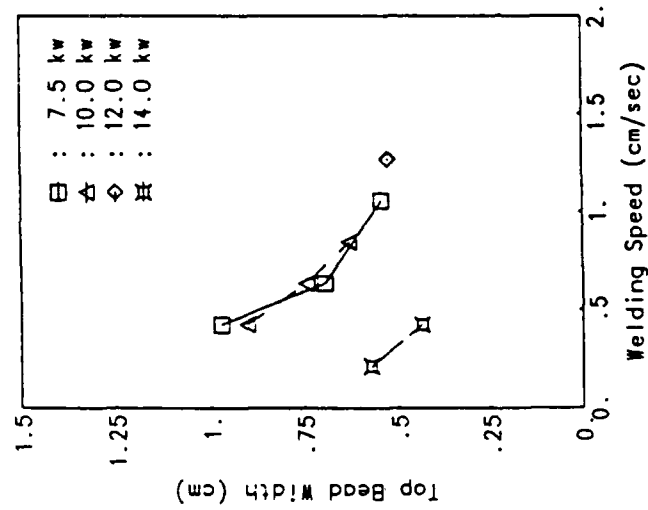
e. Alloy 6061
(conduction welds)
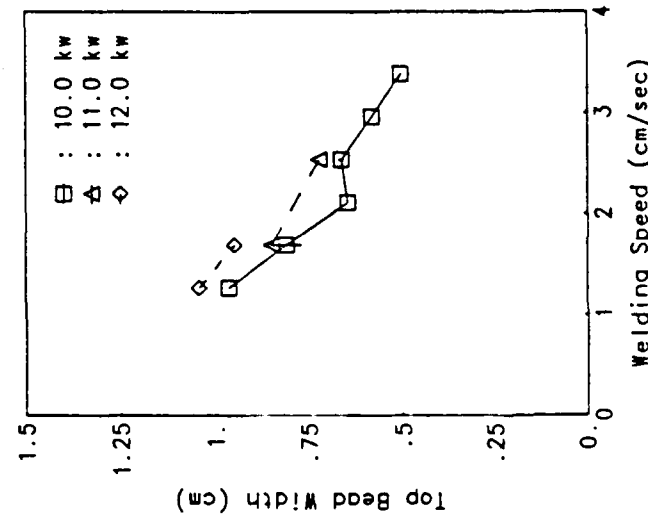
d. Alloy 6061
(on-focus welds)

Figure 5.2 (continued).

The conduction mode welds in alloy 6061 showed decrease in bead width with welding speed, but showed no significant dependence on the laser power. Again, the thickness effect was very significant as seen in figure 5.2e. The bead width data in off-focus welds was also consistent with the earlier observations regarding the transition from conduction mode to keyhole mode as seen in figure 5.2f. Weld top bead widths in the off-focus laser welds ranged from less than 0.16 cm in 5 kw welds in alloy 2219 to over 1.4 cm in 10 kw welds in alloys 5xxx. The very large bead widths in the 10 kw off-focus laser welds result from the low welding speed of 0.423 cm/sec (10 ipm) used.

5.1.3 Aspect Ratios

From the data on weld penetration and top bead widths, the aspect ratios of laser welds (penetration to width ratio) were compared among the alloys and welding modes. Figure 5.3 shows the range of aspect ratios obtained in the four aluminum alloys. Alloy 6061 showed the best ratios ranging from 0.99 to 1.36, whereas alloy 2219 had the lowest ratios in the range 0.61 to 0.78. For alloy 5xxx, the ratio was close to 1.0 and ranged from 0.85 to 1.27. The off-focus keyhole welds had slightly lower ratios than the on-focus keyhole welds. The conduction mode welds in all the four alloys had aspect ratio of about 0.4.

Laser welds in aluminum alloys exhibited much smaller aspect ratios as compared to laser welds in steels which can have aspect ratios in the range of 4 to 5. Aluminum laser welds resemble more the plasma arc welds in steels. Alloy 6061 with the smallest top bead widths for similar welding conditions resulted in the best aspect ratio, whereas alloy 2219 with the smallest weld penetration also had the smallest aspect ratio.
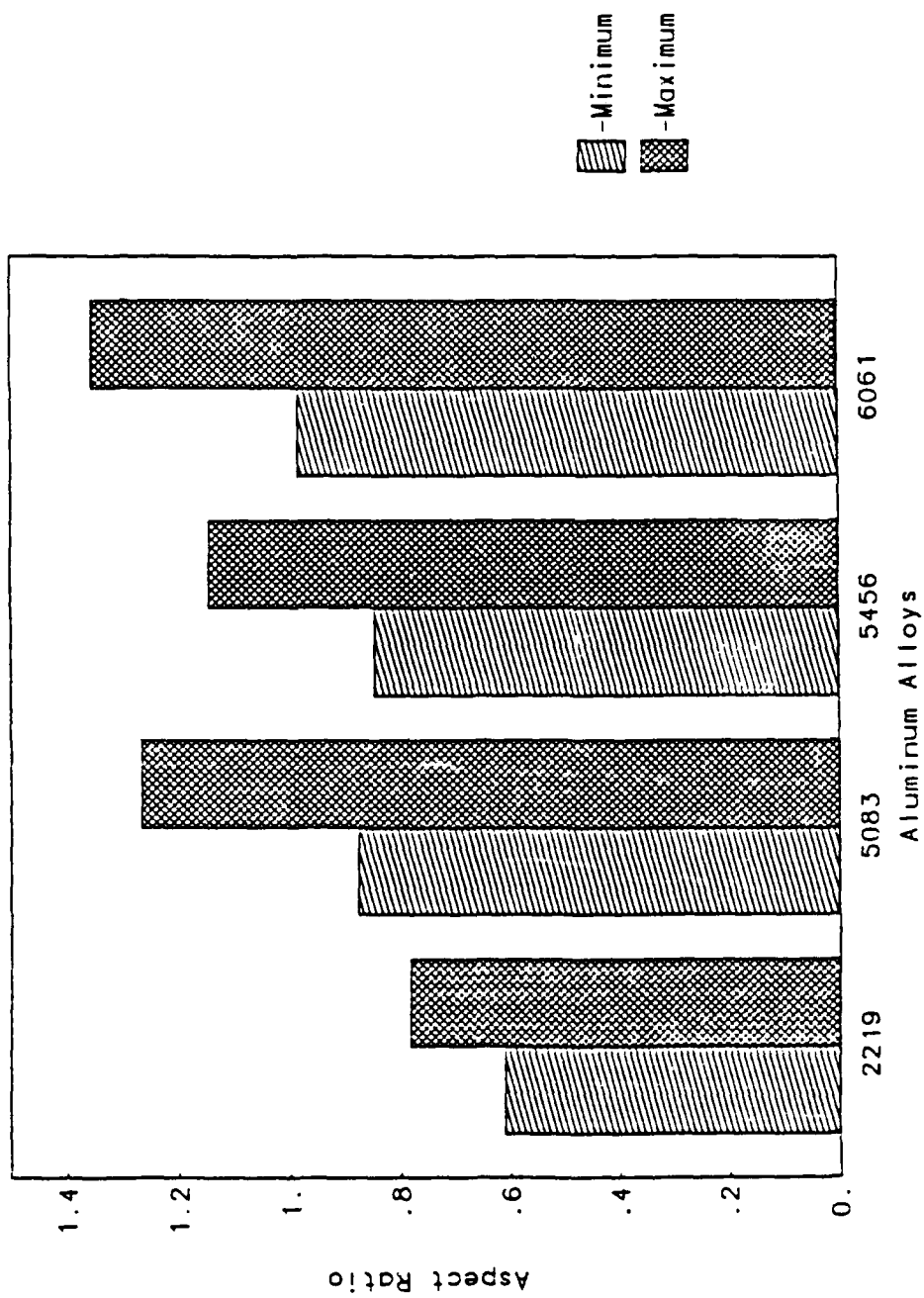
Figure 5.3 Aspect ratios in on-focus laser welds in aluminum alloys.

5.1.4 Weld Cross-sectional Areas

Although weld penetration and bead width data are important in selecting the weld parameters and for design considerations, the influence of welding parameters on the weld cross-sectional area gives more information on the process efficiency and absorption characteristics of the material. Figure 5.4 shows that the data on weld area for the different aluminum alloys and welding modes is consistent with trends observed earlier in the penetration and bead width data. Weld area increases with laser power and decreases with welding speed. Alloys 2219 and 6061 had the minimum weld area, and the 5xxx alloys the maximum for the keyhole welds. For instance, in 7.5 and 10 kw on-focus keyhole welds in alloy 2219, the weld area was about 58.8 to 69.6% of weld areas in alloy 5456; at 5 kw it was even lower (12.6 to 21.8%). Weld areas measured for off-focus welds in alloys 2219 and 5xxx also confirmed the transition from small conduction mode welds to larger keyhole welds as seen in figure 5.4f.

5.1.5 Process Efficiencies

The overall welding process efficiency for the aluminum laser welds was determined by calculating the quantity of heat (h_0) required to heat and melt the volume of weld metal per cm of weld length. The ratio of h_0 to the total laser heat input h_i per cm of weld length $(h_i = \frac{power}{speed})$ is defined here as the process efficiency. Thus, the process efficiency is given by the expression

$$\eta = \frac{v(c\Delta T + H)}{power/speed}$$

where v is the volume of the weld metal per unit length of weld, c the average volumetric specific heat, ΔT the difference between the ambient temperature and the melting point, and H the latent heat.
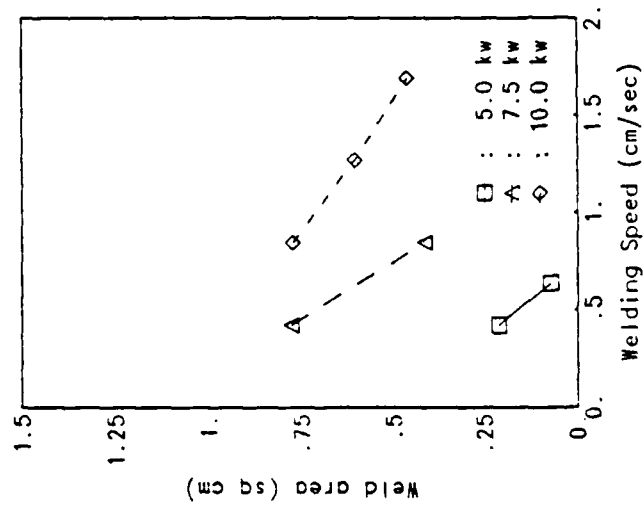
c. Alloy 5456
(on-focus welds)
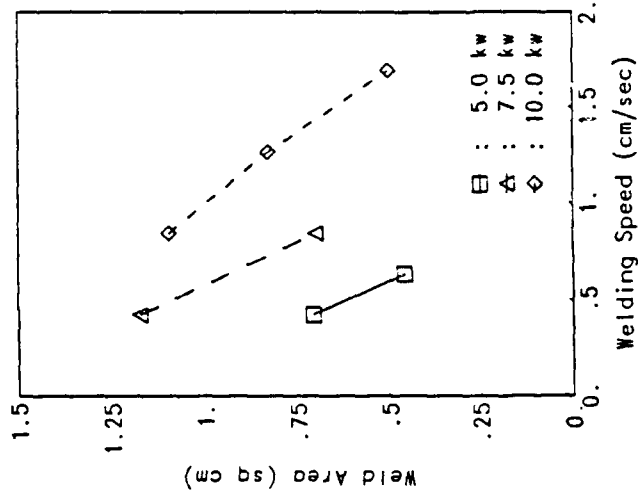
b. Alloy 5083
(on-focus welds)
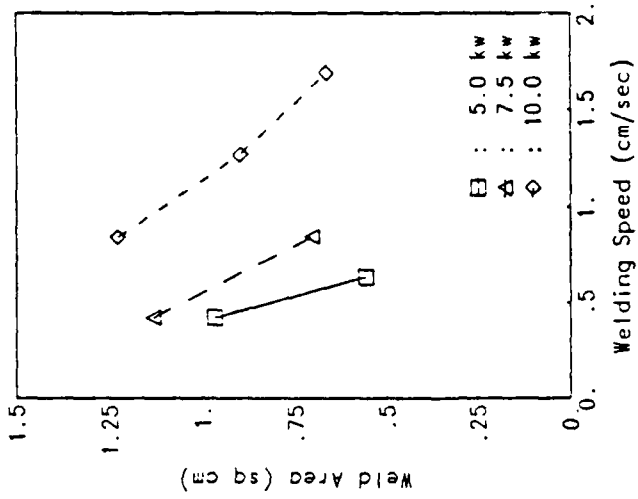
a. Alloy 2219
(on-focus welds)

Figure 5.4   Weld area in laser welds in aluminum alloys.
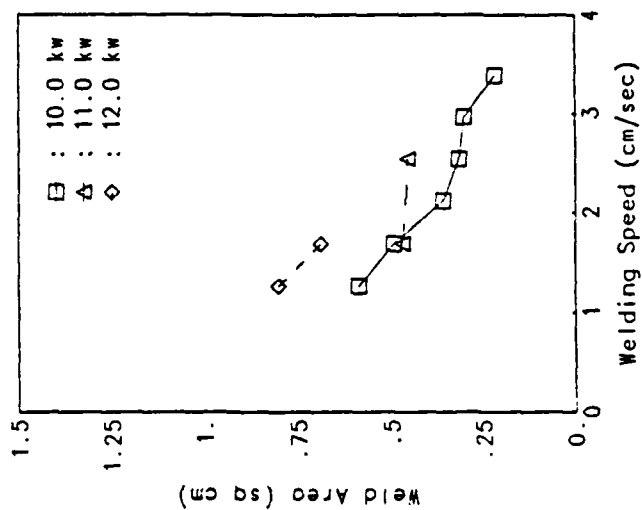
f. Off-focus welds
(speed 0.423 cm/sec)
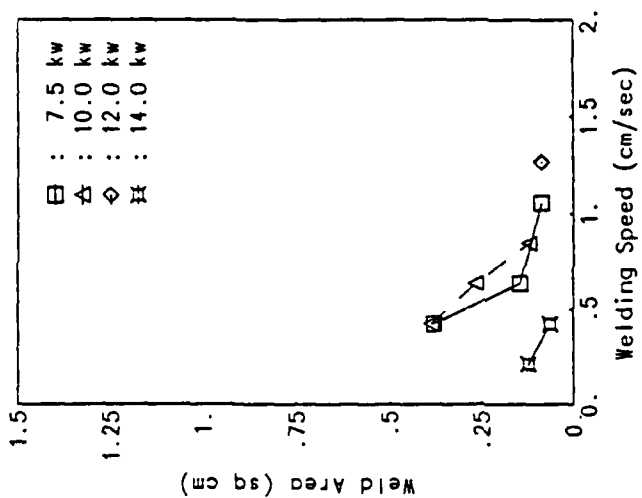
e. Alloy 6061
(conduction welds)

d. Alloy 6061
(on-focus welds)
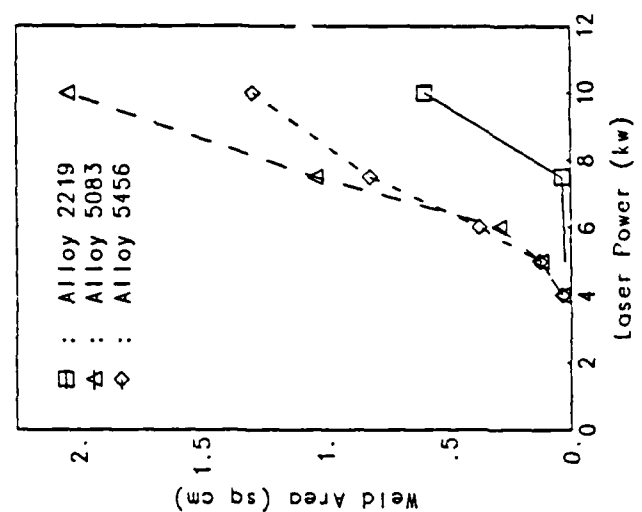
Figure 5.4 (continued).

94

Figure 5.5 shows the plots of process efficiency in laser welds in aluminum alloys. In on-focus laser welds, process efficiency increased with laser power, but showed no consistent trend with respect to the welding speed. Keyhole laser welds in alloy 5456 showed the highest process efficiency of 30 – 33% at 10 kw, and between 18 and 24% at the lower power levels. Alloy 5083 showed slightly lower process efficiencies, but with similar trends as alloy 5456. For alloy 2219, process efficiency decreased drastically from 20 – 23% at 10 kw to only about 2 – 5% at 5 kw indicating that the 5 kw welds were conduction mode welds. In on-focus welds in alloy 6061, the process efficiency ranged from 17 – 25% at all power levels investigated, whereas in the conduction mode welds in the same alloy, the process efficiency was always less than 5%, and generally decreased with welding speed. Off-focus welds showed a wide range of process efficiencies from as low as 0.6% in conduction mode welds in alloy 2219 to over 20% in keyhole welds in alloy 5083.

The process efficiency plots in figure 5.5 show some inconsistencies. For instance, η decreases with welding speed at 5 kw, but at 7.5 kw, η increases with welding speed. At 10 kw, a maximum η is observed at 1.27 cm/sec (30 ipm). The calculation of η involves the volume of weld metal v per unit length of weld, which is dependent on the welding speed and the laser power as discussed in section 5.1.4. However, the role of the welding parameters on the weld volume is rather complex. At low welding speeds, a larger amount of heat loss occurs due to conduction with resulting low η. Similarly, at high welding speeds, the η is lower as there is insufficient time for the material to react. The weld metal volume v is expected to be the maximum at the optimum welding speed which is a function of the laser power. This manifests as the apparently inconsistent behavior observed
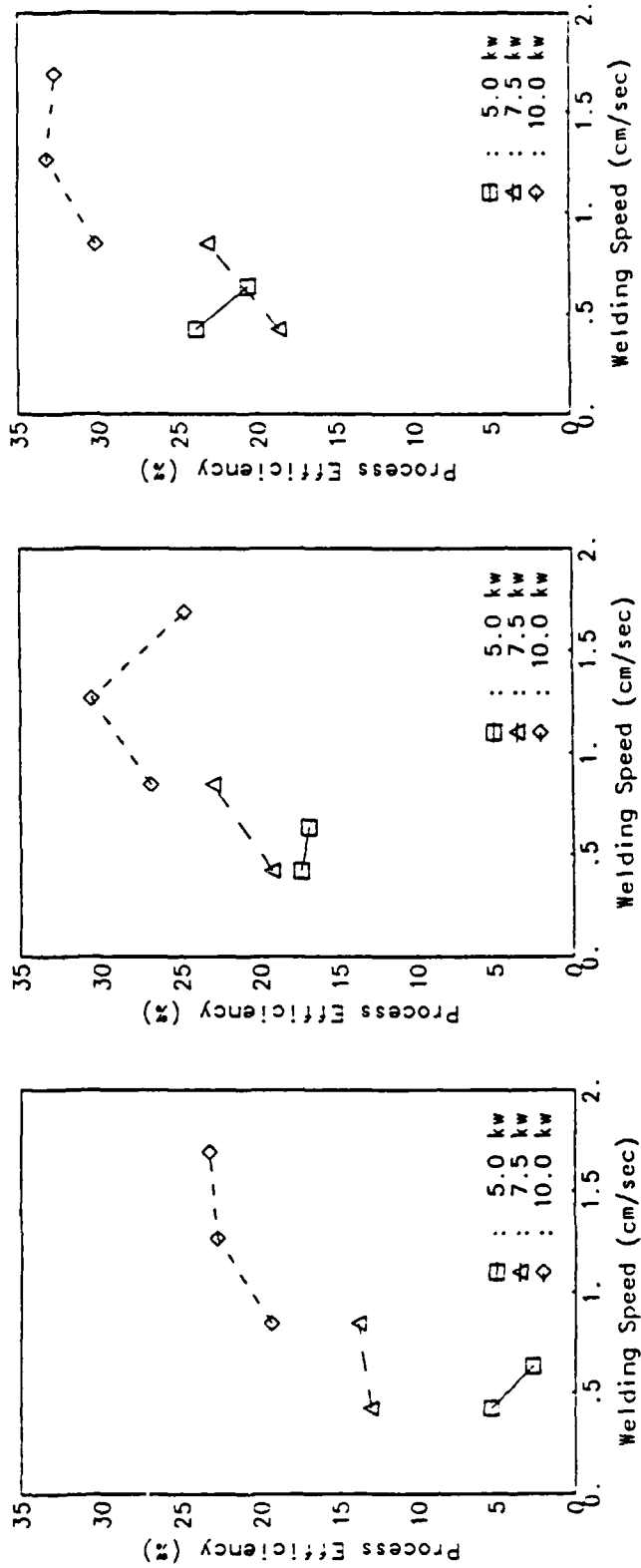
a. Alloy 2219
(on-focus welds)

b. Alloy 5083
(on-focus welds)

c. Alloy 5456
(on-focus welds)

Figure 5.5 Process efficiency in laser welds in aluminum alloys.
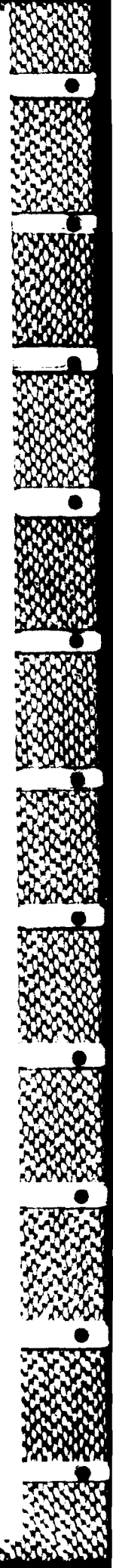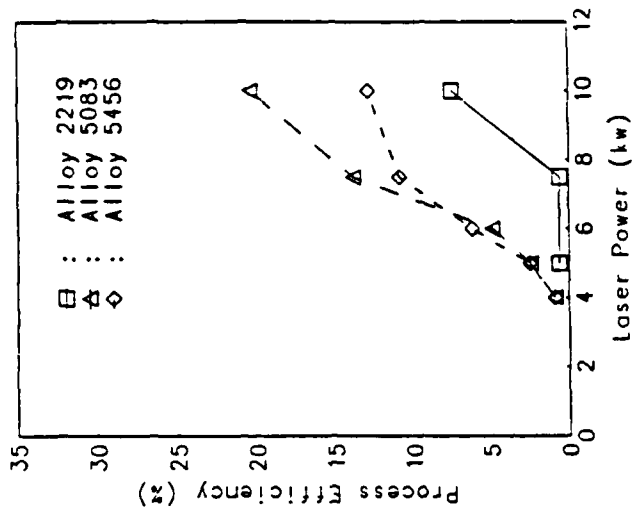
d. Alloy 6061
(on-focus welds)
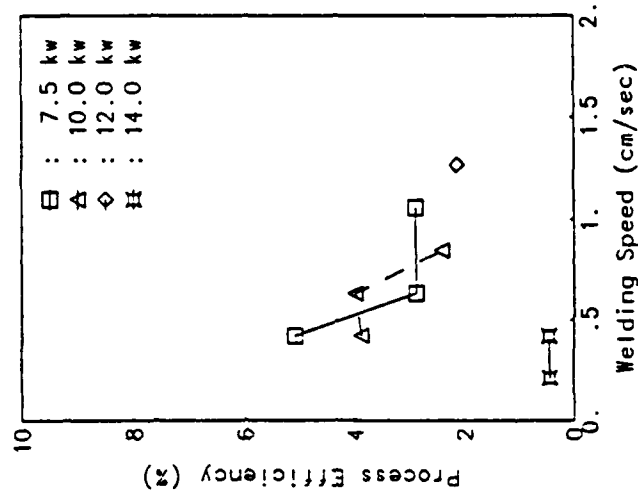
e. Alloy 6061
(conduction welds)
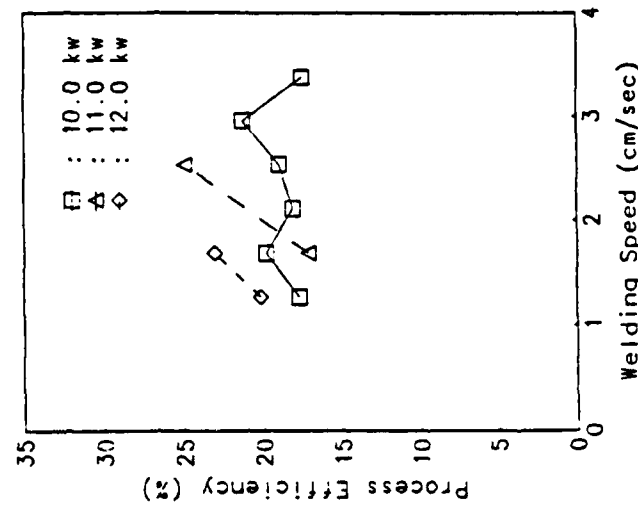
f. Off-focus welds
(speed 0.423 cm/sec)

Figure 5.5 (continued).

in figure 5.5. A schematic of the expected behavior of process efficiency is shown in figure 5.6.

5.1.6 Summary

Aluminum alloy 2219 showed considerably lower weld penetration than the 5xxx series alloys or the alloy 6061. As mentioned in section 2.1.3, the balance of forces at the bottom of the keyhole given by equation 2.2 relates the vapor pressure P_v with the cavity depth h. Due to the presence of volatile elements like magnesium, alloys 5xxx are expected to result in higher vapor pressure at the bottom of the cavity than in alloy 2219 for similar welding condition (see figures 3.1 to 3.3). Thus deeper cavities are expected with consequently higher weld penetrations in the magnesium containing aluminum alloys.

Generally, the laser welds in aluminum alloys exhibited much larger bead widths than observed in steels or titanium. The higher thermal diffusivity of these alloys is a key factor in causing such large bead widths. Further, the energy required to melt a unit volume of weld metal in aluminum is about 30% of that required for steels. The laser welds generally depicted a nail head shape with large bead width at the top surface which reduced rapidly to less than half the top width at depths slightly below the plate surface (see figure 5.9). One of the causes of such a weld shape is believed to be the reradiation of energy from the plasma generated at the plate surface. In addition, the laser optics also influences the weld profile obtained. The focal lengths resulting from electromagnetic focusing in EB welding are much longer than in laser welding. The shorter focal lengths involved in laser systems in turn result in larger beam divergence angle, and the power intensity decreases rapidly away from the focal spot.

Process Efficiency

Welding Speed

$P_3 > P_2 > P_1$

P_3

P_2

P_1
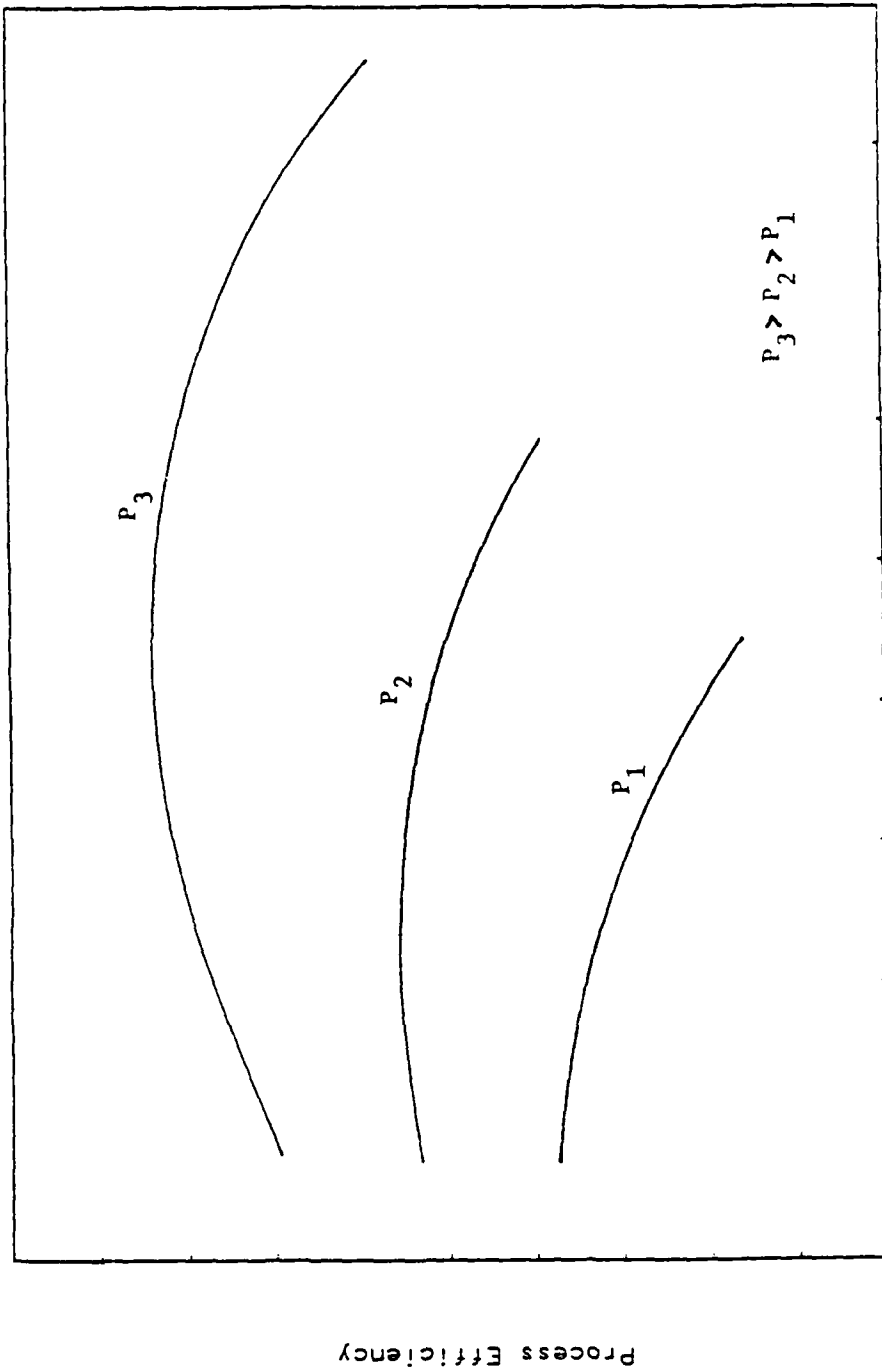
Figure 5.6 Expected process efficiencies at varying power levels P_i.

Weld bead dimensions described in the last few sections showed that the laser welds in aluminum alloys ranged from conduction mode to keyhole welds. The overall welding process efficiency data was used to classify the welding mode for each of the welds. The on-focus welds in alloy 5xxx and 6061 had process efficiency better than 17%. However, alloy 2219 exhibited a process efficiency of only 5% or less for the 5 kw on-focus welds as compared to over 13% efficiency at 7.5 kw and over. Absorptivity of these aluminum alloys is in the range of 5%, and it improves considerably once the keyhole is formed. The weld bead dimensions as well as process efficiency data in off-focus welds in alloys 2219 and 5xxx also showed a transition from conduction mode to keyhole mode. Thus, a process efficiency value of about 5% was defined as a threshold below which the welds were classified as conduction mode welds and above which the welds were classified as keyhole welds. Using such a criteria, the threshold power intensity for keyholing for alloy 2219 was estimated to be 6.63×10^5 to 8.84×10^5 w/cm^2. Similarly, the threshold intensity for alloys 5xxx is in the range of 5.3×10^5 to 6.63×10^5 w/cm2. In conduction mode welds in alloy 6061, no keyhole was formed even at 14 kw, and therefore, the threshold intensity is greater than 2.33×10^5 w/cm^2.

5.2 Characterization of Surface Hydrogen

The main cause of porosity in arc welds in aluminum alloys is hydrogen as described in section 2.1.2. To reduce the possibility of hydrogen contamination of the laser weld pool, the plate surfaces were thoroughly cleaned prior to welding using a surface preparation procedure recommended by AWS and described in section 3.1. The plate surfaces were then characterised using the depth profile technique by SIMS to ascertain the effectiveness of the surface preparation. An 8 kv, 50 mA beam was used for sputtering the surface at a vacuum of 10^{-8} torr. A typical depth profile for aluminum alloy 5083 for both the as-received and

cleaned surfaces is shown in figure 5.7. The x-axis represents the sputtering time in minutes, and the y-axis represents the detected intensity in counts per second (c/sec) of the different specie being investigated. To determine the actual hydrogen content present, standard specimen of each alloy with known levels of hydrogen are required. Further, the depth of sputtering may not be uniform among the alloys as the sputtering rate varies with the alloying content. As standard specimen were not available for the four aluminum alloys, the relative intensity of hydrogen with respect to aluminum was compared for the two surface conditions for each alloy to study the influence of the surface preparation.

The intensity of hydrogen (+) has a maximum (peak) value at the outermost surface, and it drops to a lower (base) value within a few angstroms in the material as shown in figure 5.7. The peak and the base values of the relative hydrogen intensities are compared for the as-received and cleaned surfaces for each of the alloys in figure 5.8. The surface preparation procedure has significantly reduced the hydrogen intensity at the outer surface. Further, although the peak and base values of hydrogen intensities vary considerably among the four alloys in the as received condition, the base levels are quite uniform among these alloys in the cleaned condition, thereby allowing the volume of porosity to be compared for the different welding conditions.

5.3 Porosity in Aluminum Laser Welds

Figure 5.9 shows transverse sections of typical laser welds obtained in the aluminum alloys showing the kind of porosity observed. In the keyhole welds in the copper containing alloy 2219 as well as the Mg-Si containing alloy 6061, occasional shrinkage cavities were observed which were sometimes as large as 0.3 to 0.4 cm in diameter and usually located near the middle of the weld. Otherwise,
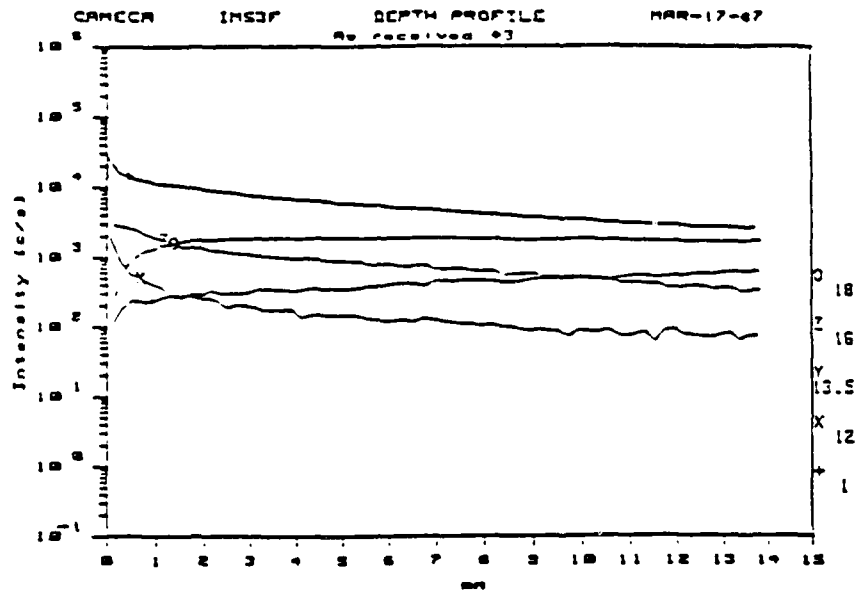
a. As-received plate.
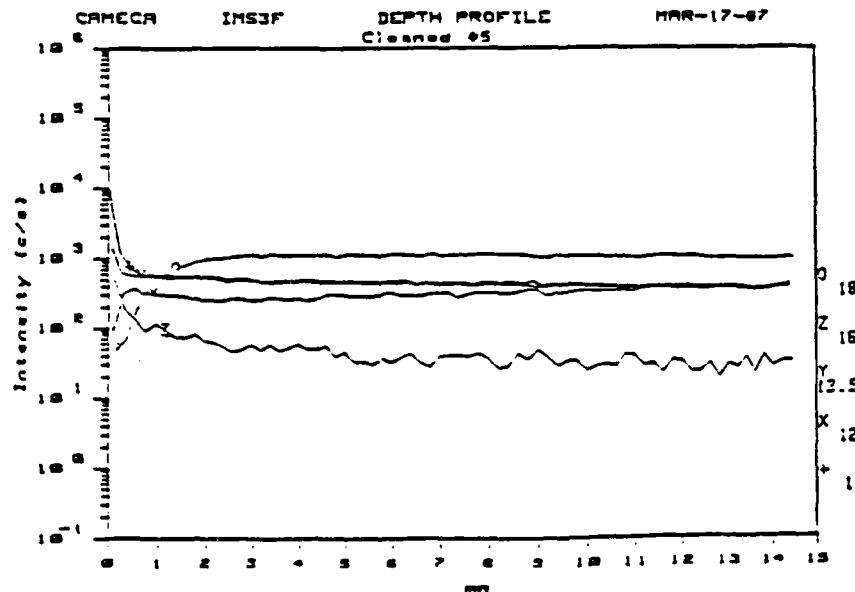
b. Plate surface cleaned as per sec. 3.1.

Figure 5.7   Hydrogen intensity (+) on the surface of alloy
5083 from depth profile using SIMS.
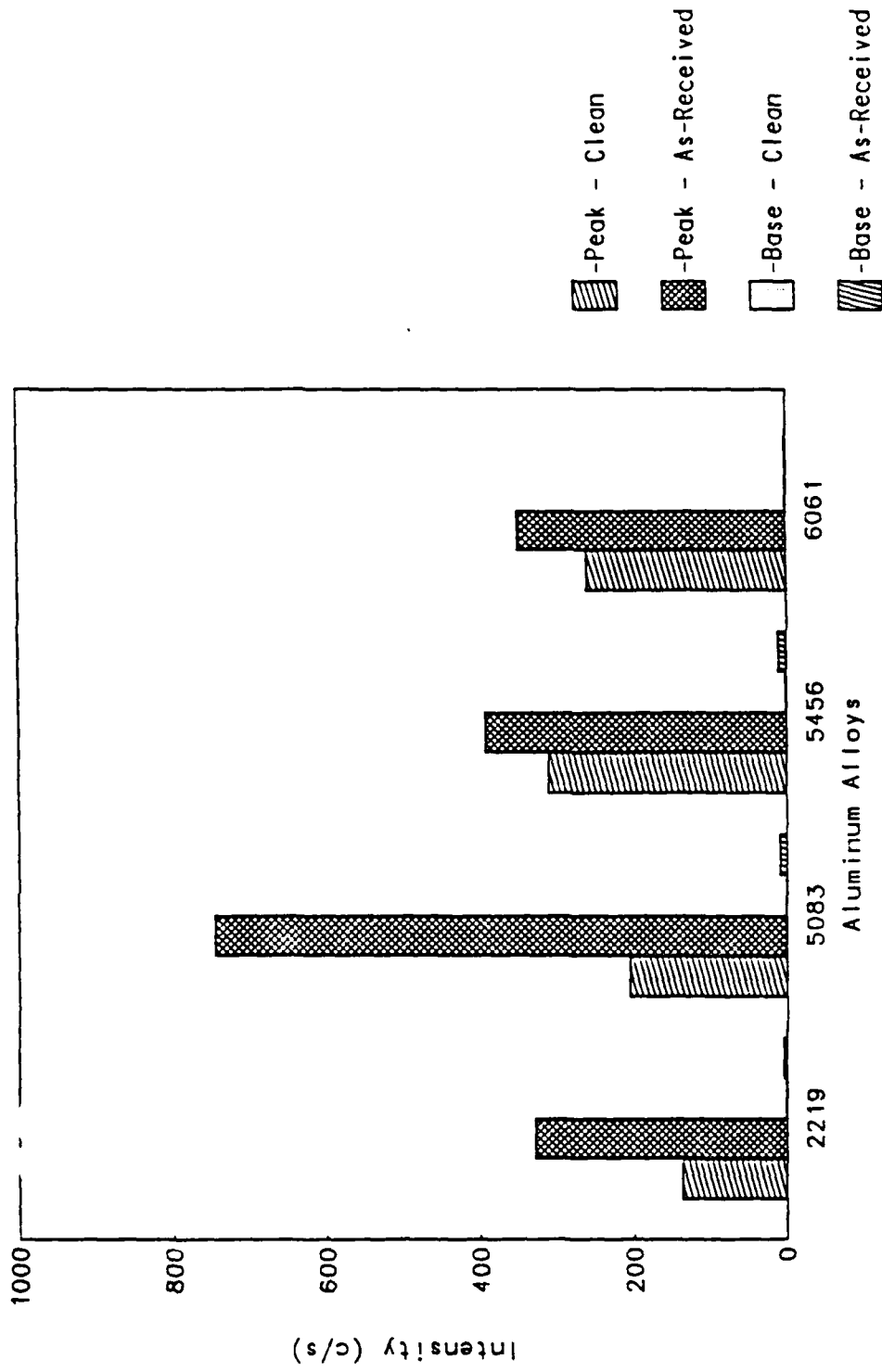
Figure 5.8 Relative intensity of H_2/Al on the surface of aluminum alloys.

a. Alloy 6061
   10 kw
   1.27 cm/sec
   (30 ipm)
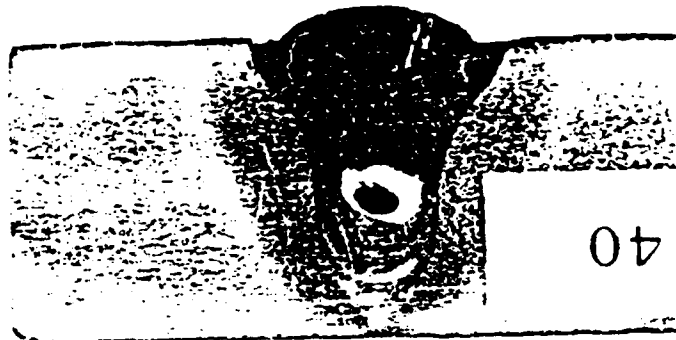
b. Alloy 5456
   10 kw
   0.843 cm/sec
   (20 ipm)

c. Alloy 5083
   10 kw
   0.843 cm/sec
   (20 ipm)

d. Alloy 2219
   10 kw
   0.843 cm/sec
   (20 ipm)

Figure 5.9 Transverse sections of on-focus laser welds
showing porosity and cavities.

these alloys did not exhibit any significant porosity under microscopic examination of transverse sections even at high magnifications. However, the keyhole welds in Mg containing alloys 5xxx contained large amounts of spherical porosity with pore diameters ranging from 0.01 cm to over 0.3 cm. The larger spherical pores were usually clustered near the top surface of the weld bead, and the smaller pores distributed throughout the weld. In addition, these welds also contained frequent large cavities trapped in the middle of the weld. The off-focus keyhole welds in alloys 2219, 5083 and 5456 also showed similar results to on-focus keyhole welds. However, the off-focus conduction welds in alloy 2219 as well as the conduction mode welds in alloy 6061 were generally free of any kind of porosity or shrinkage cavities. The 5xxx series alloys exhibited distributed small pores of about 0.01 cm diameter even in the off-focus conduction mode welds.

Longitudinal sections of the welds shown in figure 5.10 reveal the worm-hole nature of the porosity, as well as the severity of porosity in the 5xxx series alloys. Only primary porosity was observed in aluminum laser welds. No secondary interdendritic porosity was observed during microstructural examination in any of the alloys. The volume of porosity determined from the density measurements is presented in figure 5.11. Porosity measurements by such techniques are usually accurate to within 0.5%. Alloy 2219 contained the minimum amount of voids present, whereas alloys 5xxx had the maximum. Following paragraphs briefly describe the observations regarding the porosity data for the different alloys.

5.3.1 Alloy 2219

As mentioned above, this alloy showed the least amount of porosity, in the range of 0.019 to 0.067 cc per linear inch of weld. Figure 5.11a shows that at laser power levels of 5.0 and 7.5 kw, porosity increased with welding speed, and at

a. Alloy 2219
   10 kw
   1.27 cm/sec
   (30 ipm)

b. Alloy 5083
   10 kw
   1.27 cm/sec
   (30 ipm)

c. Alloy 5456
   10 kw
   1.27 cm/sec
   (30 ipm)

Figure 5.10   Longitudinal sections of on-focus laser welds
showing cavities and uneven penetration.
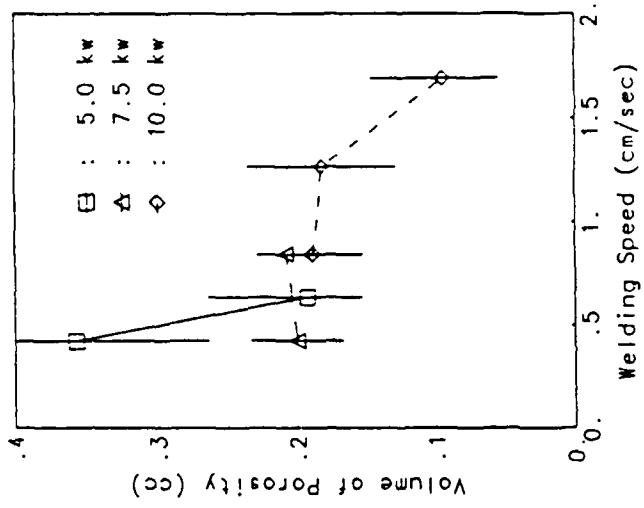
a. Alloy 2219
(on-focus welds)
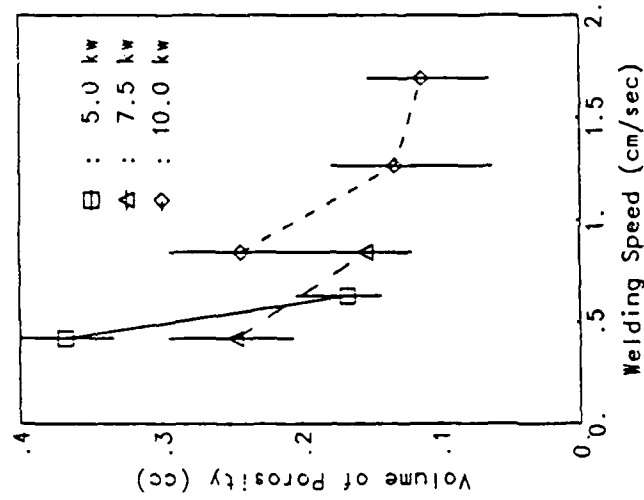
b. Alloy 5083
(on-focus welds)
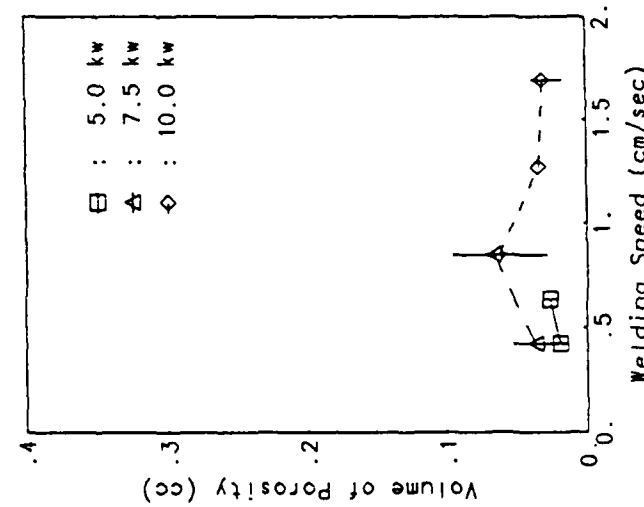
c. Alloy 5456
(on-focus welds)

Figure 5.11 Volume of porosity in laser welds in aluminum alloys.
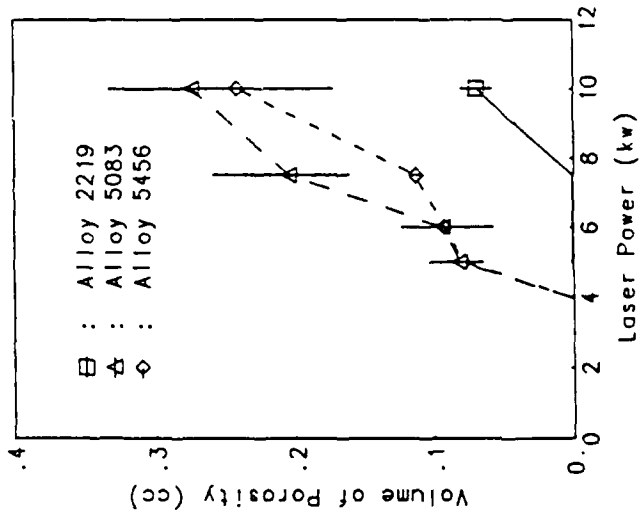
e. Off-focus welds
(speed 0.423 cm/sec)
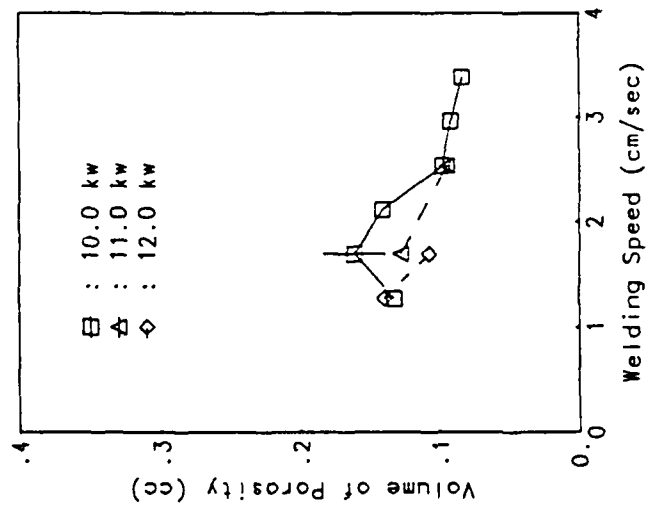
d. Alloy 6061
(on-focus welds)

Figure 5.11 (continued).

10.0 kw the trend was opposite. Moreover, porosity at 5.0 kw was the minimum, whereas at the higher power levels investigated, porosity was about equal. The variation in porosity along the weld length was very small, the average standard deviation (ASD) being 0.0091 cc.

5.3.2 Alloys 5xxx

Alloys 5083 and 5456 had higher levels of porosity in the range of 0.09 – 0.36 cc as seen in figures 5.11b and 5.11c. Porosity decreased with increasing welding speed at all power levels unlike in alloy 2219. Also, maximum porosity was found at the lowest power level of 5.0 kw. The variation along the weld length was also found to be relatively higher (ASD of 0.037 cc).

5.3.3 Alloy 6061

Porosity was observed only in the keyhole welds, and was in the range of 0.08 to 0.16 cc (see figure 5.11d – note that the welding conditions are slightly different from the earlier welds). In general, porosity decreased with increasing welding speeds. However, the data showed large scatter.

5.3.4 Off-focus Welds

In the off-focus keyhole welds made at a welding speed of 0.423 cm/sec (10 ipm), porosity increased with increasing power for all the alloys as seen in figure 5.11e. Only in the 5xxx non-keyhole welds, a small amount of micro-porosity was observed in the low power conduction mode welds.

5.3.5 Summary

Conduction mode welds in alloy 6061 as well as the low power off-focus welds in the other three alloys were generally free from porosity and large cavities. The

surface preparation regimen used to prevent hydrogen contamination of the weld pool was found to be effective by the depth profile techniques using SIMS. It is reasonable, therefore, to assume that the porosity and voids observed in aluminum laser welds are not caused by hydrogen. Porosity and cavities were observed only in the keyhole mode welds at higher laser intensities. These keyhole welds are dominated by the vaporization of elements from the weld pool and the formation of vapor column.

In 5xxx series alloys, the weld penetrations were found to have cyclic variations with a frequency of about 4 to 8 hz as seen in figures 5.10b and 5.10c. This variation of over $\pm 15\%$ in weld penetration is attributed to the instability of the keyhole in these alloys. For a partial penetration weld, the condition for stability at the bottom of the keyhole is given by the expression

$$P_v = \frac{2\sigma}{r} + \rho \, g \, h,$$

and at a depth of x from the plate surface by the expression[2]

$$P_v = \frac{\sigma}{r} + \rho \, g \, x.$$

Assuming that the vapor pressure increases linearly from 0 at the plate surface to P_v at the bottom of the cavity, the condition for a stable keyhole is given by a maximum depth of cavity

$$h_{max} < \frac{r \, x \, P_v(h)}{(\sigma + \rho \, r \, g \, x)}$$

If the cavity depth is larger than h_{max}, the cavity collapses with th liquid metal closing the cavity at the depth x. The laser beam then impinges the liquid metal and the cycle of keyhole formation and collapse repeats at the characteristic frequency.

Such an oscillating and unstable keyhole is believed to result in parts of the cavity getting trapped in the solidifying metal, resulting in the large amount of cavities present in the laser welds in alloys 5xxx. In the alloy 2219, there is no evidence of an unstable keyhole, and the weld penetration does not vary significantly over the length of the weld as seen in figure 5.10a. This alloy consequently contained much smaller amounts of voids present in the form of shrinkage cavities.

5.4 Vaporization of Alloying Elements

The vaporization of alloying elements in the weld metal due to laser welding was investigated for a few selected welds using the electron micro-probe analyzer (EMPA). To compare the gross change in composition in the weld metal due to welding, numerous random spot measurements were made in the base metal as well as the weld metal. Due to the microstructural heterogeneity in the aluminum alloys, use of small beam spot of one micron diameter usually gave erroneous results. Thus, the random spot measurements were made using a larger beam spot of 20 microns. At least ten measurements were taken for each weld to ensure accuracy. The error involved in the EMPA measurements is usually of the order of 2% of the measured value. Laser welding of aluminum alloys caused significant changes in the weld metal compositions, and the results of the alloying element loss are presented in the following paragraphs.

5.4.1 Alloy 2219

The most significant change in the composition (weight percentage) in the weld zone in alloy 2219 was in the two major species aluminum and copper. Table 5.1 shows the chemical composition of the base metal and the on-focus laser welds.

It is seen that weld metal is significantly enriched in copper and is depleted in aluminum as compared to the base metal.

Table 5.1. Weld metal Composition in alloy 2219.

Weld	Al	Cu	Fe	Mn	Si	Ti
Base metal	93.04	5.75	0.10	0.35	0.08	0.05
10 kw, 20 ipm (# 104)	91.55	6.84	0.15	0.33	0.07	0.04
10 kw, 30 ipm (# 102)	92.00	6.82	0.06	0.33	0.097	0.04
10 kw, 40 ipm (# 103)	92.00	6.89	0.15	0.32	0.09	0.05
7.5 kw, 10 ipm (# 106)	92.11	6.70	0.09	0.30	0.08	0.08
7.5 kw, 20 ipm (# 105)	92.53	6.78	0.18	0.31	0.10	0.04
5 kw, 10 ipm (# 108)	91.30	6.86	0.09	0.32	0.08	0.07
5 kw, 15 ipm (# 107)	92.07	6.70	0.08	0.30	0.07	0.07

Depletion of aluminum from the weld metal in alloy 2219 is expected. Vapor pressure of aluminum is almost two orders of magnitude higher than copper in the melting point to boiling point range of aluminum and beyond as shown in figure 3.1a. Also, from figure 3.1c, for the range of input power intensities involved, aluminum boiling determines the weld pool peak temperatures, and is the significant specie vaporizing. Assuming that there is little vaporization of copper from the molten pool, copper enrichment observed is the result of loss of aluminum. Based on the above assumption, the percentage loss of aluminum was estimated to be in the range of 15 to 24%. Loss of aluminum due to vaporization

combined with the volume shrinkage of the molten pool on cooling can cause the shrinkage cavities observed in the laser welds in alloy 2219.

Table 5.2 compares the percentage loss of aluminum with the volume of porosity determined by the density measurements for a few selected welds and shows a direct relation between these two effects. Although welds 102 and 107 have been made at different welding conditions, they still result in the same amount of heat input per unit length of the the weld. However, they show considerable difference in the percentage loss of aluminum as well as in the volume of porosity present. The higher peak temperatures in the welds associated with the higher input power intensity involved in weld 102 has resulted in the larger amount of aluminum vaporization as compared to the weld 107. Similarly, weld 103 made at 10 kw and a higher welding speed of 40 ipm has resulted in a smaller amount of aluminum vaporization and also smaller levels of porosity observed as compared to weld 102 made at 10 kw and a lower welding speed of 30 ipm. The higher welding speed results in lower power input per unit length of weld, with generally lower temperatures in the weld pool.

Table 5.2. Loss of aluminum related to porosity in alloy 2219.

	# 102	# 103	# 107
% loss of aluminum	24.12	17.48	15.07
Vol. of pores (cc × 100)	3.41	3.09	2.63

5.4.2 Alloys 5xxx

In the 5xxx series aluminum alloys, the most significant change in the weld metal composition was observed in aluminum and magnesium which were both

depleted and manganese which was enriched as compared to the base metal. Table 5.3 and 5.4 summarize the results of compositional changes in a few on-focus keyhole welds in alloys 5083 and 5456 respectively. Again, using similar arguments as in section 5.4.1 and from figures 3.2a and 3.3a, it is seen that manganese has significantly lower vapor pressure as compared to aluminum and magnesium in the melting point to boiling point range and beyond. It is therefore reasonable to assume that manganese vaporization is negligible and the enrichment in this element is solely caused by the loss in aluminum and magnesium. Based on this assumption, the loss in aluminum was estimated to be from 7 to 19% in alloy 5083, and up to 22% in alloy 5456. Similarly, the loss in magnesium was found to be from 18 to 26% in alloy 5083 and up to 25% in alloy 5456.

Table 5.3. Weld metal Composition in alloy 5083.

Weld	Al	Mg	Mn
Base Metal	94.44	4.36	0.62
10 kw, 20 ipm (# 202)	94.94	3.21	0.66
10 kw, 30 ipm (# 201)	94.24	3.62	0.72
10 kw, 40 ipm (# 203)	92.18	4.11	0.76
7.5 kw, 10 ipm (# 204)	94.74	3.64	0.66
7.5 kw, 20 ipm (# 205)	91.13	4.38	0.82
5 kw, 10 ipm (# 206)	95.34	4.29	0.77
5 kw, 15 ipm (# 204)	93.23	4.26	0.66

Table 5.4. Weld metal Composition in alloy 5456.

Weld	Al	Mg	Mn
Base metal	93.98	4.51	0.55
10 kw, 30 ipm (# 302)	93.26	4.74	0.70
10 kw, 40 ipm (# 301)	93.45	3.99	0.65

Table 5.5 and 5.6 compare the percentage loss of aluminum and magnesium as well as the volume of porosity observed among the different welds in alloys 5083 and 5456 respectively. Several inconsistencies are evident among these alloys as well as within each alloy. For instance, comparing welds 201 and 203 with increasing welding speeds for the same input power of 10 kw, percentage loss in aluminum increased from 12.49 to 19.19, but the percentage loss in magnesium decreased from 26.62 to 22.25, and so did the porosity volume. However, between welds 201 and 207 with equal power input per unit lengths but different welding conditions, both the percentage loss in aluminum and magnesium decreased, but the porosity volume increased. Further, comparing the welds 201 and 203 in alloy 5083 with the welds 302 and 301 in alloy 5456, although the trend in porosity volume is similar, the trends in percentage loss of aluminum and magnesium are reversed.

It is clear that the higher magnesium content in the 5xxx series alloys results in much larger amounts of porosity in the weld as compared to the magnesium free alloy 2219. But, the porosity volume could not be correlated to the percentage loss of aluminum or magnesium and thereby the welding parameters in any consistent manner, as was possible with alloy 2219.

Table 5.5. Loss of aluminum and magnesium related to porosity in alloy 5083.

	# 201	# 203	# 207
% loss of aluminum	12.49	19.19	7.26
% loss of magnesium	26.62	22.25	18.81
Vol. of pores (cc × 100)	13.21	11.30	16.63

Table 5.6. Loss of aluminum and magnesium related to porosity in alloy 5456.

	# 302	# 301	# 307
% loss of aluminum	22.03	15.87	–
% loss of magnesium	17.52	25.06	–
Vol. of pores (cc × 100)	18.18	9.43	19.24

5.4.3 Summary

Porosity and shrinkage cavities were observed only in the higher intensity keyhole mode welds, with the associated significant vaporization of aluminum as well as other volatile alloying elements. A direct corelation was observed between the loss of aluminum and the volume of porosity measured in alloy 2219. This alloy exhibited large shrinkage cavities in the middle of the weld and very little amount of spherical gas porosity of the kind observed in the 5xxx alloy. The 5xxx alloys showed a large amount of spherical porosity with large pores accumulated near the top surface of the welds. The large bubble formation is attributed to the boiling of highly volatile magnesium present in the 5xxx alloys. It is conceivable that

considerable amount of the bubbles escaped from the molten metal, but sufficient quantity of bubbles were trapped in the weld resulting in the large volume of spherical porosity observed in these alloys in addition to the large cavities in the middle of the welds. The aluminum alloys have a large solidification range, which results in a large mushy zone during solidification as seen in figure 5.35 and 5.36 which are discussed later. As solidification progresses, the large mushy zone prevents the bubbles to float up and escape, resulting in the entrapment of the large amount of spherical pores.

5.5 Microstructures in Aluminum Laser Welds

The weld metal properties are dependent upon the microstructures and segregation patterns in the weld zone, and are a function of the welding process variables, the weld geometry, and the material thermal properties. The welding process also effects the properties of the base metal surrounding the weld zone called the heat affected zone (HAZ). In the non-heat treatable aluminum alloys in the series 1xxx, 3xxx, 4xxx and 5xxx, the strengthening mechanism employed is cold working. Thus, for these alloys, the welding cycle effects the HAZ by annealing it to varying degrees of strength reduction. However, in the heat-treatable aluminum alloys belonging to the series 2xxx, 4xxx, 6xxx and 7xxx, the principal strengthening mechanism is the controlled precipitation of the supersaturated solutes in the alloy. This is achieved by solution heat treatment and quenching to dissolve the solute into the matrix, followed by an aging process to induce the precipitation. Welding of the precipitation strengthened aluminum alloys therefore results in a variety of structures in the HAZ ranging from the fusion zone, solid solution zone, overaged zone to unaffected base metal. In the following paragraphs, typical structures observed in transverse sections of a few selected welds are described.

5.5.1 <u>Alloy 2219</u>

Base metal microstructure of alloy 2219 in the annealed condition is shown in figure 5.12. The microstructure consists of elongated grains in the rolling direction of the solid solution with small particles of $CuAl_2$ (light) widely distributed, along with larger and darker particles of $(Fe,Mn)_3SiAl_{12}$. The strengthening heat-treatment would have resulted in much larger quantity of precipitates of the intermetallic phase $CuAl_2$ agglomerating into larger globules.

The weld zone for a 10 kw, 20 ipm on-focus weld is shown in figures 5.13 to 5.16. The weld microstructure consists of α aluminum phase in a dendritic network of the Θ phase ($CuAl_2$). However, the substructure varies widely from the edge of the fusion zone to the center of the weld. In figure 5.13, the edge of the fusion zone is shown with the unmelted region in the bottom right side of the figure. The weld zone consists of a small region of cellular grains changing rapidly to columnar dendritic structure within a few microns. Figure 5.14 of a region further interior and away from the weld boundary shows the columnar dendritic structure in more detail and clarity. Finally, figure 5.15 shows equiaxed grains from the interior of the weld far from the weld boundary. The primary dendrite arm spacing in this equiaxed region is finer than in the outer edges of the weld, indicating smaller thermal gradients at the late stages of solidification. However, the dendrite arm spacing does vary considerably within this equiaxed region. It is to be noted that for a reliable measurement of the dendrite arm spacing, the sections must be parallel to the growth direction - this is easily accomplished in the outer regions of the welds where columnar dendrites are observed with growth direction clearly defined. However, in the interior of the weld with the equiaxed grains randomly oriented, average values of dendrite arm spacing were taken from many grains.

Figure 5.12   Base metal in alloy 2219 (x 100).
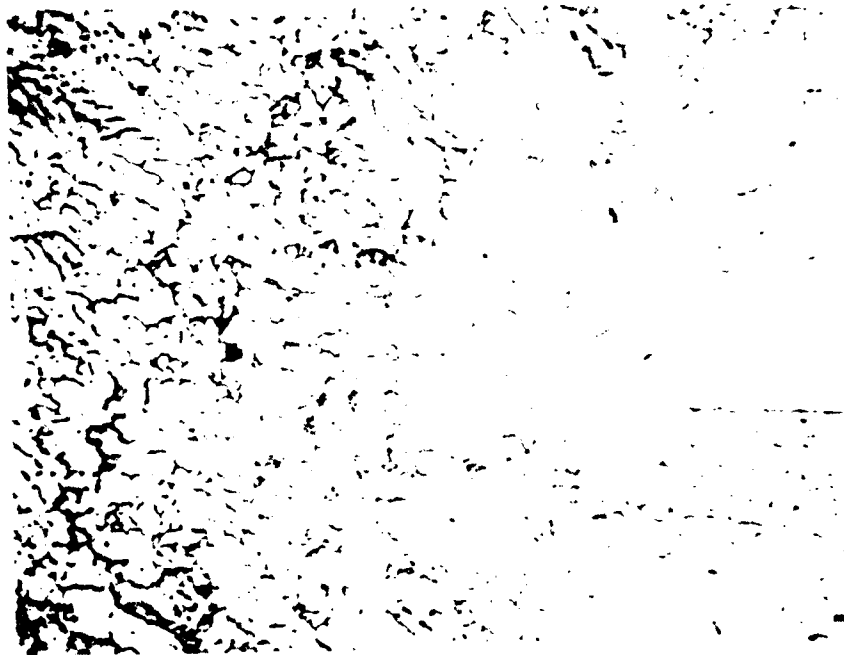
Figure 5.13   Fusion zone boundary with base metal on the
right; cellular structure changing to cellular
dendritic in weld zone (x 200).
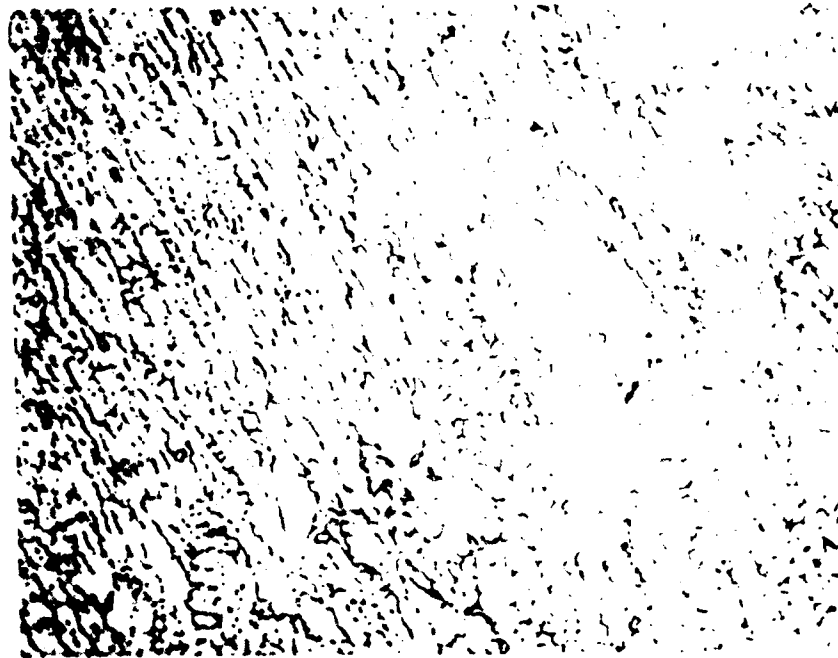
Figure 5.14   Weld metal near the fusion boundary;
columnar dendritic structure (x 200).
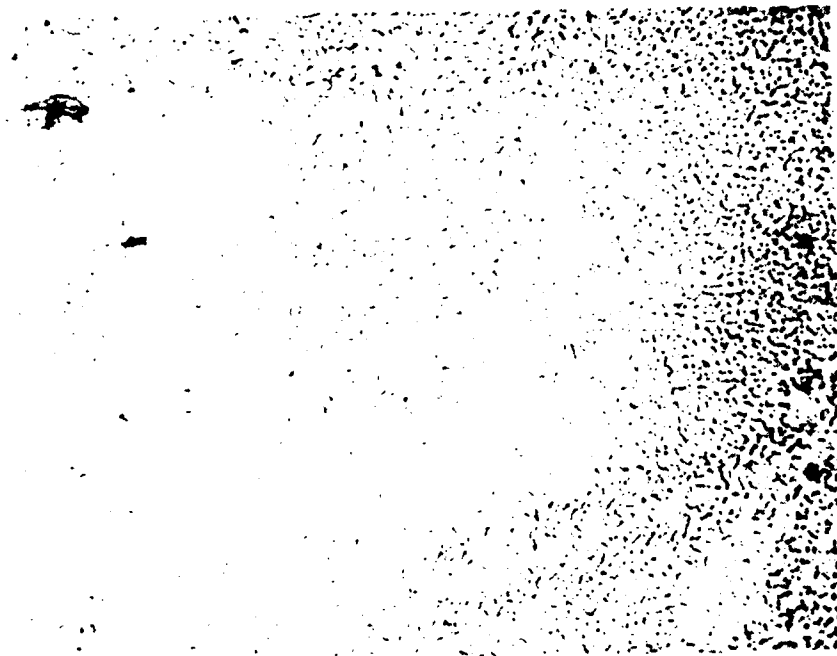
Figure 5.15   Weld metal in the middle of the weld; equiaxed
dendrites (x 200).

Figure 5.16   Fusion zone boundary showing epitaxial growth
              from parent metal liquation and agglomeration
              of θ phase in HAZ (x 500).

In the HAZ close to the fusion boundary, there is evidence of incipient melting as well as agglomeration of the Θ phase as seen in figure 5.16. As this alloy was originally in the annealed condition, other structures like the overaged zone are not present.

From figure 5.9a showing the macro-section of the weld, the weld appears to be a superimposition of two welds – 1. a wide and shallow weld made on top of 2. a narrower deep penetration weld. Also, several bands of columnar dendritic regions interspersed with equiaxed grains are evident. Such banding was unique to this alloy and was observed in both the on-focus as well as off-focus welds.

5.5.2 Alloys 5xxx

As the compositions of the aluminum alloys 5083 and 5456 vary only marginally, the weld microstructures observed were quite similar. Thus, only the microstructures in a keyhole laser weld in alloy 5083 are presented here as representative samples of both the alloys. Figure 5.17 shows the base metal structure of the annealed alloy showing light outlined particles of irregular shaped intermetallic compound $(Fe,Mn)Al_6$. Also, some dark particles of the insoluble Mg_2Si are seen. Rapid cooling has resulted in the retention of the Mg_2Al_3 phase in the solid solution. Elongated grains in the rolling direction are evident.

The weld microstructures are shown in figures 5.18 and 5.19. In figure 5.18, the unmelted region is on the bottom right end of the picture. The weld structure consists of Mg_2Al_3 at the dendrite boundaries in a matrix of the solid solution. Not much variation in the dendrite arm spacing is seen from the edge of the weld to the center. In this non-heat treatable aluminum alloy, the structures in the HAZ are virtually unchanged.

Figure 5.17   Base metal in alloy 5083 (x 200).

Figure 5.18   Fusion zone boundary with base metal on the
right (x 200).

124
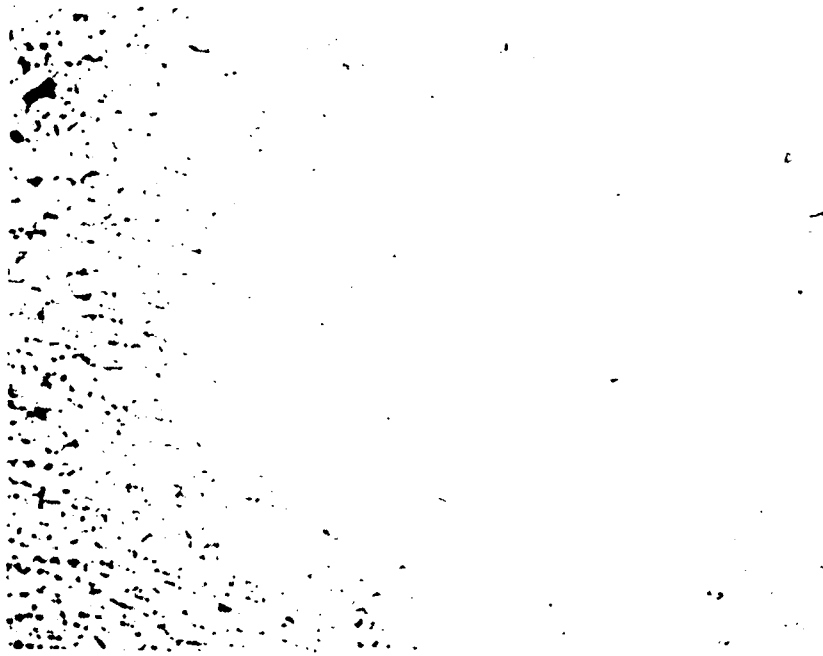
Figure 5.19   Weld metal in the middle of the weld (x 200).

5.5.3 Alloy 6061

The parent metal microstructure in the 1.27 cm thick plate in alloy 6061.T6 is shown in figure 5.20. The structure is made up of elongated grains of aluminum solid solution with fine gray particles of the intermetallic $(Fe,Mn,Cr)_3SiAl_{12}$ along with dark particles of Mg_2Si precipitate distributed throughout the matrix. In the 4 mm thick plate of the same alloy used for the conduction mode welds, similar structures were observed with more precipitation of Mg_2Si in the matrix.

The HAZ microstructures in the thick plate 10 kw, 40 ipm on-focus laser weld are shown in figures 5.21 and 5.22 representing the overaged region and the fusion boundary respectively. In the overaged region, the Mg_2Si particles have grown due to further precipitation from the solid solution. In figure 5.22, liquation of the Al-Mg_2Si eutectic is evident around the ground boundaries. Also, some dark regions of the eutectic agglomeration can be seen.

The weld structures for the same weld are shown in figures 5.23 and 5.24. The structure consists of an interdendritic network of the Al-Si eutectic in the aluminum solid solution matrix. The unmelted region is on the bottom right side of the figure 5.23, and the columnar dendritic structure is clearly evident in the weld zone. The equiaxed dendritic nature of the structure in the middle of the weld is shown in figure 5.24. Again, the primary dendrite arm spacing progressively decreases from the edge of the weld to the weld center.

For the conduction mode welds in the 4 mm thick plates, the structures were slightly different. For the 10 kw, 20 ipm conduction mode weld, figure 5.25 and 5.26 show the same region of the fusion boundary at the bottom of the weld at different magnifications. More extensive liquation of the eutectic is seen in the HAZ. Also agglomeration of the eutectic into large globules is seen in this region.
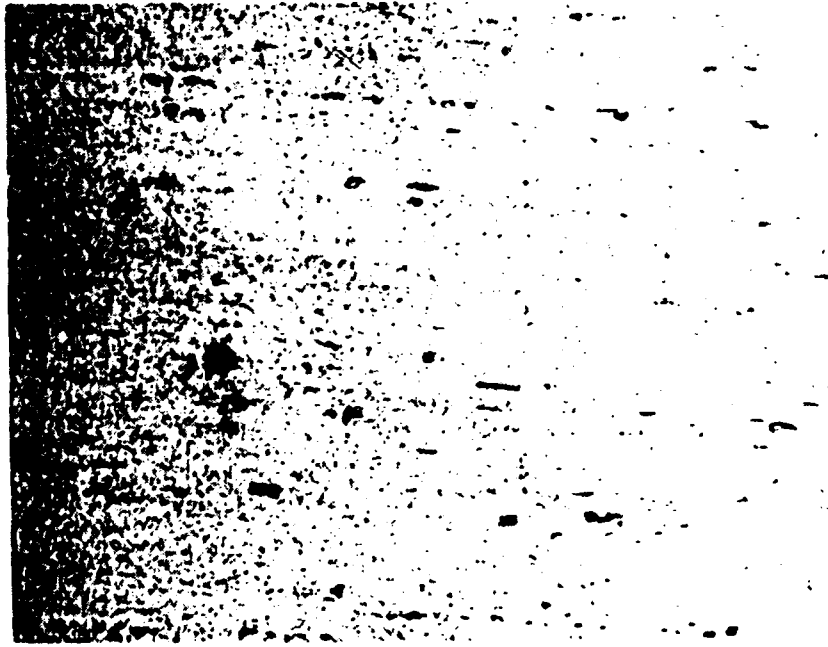
Figure 5.20   Base metal in alloy 6061-T6 (x 500)
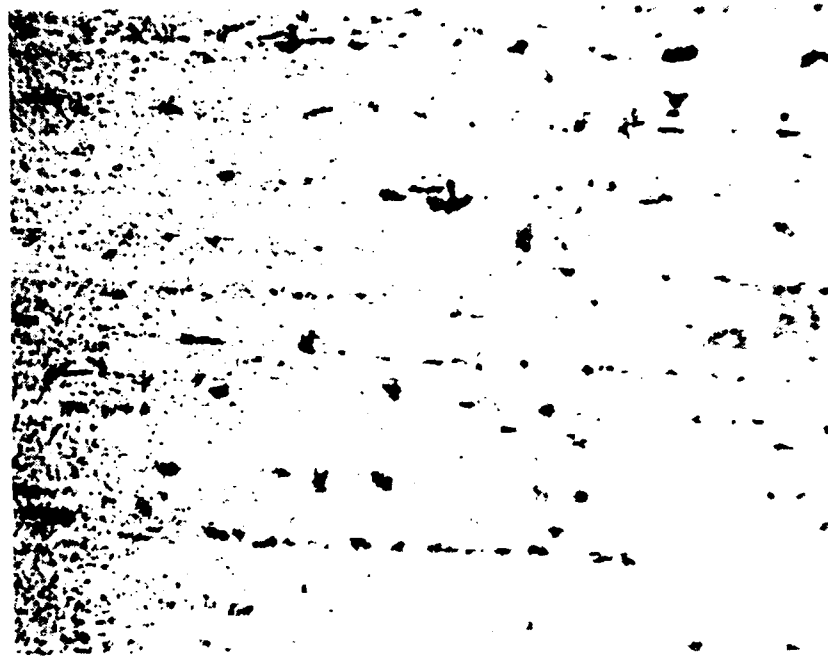
Figure 5.21   HAZ showing overaged region (x 500).
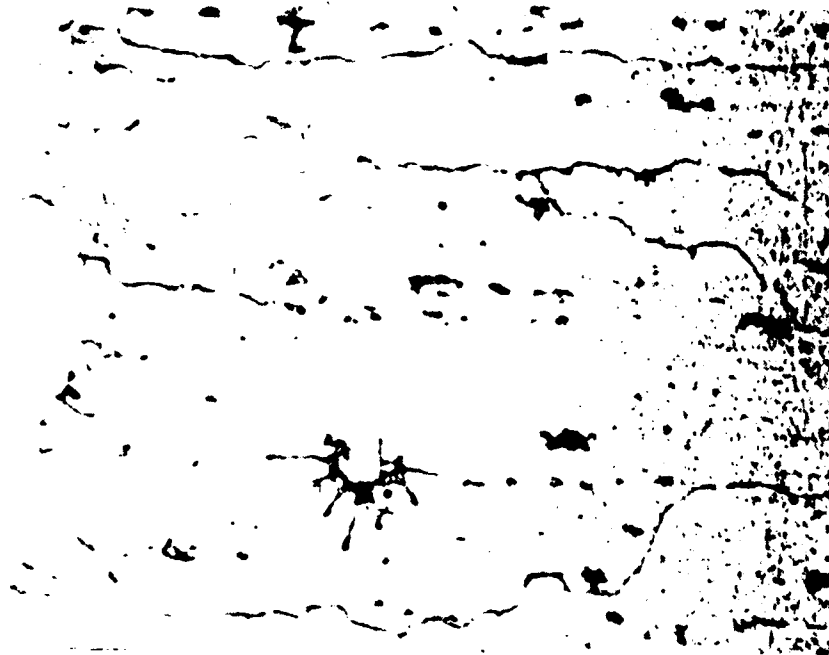
Figure 5.22 Fusion zone showing liquation and agglomeration of eutectic; weld is on the right (x 500).

Figure 5.23 Fusion zone showing columnar dendrites at the weld boundary; epitaxial growth from the base metal on the right (x 250).
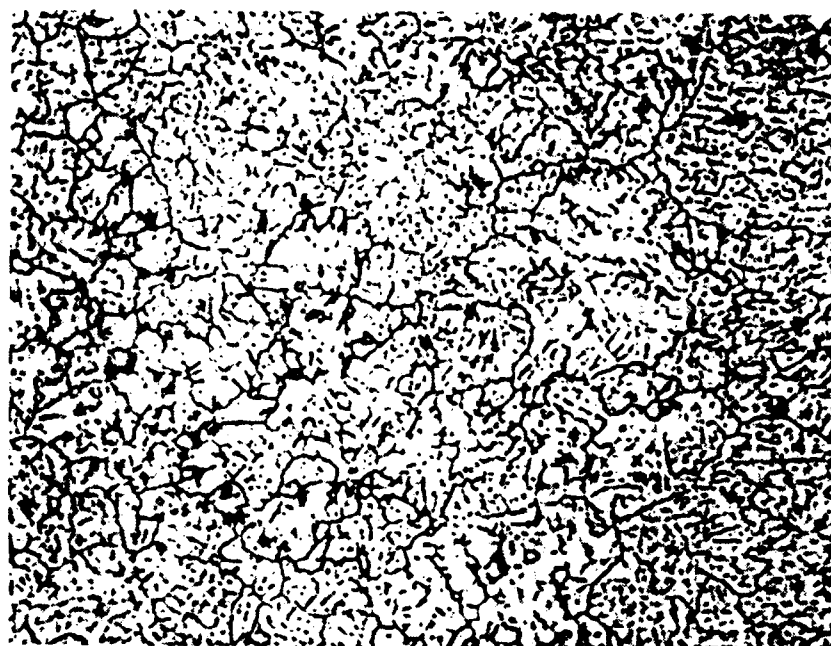
Figure 5.24   Equiaxed dendritic structure in the middle of
weld (x 250).
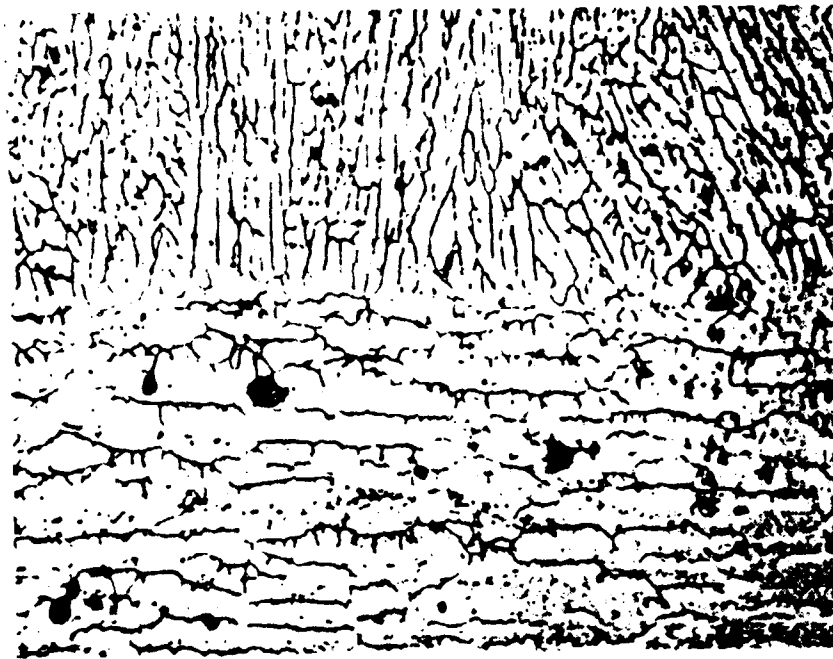
Figure 5.25   Fusion zone boundary in 0.4 cm thick 6061-T6;
large amount of liquation and agglomeration of
eutectic in HAZ in lower half; columnar
dendrites in weld in top half (x 200).

Figure 5.26   Fusion zone at higher magnificaion (x 500).

Keller's reagent used for the etching has dissolved the Mg_2Si and has resulted in the agglomeration seen as a void. The weld structures are shown in the figures 5.27 and 5.28. The columnar dendritic structure close to the edge of the weld changes to more equiaxed dendritic as seen in these figures. Compared to the welds in the 1.27 cm thick plates, the primary dendrite arm spacing is much larger. Also, the amount of the interdendritic eutectic present is higher in the thinner plate welds.

5.6 Thermal Modeling of Aluminum Laser Welds

The finite element program THERM described in chapter 4 was used to model the laser welds in aluminum alloys. The temperature dependent thermal properties used for the modeling are shown in table 5.7 for each of the four alloys.[81,82] As the chemical composition varies only marginally between the alloys 5083 and 5456, and the experimental results for the weld bead dimensions are also very similar, these two alloys were not differentiated for the modeling. Alloy 2219 has slightly higher thermal conductivity as well as volumetric specific heat as compared to the other three alloys. Also, it has the largest solidification range of 100 °K, as compared to 64 °K for the 5xxx alloys and 70 °K for alloy 6061. The temperature dependent specific heat data was available only for alloy 2219, and it was therefore assumed constant for the other three alloys. The finite element mesh of 136 elements and 170 nodes consisting of 4 and 5 node elements is shown in figure 5.29.

For modeling the aluminum laser welds, the surface heat flux model was used for the low penetration conduction mode welds, and the internal heat source model was used for the deep penetration keyhole welds. A gaussian distribution of energy was assumed in the laser beam for modeling these welds. The effective beam spot radius r_0 for the on-focus and off-focus welds was determined from spot burns on thick acrylic slabs. The beam spot diameters for the on-focus and off-focus welds
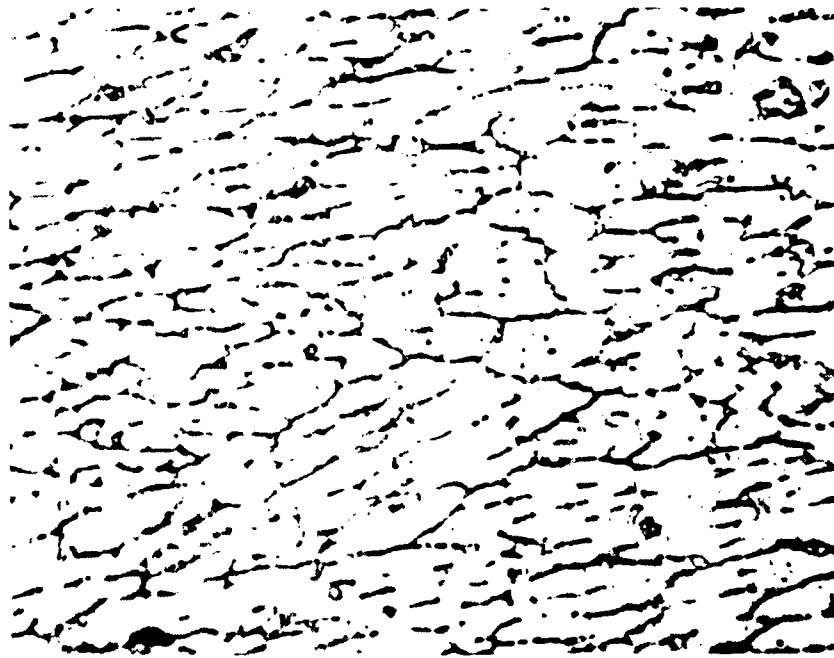
Figure 5.27   Large dendritic structure near weld boundary
(x 500).
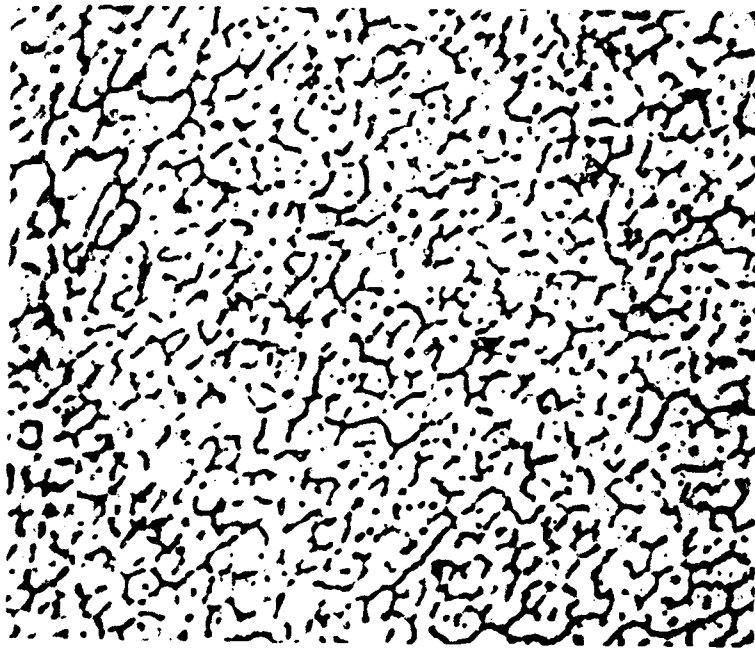
Figure 5.28   Finer equiaxed structure in the middle of weld
(x 500).

Table 5.7. Temperature dependent thermal properties for aluminum alloys.[81,82]

	Alloy 2219		Alloy 5xxx		Alloy 6061	
	Temp. (°K)	Value	Temp. (°K)	Value	Temp (°K)	Value
Thermal Conductivity (w/cm °K)	273.0	1.170	273.0	1.090	293.0	1.067
	323.0	1.280	323.0	1.280	373.0	1.192
	816.0	1.840	847.0	1.470	855.0	1.611
	916.0	1.963	911.0	1.495	925.0	1.700
Specific Heat (j/cc °K)	300.0	2.426		2.114		2.114
	366.0	2.576				
	589.0	2.908				
	816.0	3.515				
	916.0	3.783				
Solidus (°K)		816.0		817.0		855.0
Liquidus (°K)		916.0		911.0		925.0
Lat. Heat of Fusion (j/cc)		1073.82		1016.80		1016.42
Lat. Heat of Vap. (kj/cc)		28.43		28.43		28.43

*** TEMPERATURE DISTRIBUTION IN LASER WELDS ***

Mesh Used for Finite Element Analysis.

Alloy : 2219.   Power (kw): 10.   Eff : .35   Time (sec): 0.
Focus : 0.   Speed (cm/s): 1.27   Y0 : 1.27   Position (cm): 0.
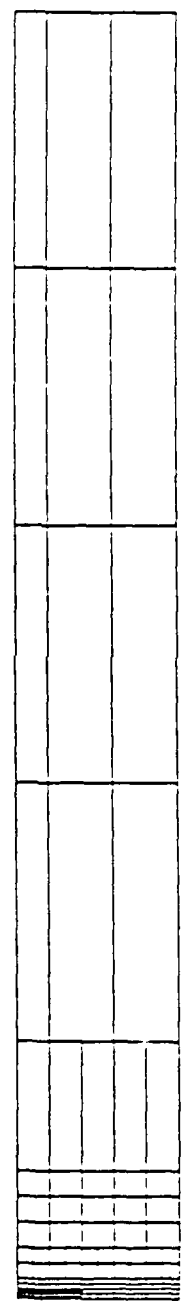
Figure 5.29 Mesh used for analyzing aluminum laser welds.

were estimated to be 0.08 and 0.12 cm respectively. The effective depth y_0 of the internal heat source was assumed to be 1.27 cm or the plate thickness. For alloy 2219, this value resulted in overprediction of the weld penetration, and therefore, a value of 1.0 cm was used for this alloy.

5.6.1 Absorptivity

To accurately model the laser welds, an effective absorption coefficient must be assumed to ensure that only the laser energy actually absorbed by the material is used in the heat transfer analysis for each of the welds. The overall welding process efficiency (η) presented in section 5.1.5 was used to estimate the absorptivity values to be used for the modeling. As Banas[26] has discussed, the overall process efficiency η is defined as

$$\eta = \eta_a \cdot \eta_m.$$

Here, η_a is the absorptivity which depends on the material and surface characteristics as discussed in section 2.3, and η_m is the melting efficiency defined as the ratio of the energy required to melt the material within the weld zone to the absorbed laser power. Both the melting efficiency and the absorptivity depend on the welding mode. At low intensity conduction mode welds, the melting efficiency is lower than at high intensity levels, as more of the heat is conducted away faster into the material. Also, the absorptivity changes dramatically with the keyhole formation as discussed in section 2.3. These two factors result in the overall process efficiency changing with the welding parameters as seen in figure 5.5. The absorptivity values used in the calculation of the heat input term as per section 4.3 were estimated based on the above process efficiency data; absorptivity values averaging 1.5 times the process efficiency generally gave the best results in the predictions of the weld bead geometry.

5.6.2 Prediction of Weld Geometry

Laser welds in aluminum alloys were analysed using the finite element program THERM, and the predicted weld geometries compared with the experiment.l results. The solidus isotherm was defined as the boundary of the weld zone. Accurate prediction of the cross-section of the weld is widely used as an important test for any weld heat transfer model. As discussed in chapter 4, in the cross-sectional approach for modeling partial to full penetration welds in thick plates, the thermal history in the reference plane is predicted at successive time steps as the heat source moves towards and passes the reference plane. A three dimensional picture of the weld pool can thus be assembled as is shown in the figure 5.30 for a 10 kw, 1.27 cm/sec (30 ipm) on-focus weld in alloy 2219. For clarity, the top view and the longitudinal section of the same weld pool are shown in figures 5.31 and 5.32 respectively. It is seen from figure 5.32 that the maximum weld penetration in the weld occurs slightly after the heat source has passed the reference plane (0. in the x-axis). But, the maximum top bead width is seen in figure 5.31 to occur a considerable distance behind the peak penetration plane. The predicted weld cross-sections are obtained by the projection of the three dimensional weld pool on to the reference plane.

Table 5.8 shows the selected aluminum laser welds modeled covering a wide range of welding parameters. Also shown in the table are the absorptivity values used for modeling these laser welds; these values were derived from the process efficiency data discussed earlier. The type of heat source assumed (surface heat flux or internal heat source) for each of the welds is also indicated. Figures 5.33 to 5.40 show the weld cross-sections of these welds in the alloys 2219, 5xxx and 6061. The predicted weld profiles match reasonably well with the experimental results. The weld penetration, top bead width as well as the weld cross-sectional
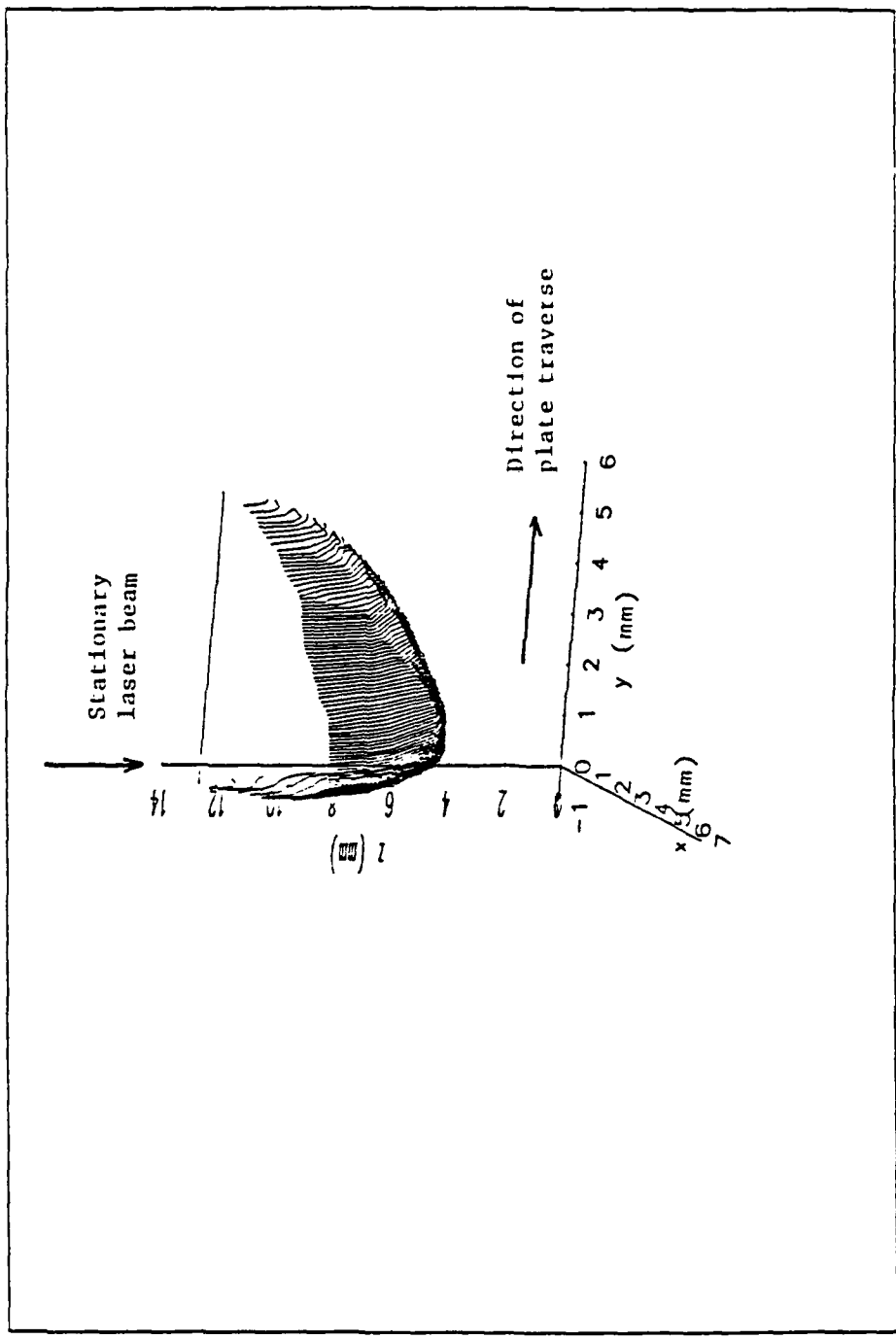
Figure 5.30   Laser weld pool in alloy 2219 (10 kw, 1.27 cm/sec).
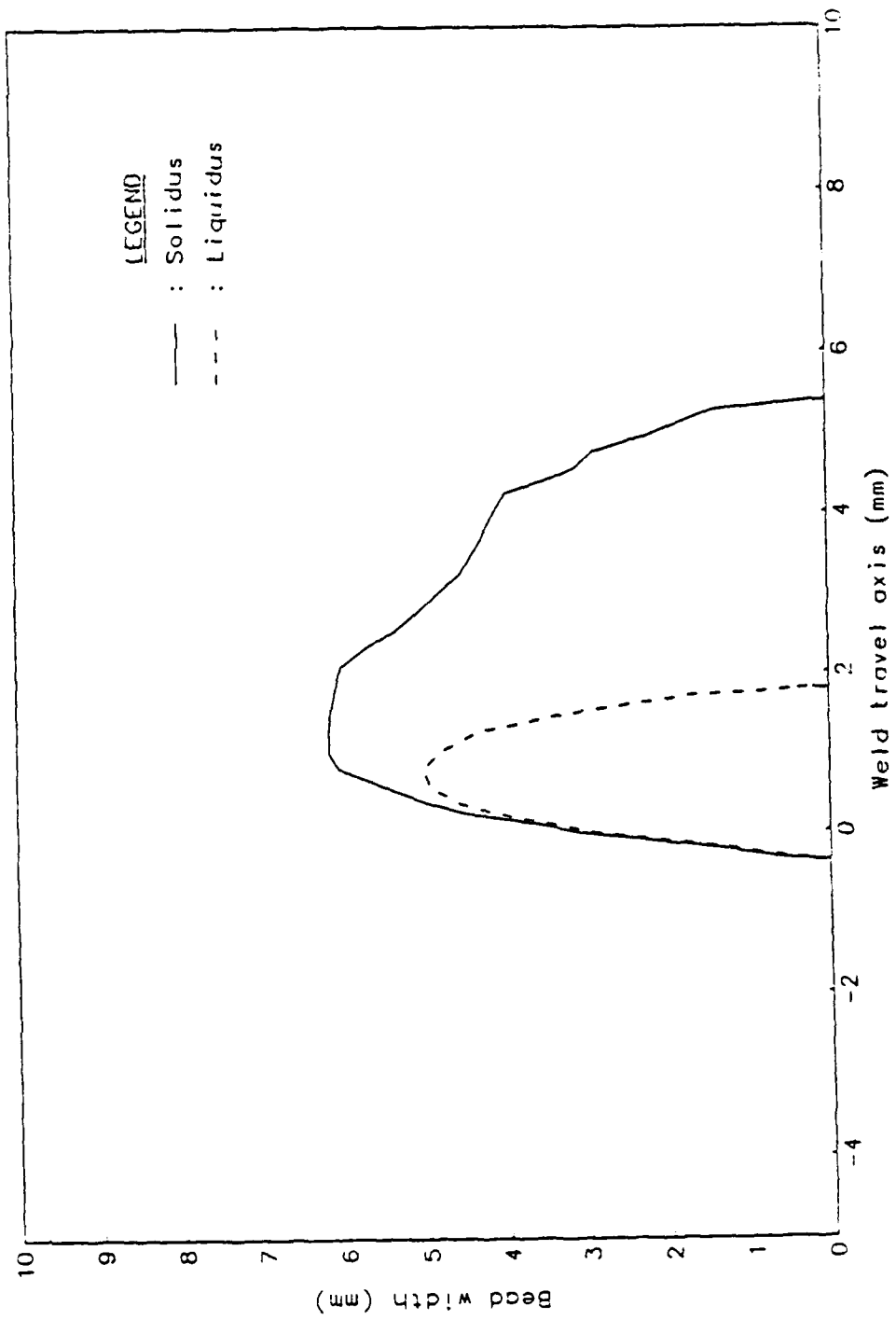
Figure 5.31 Top view of laser weld pool in alloy 2219 (10 kw. 1.27 cm/s).
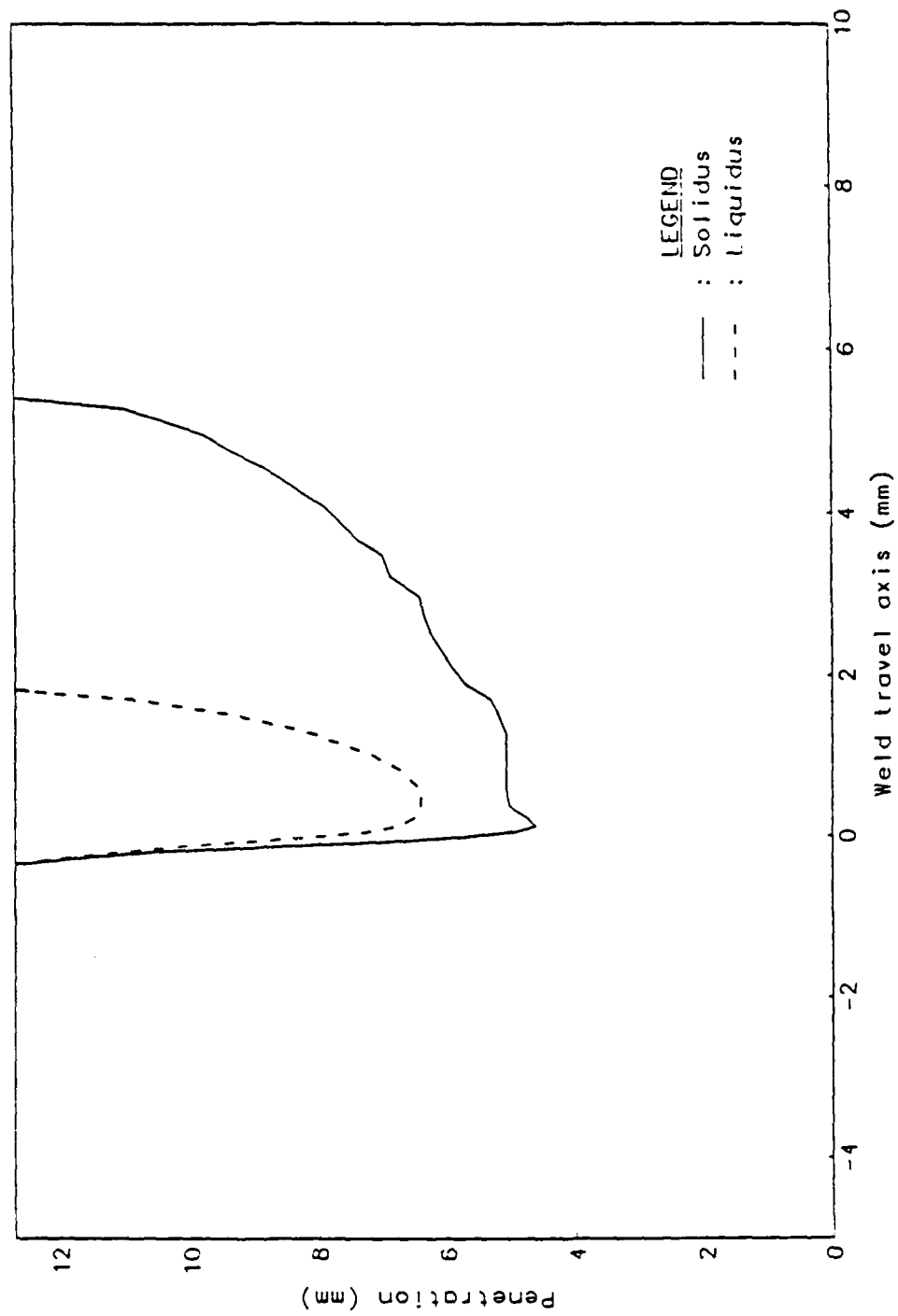
Figure 5.32 Long section of laser weld pool in alloy 2219 (10 kw, 1.27 cm/s).
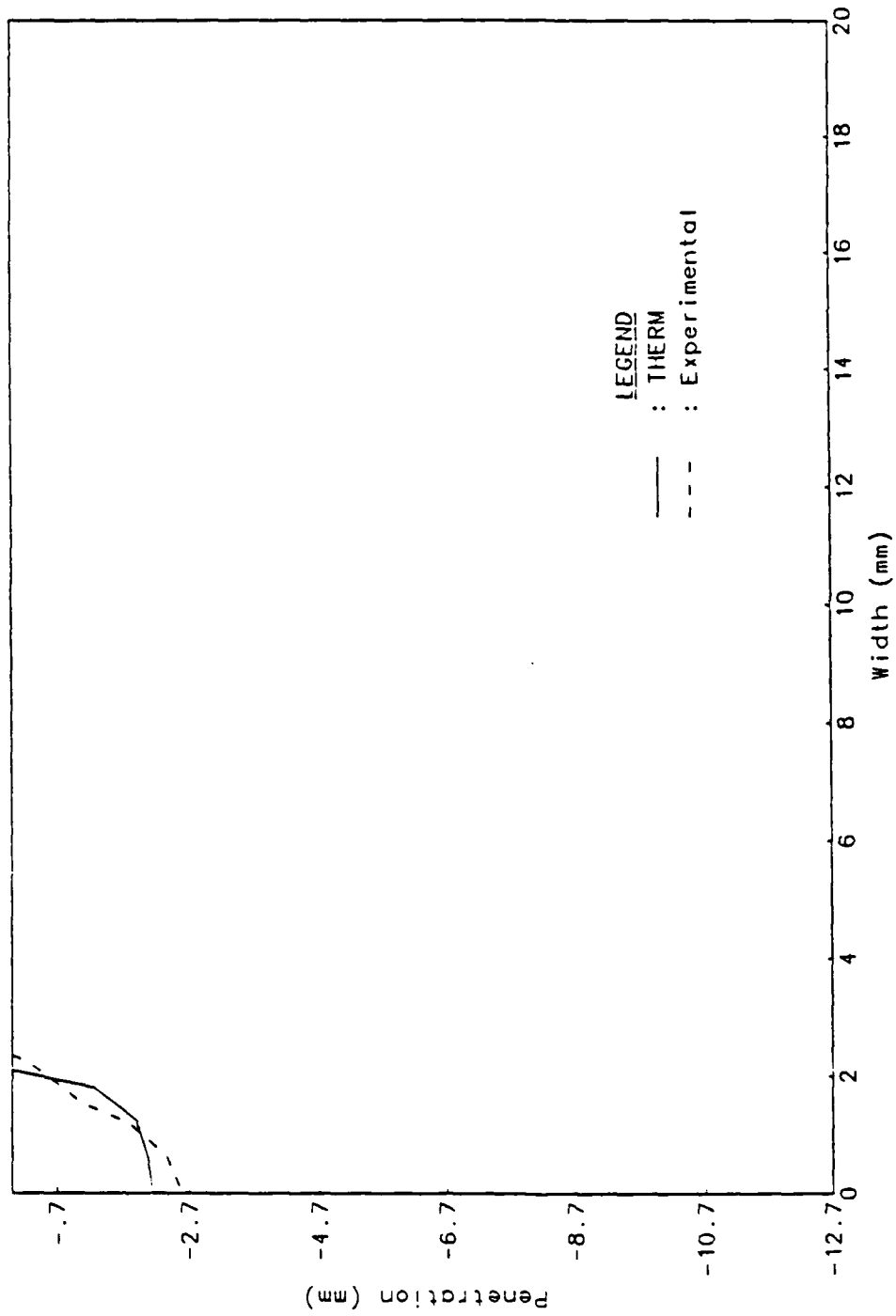
Figure 5.33 Laser weld cross-section in alloy 2219 (5 kw, 0.635 cm/sec).
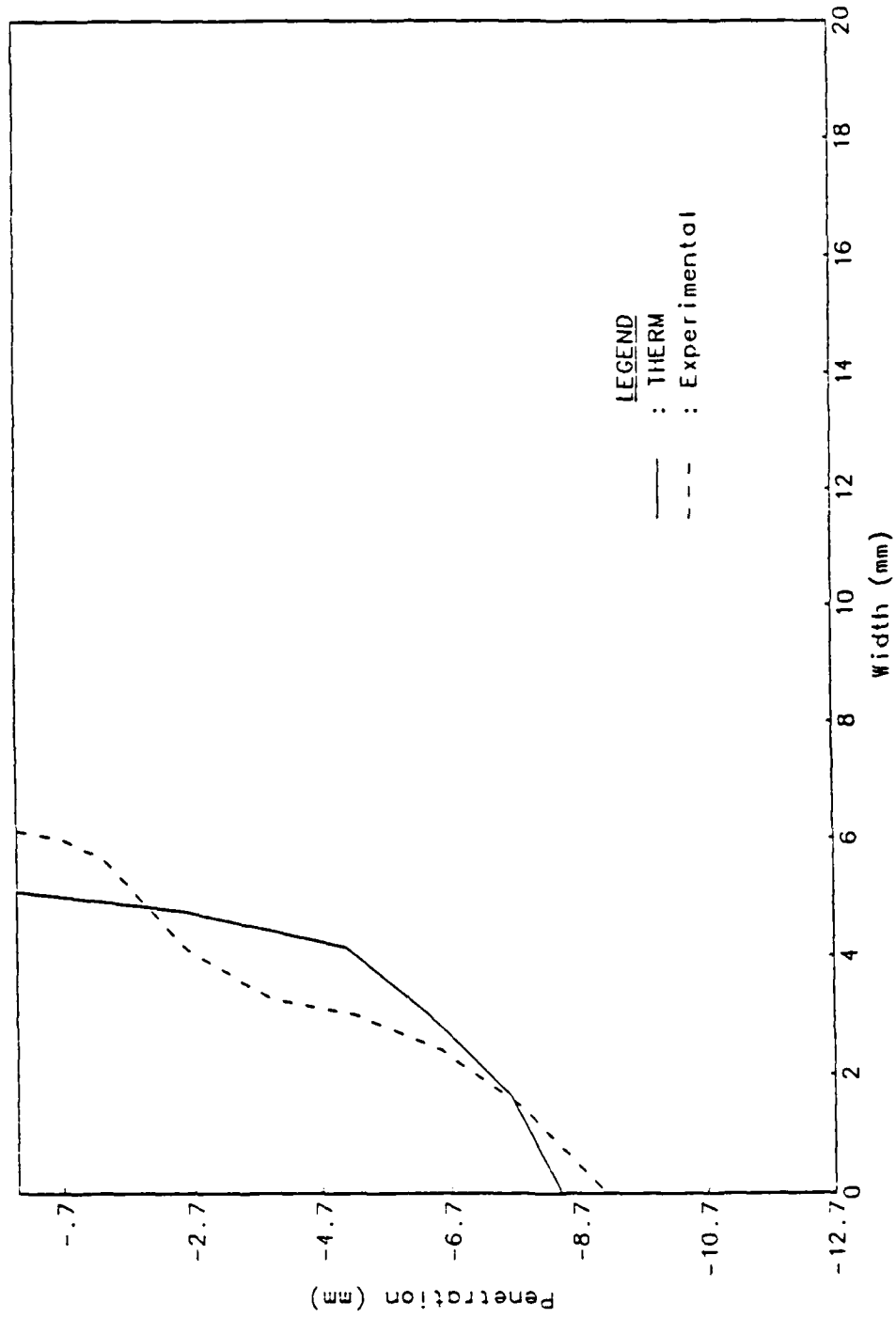
Figure 5.34 Laser weld cross-section in alloy 2219 (10 kw, 1.27 cm/sec).
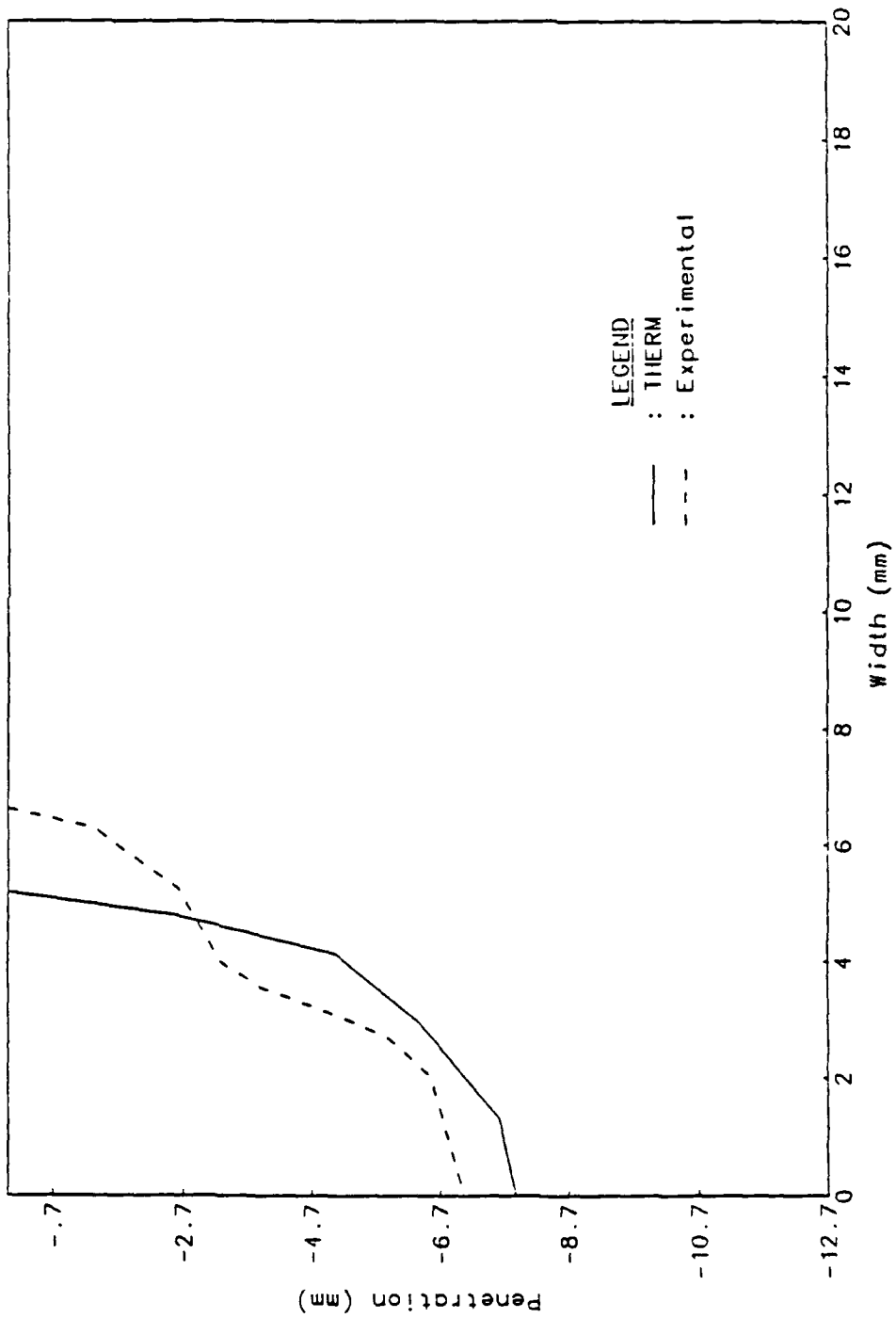
Figure 5.35 Laser weld cross-section in alloy 2219 (10 kw, off-focus).

142
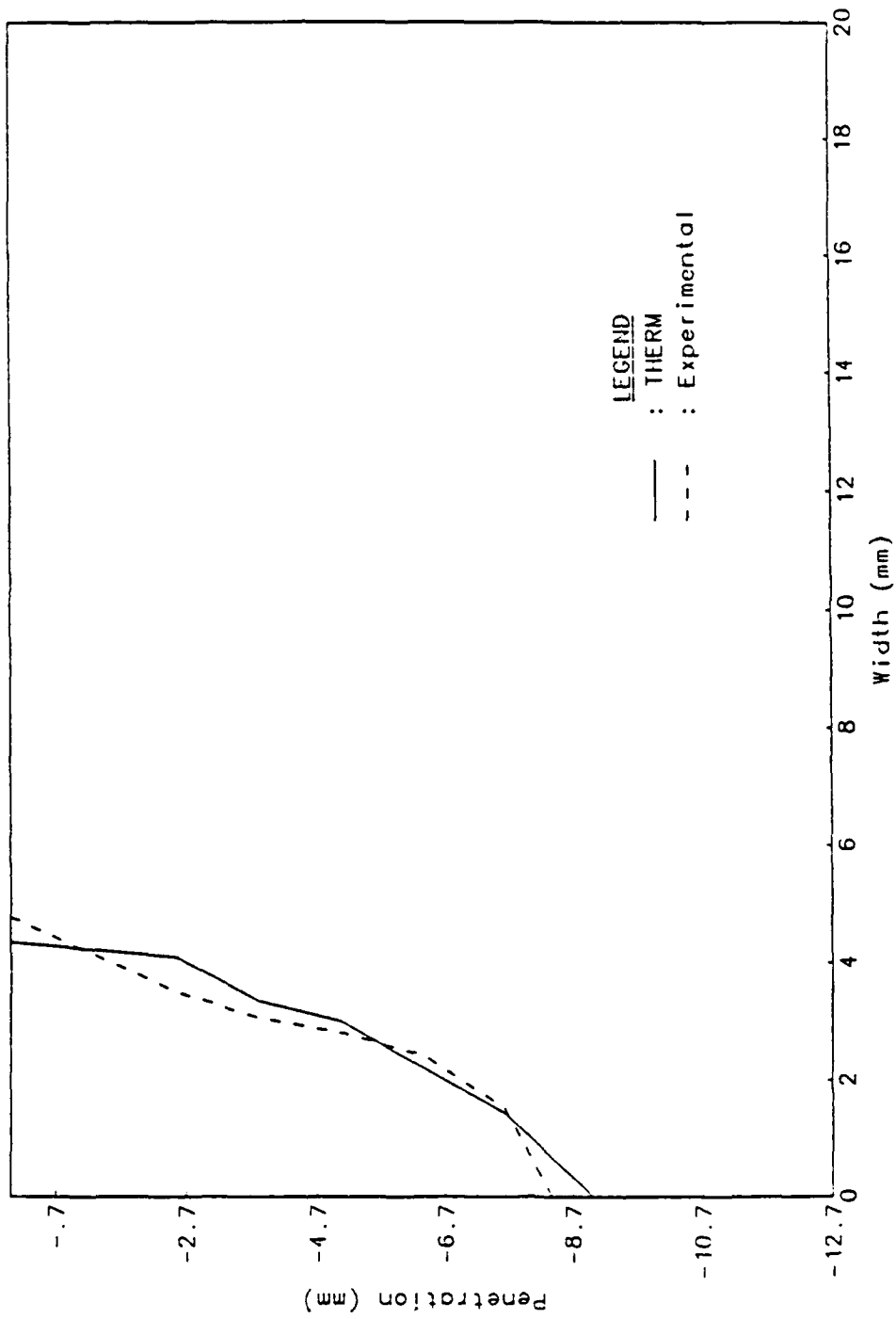
Figure 5.36 Laser weld cross-section in alloy 5xxx (5 kw, 0.635 cm/sec).
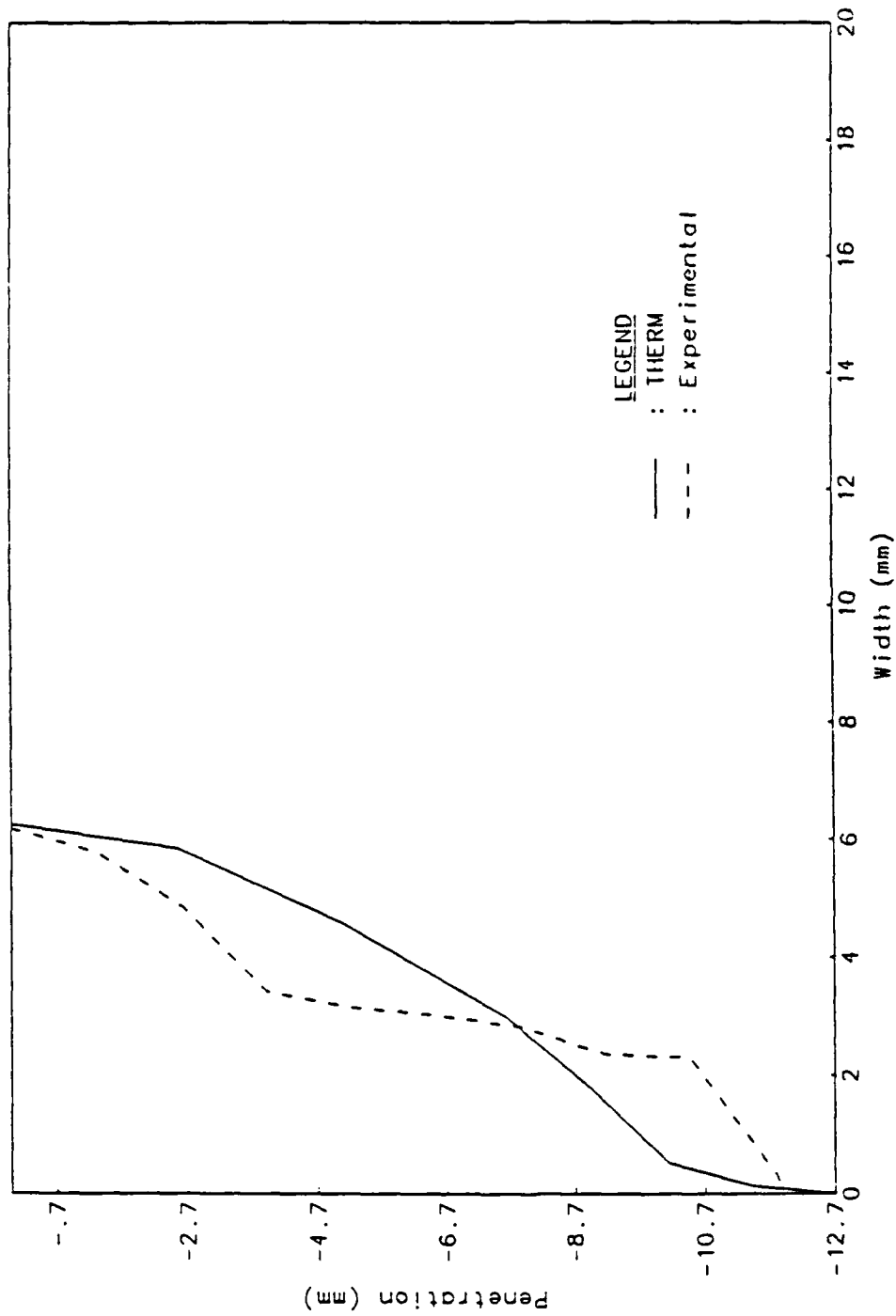
Figure 5.37 Laser weld cross-section in alloy 5xxx (10 kw. 1.27 cm/sec).
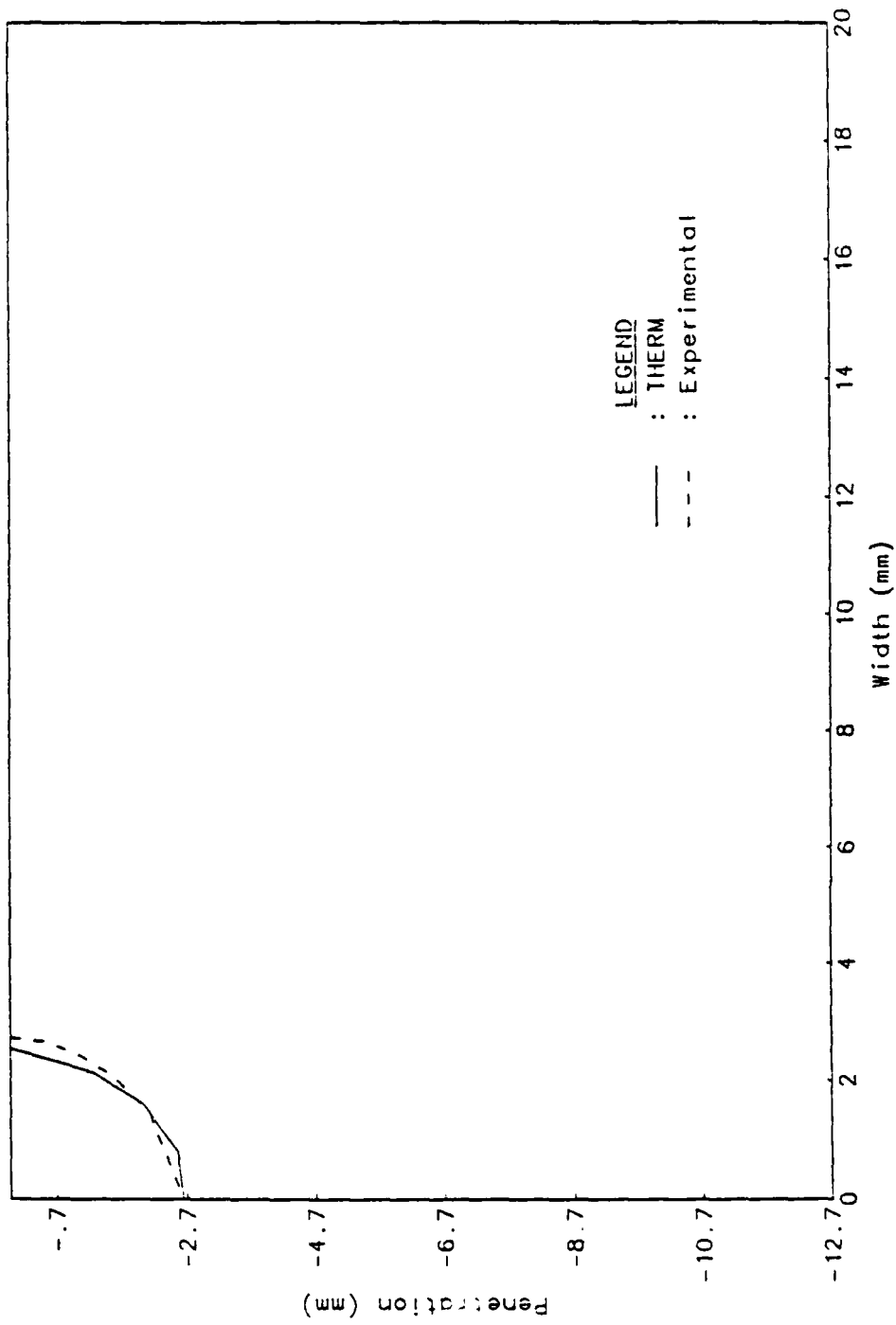
Figure 5.38 Laser weld cross-section in alloy 5xxx (5 kw, off-focus).

145
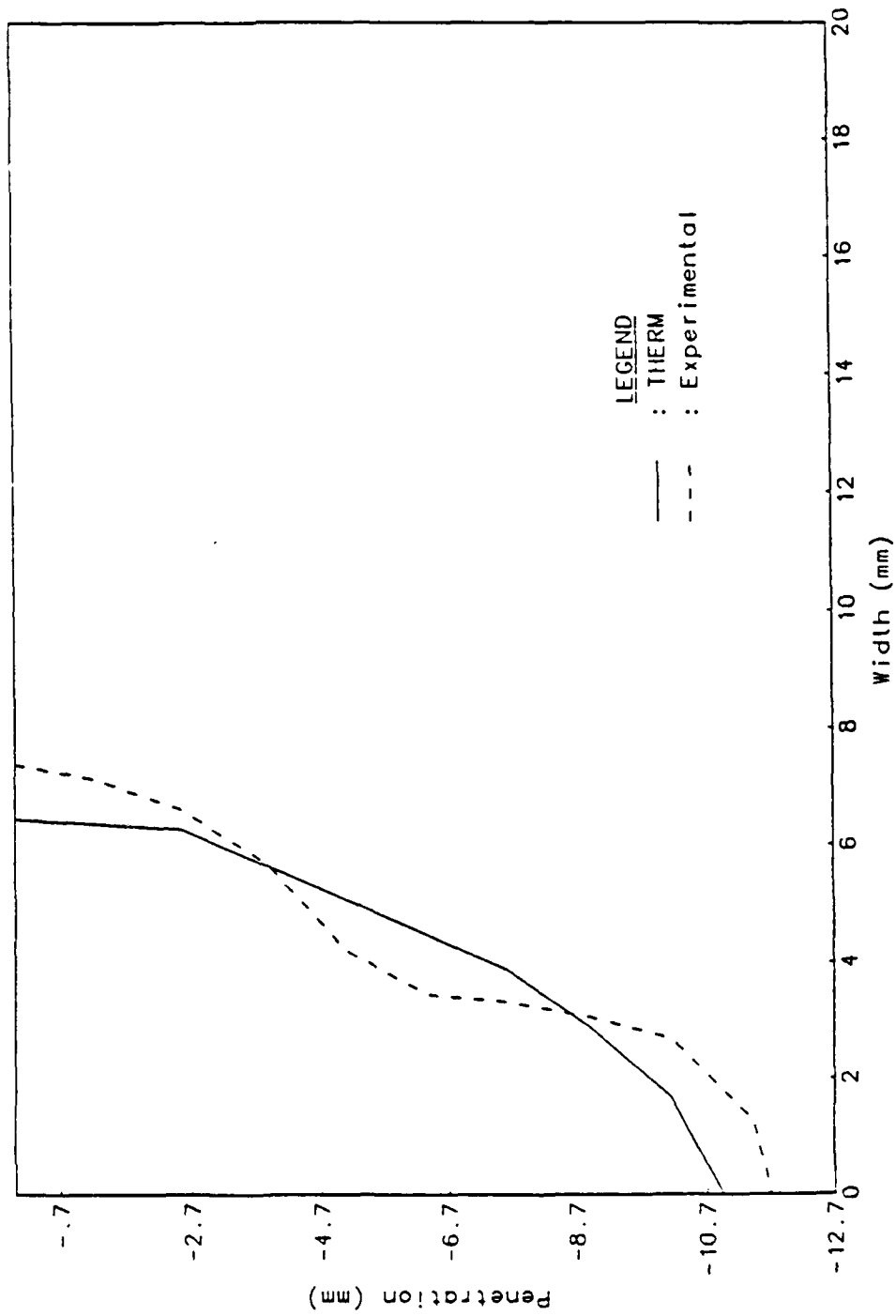
Figure 5.39   Laser weld cross-section in alloy 5xxx (10 kw, off-focus).
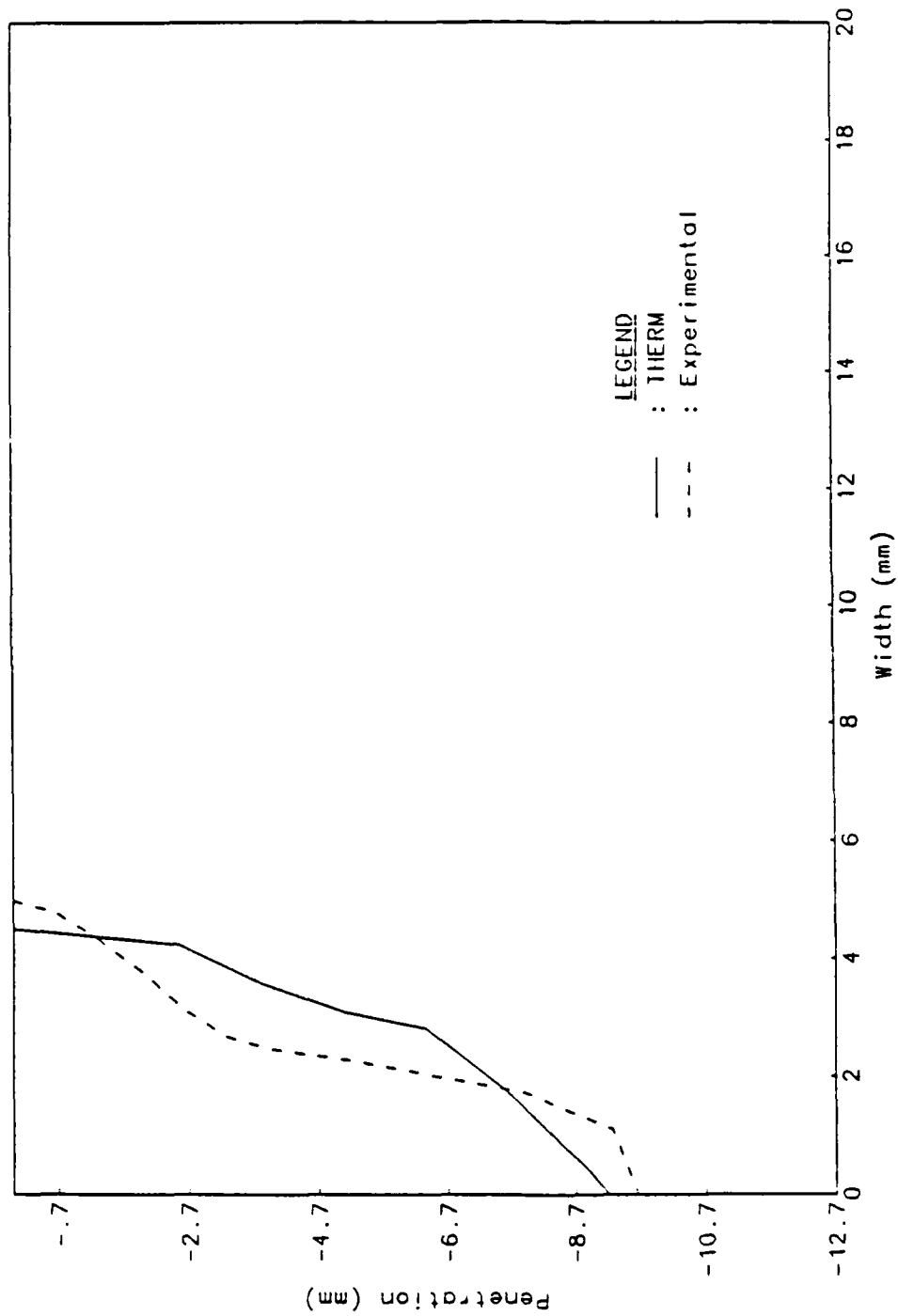
Figure 5.40   Laser weld cross-section in alloy 6061 (10 kw, 1.27 cm/sec).

area are in good agreement with the experimental data. However, the model does not accurately predict the nail-head shape of deep penetration welds.

Table 5.8. Absorptivity values used in modeling aluminum laser welds.

Welds	Alloy 2219	Alloy 5xxx	Alloy 6061
5 kw, 0.635 cm/sec (on-focus)	0.06†	0.25‡	–
10 kw, 1.27 cm/sec (on-focus)	0.35‡	0.35‡	0.20‡
5 kw, 0.423 cm/sec (off-focus)	–	0.06†	–
10 kw, 0.423 cm/sec (off-focus)	0.125‡	0.15‡	–

† : Surface heat flux model.
‡ : Internal heat source model

5.6.3 Prediction of Local Solidification Times

The finite element program THERM predicts the temperatures at all the nodes for successive time steps, and from these temperature histories, the thermal gradients and the local cooling rates are determined. The model was used to predict the local solidification times in keyhole laser welds in aluminum alloys. Local solidification times and thereby the solidification rates significantly influence the weld metal microstructure and the solidification morphology. The dendrite arm spacings are an important characteristic of the weld metal and effect its mechanical properties – in general, the finer the spacings , the better the strength and toughness. The primary dendrite arm spacing is inversely proportional to square root of the thermal gradient, whereas the secondary arm spacings are directly proportional to the local solidification times.[83] Considerable

experimental data exists for the aluminum - 4.5% copper system which shows that the secondary dendrite arm spacing and the local solidification time follow the empirical relation[84]

$$d = 7.5\Theta^{0.39} \tag{5.1}$$

where d is the secondary dendrite arm spacing in microns, and Θ the local solidification time in seconds.

Table 5.9. Solidification time in on-focus laser weld in alloy 2219.

(10 kw, 0.847 cm/sec)

Node #	X mm	Y mm	Sol. Time sec.	Predicted Spacing, μ	Measured Spacing, μ
12	0.0	5.8	0.4053	5.27	6.56
112	3.3	4.3	0.3603	5.03	6.35
123	5.8	3.5	0.3159	4.77	5.98

Table 5.9 shows the experimentally determined arm spacing at three locations in a 10 kw, 0.847 cm/sec on-focus laser weld in alloy 2219. Also shown are the calculated secondary dendrite arm spacings using equation 5.1 and the solidification times predicted by THERM. The predicted arm spacings are in good agreement with the experimentally measured values.

Chapter 6

CONCLUSIONS

The main objective of the investigation was to understand the influence of laser welding parameters on the weld characteristics in aluminum alloys 2219, 5083, 5456 and 6061. The investigation consisted of an experimental program to analyze the high power laser welds in aluminum alloys, and an analytical program for the thermal modeling of the melting and solidification phenomena in laser welds. The main conclusions of the investigation are as follows:

i. Weld penetration varied considerably among the four aluminum alloys investigated. Alloy 2219 showed the smallest weld penetration and the 5xxx series alloys the largest for similar welding condition. Presence of volatile alloying elements like magnesium in the 5xxx alloys alloys results in a higher vapor pressure, and consequently in deeper vapor columns or keyholes. In addition, the laser welds in aluminum alloys exhibited large bead widths owing to the high thermal diffusivity as well as the lower enthalpy per unit volume. The overall process efficiency determined from the weld cross-sectional areas also showed a wide variation among the alloys investigated. The highest process efficiency of over 33% was observed in 10 kw laser welds in alloy 5456. However, the process efficiency for alloy 2219 was only about 24% for similar welding conditions. Conduction mode welds had efficiency values under 5%. The overall process efficiency calculated from the experimentally determined weld areas is directly related to the amount of laser energy absorbed by the material during the welding cycle.

ii. The 5xxx series alloys showed a cyclic variation in the weld penetration along the weld travel direction. Up to 15% variation in penetration was observed

150

with a frequency of about 4 to 6 hz evidently caused by an unstable and oscillating keyhole. Violent eruptions occurred during the welding cycle due to the frequent collapse of the keyhole and the weld surface often exhibited open cavities.

iii. The laser welds in aluminum alloys were characterized for the nature and amount of porosity present in the welds in terms of the welding parameters and alloying content. Conduction mode welds were generally free from porosity or shrinkage cavities. The volume of porosity was the highest for the 5xxx alloys, and generally decreased with increasing welding speed. In the keyhole welds, the magnesium containing alloys 5xxx exhibited a large amount of spherical porosity of up to 0.4 cm diameter. The, larger spherical pores were usually clustered near the top of the welds. Further, laser welds ion these alloys also contained large cavities in the weld. These cavities are caused by the entrapment of parts of the unstable cavity as it oscillates between maximum depth and collapse. Alloys 2219 and 6061 did not exhibit any spherical pores, but did contain occasional large shrinkage cavities. No secondary interdendritic porosity was found in any of the welds.

iv. Loss of elements from the keyhole laser welds were determined by the electron microprobe analyzer. Aluminum was the main specie vaporized during laser welding of alloy 2219. Percentage loss of aluminum from the weld was related to the amount of porosity or shrinkage cavities present in the welds. In alloys 5xxx, both aluminum and magnesium were the dominant vaporizing species. However, no direct correlation between % loss of aluminum or magnesium and the amount of porosity measured could be established. The large amount of spherical porosity observed in these alloys is associated with the boiling of magnesium from the weld metal, and the subsequent entrapment of the

bubbles. The large solidification range in the aluminum alloys results in a large mushy zone during solidification, increasing the probability of bubble entrapment.

v. A two-dimensional nonlinear finite element model was developed to analyze the transient heat flow in welding. The model was tested for stability and accuracy by solving numerous heat-conduction problems involving phase change. The results predicted by the numerical model THERM were in good agreement with the relevant published experimental and/or analytical results.

vi. The heat transfer model was used to simulate the melting and solidification phenomenon occurring in keyhole laser welds. The weld bead shape and dimensions predicted by the model are in good agreement with the experimental results. The model was used to predict the three-dimensional shape of the weld pool, and the shape of the large mushy zone that results during the solidification of laser welds in aluminum alloys.

vii. The model was also used to predict the local solidification rates and times in the weld. The solidification times at specific locations in the weld zone were correlated with the secondary dendrite arm spacings in the weld microstructure. The predicted dendrite arm spacings were in good agreement with the experimentally measured values.

REFERENCES

1. Hanson, R.C. 1985. A Comparison of High Energy Beam Systems – Electron Beam/Laser Beam. *Proc. of conf. on The Laser vs. the Electron Beam in Welding, Cutting and Surface Treatment*, pp. 255, Bakish Materials Corporation, Englewood, NJ.

2. Quigley, M.B.C. 1986. High Power Density Welding. *The Physics of Welding*, 2nd ed., pp. 306-329, IIW, Pergamon Press, NY.

3. Breinan, E.M., Banas, C.M., and Greenfield, M.A. 1981. Laser Welding – The Present State-of-the-Art. *Source Book of Electron Beam & Laser Welding*, pp. 247, ASM, Metals Park, OH.

4. Ready, J.F. 1978. *Industrial Applications of Lasers.* Academic Press, NY.

5. Duley, W.W. 1976. *CO_2 Lasers, Effects & Applications*, Academic Press, NY.

6. Duley, W.W. 1983. *Laser Processing & Analysis of Materials*, Plenum Press, NY.

7. Devletian, J.H., and Wood, W.E. 1983. *Factors Affecting Porosity in Aluminum Welds – A Review*, WRC Bulletin 290, Welding Research Council, NY.

8. American Welding Society. 1982. *Metals and their Weldability.*, Welding Handbook, vol. 4, 7th ed., AWS.

9. Snow, D.B., and Breinan, E.M. 1978. *Evaluation of Basic Laser Welding Capabilities.* United Tech. Research Center Report R78-911989-14.

10. Snow, D.B., Kaufman, M.J., Banas, C.M., and Breinan, E.M. 1979. *Evaluation of Basic Laser Welding Capabilities.* United Tech. Research Center Report R79-911989-17.

11. Moon, D.W., and Metzbower, E.A. 1983. Laser Beam Welding of Aluminum Alloy 5456. *Welding Journal*, 62(2):53-s to 58-s.

12. Oreper, G.M. and Szekely, J. 1984. Heat- and Fluid-flow Phenomena in Weld Pools. *J. Fluid. Mech*, 147:53-79.

13. Marcus, S., Lowder, J.E., and Mooney, D.L. 1976. Large Spot Thermal Coupling of CO_2 Laser Radiation to Metallic Surfaces. *J. Appl. Phys.*, 47(7):2966-2968.

14. Pavelic, V., Tanbakuchi, R., Uyehara, O.A., and Myers, P.S. 1969. Experimental and Computed Temperature Histories in Gas Tungsten-Arc Welding of Thin Plates. *Welding Journal*, 48(7):295-s to 305-s.

15. Tong, H., and Giedt, W.H. 1971. Depth of Penetration during Electron Beam Welding. *J. Heat Transfer*, 93(5):155-163.

16. Miyazaki, T., and Giedt, W.H. 1982. Heat Transfer from an Elliptical Cylinder Moving Through an Infinite Plate Applied to Electron Beam Welding. *Int. J. Heat Mass Transfer*, 25(6):807-814.

17. Mazumder, J., and Steen, W.M. 1980. Heat Transfer Model for CW Laser Material Processing. *J. Appl. Phys.*, 51(2):941-947.

18. Chande, T., and Mazumder, J. 1984. Estimating Effects of Processing Conditions and Variable Properties upon Pool Shape, Cooling Rates, and Absorption Coefficient in Laser Welding. *J. Appl. Phys.*, 56(7):1981-1986.

19. Goldak, J., Chakravarti, A., and Bibby, M. 1984. A New Finite Element Model for Welding Heat Sources. *Metall. Trans. B*, 15B(6):299-305.

20. Goldak, J., Bibby, M., Moore, J., House, R., and Patel, B. 1986. Computer Modeling of Heat Flow in Welds. *Metall. Trans. B*, 17B(9):587-600.

21. Ready, J.F. 1982. Material Processing – An Overview. *Proc. of the IEEE*, 70(6):533-544.

22. Huntington, C.A., and Eager, T.W. 1983. Laser Welding of Aluminum and Aluminum Alloys. *Welding Journal*, 62(4):105-s to 107-s.

23. Jergensen, M. 1980. Increasing Energy Absorption in Laser Welding. *Metal Construction*, (2):88.

24. McLachlan, A.D. 1986. Improved Coupling Coefficient of Laser Radiation to Aluminum by means of Absorptive Polymer Coatings. *J. Appl. Phys.*, 59(6):1829-1833.

25. Banas, C.M., and Webb, R. 1982. Macro-Materials Processing. *Proc. of the IEEE*, 70(6):556-565.

26. Lewis, G.K., and Dixon, R.D. 1985. Plasma Monitoring of Laser Beam Welds, *Welding Journal*, 64(2):49-s to 54-s.

27. Dixon, R.D., and Lewis, G.K. 1985. Electron Emission and Plasma Formation during Laser Beam Welding. *Welding Journal*, 64(3):71-s to 78-s.

28. Martukanitz, R.P. 1982. Sources of Porosity in Gas Metal Arc Welding of Aluminum. *Trends in Welding Research*, pp.315-330, ASM.

29. Andrew, R.C., and Chadwick, G.A. 1975. Source of Hydrogen Porosity in Aluminum Alloy Welds – A Literature Survey – AWRA Report P3-5-74. *Australian Welding Research*, pp. 1-19.

30. Talbot, D.E.J. 1975. Effects of Hydrogen in Aluminum. Magnesium, Copper, and Their Alloys. *Int. Metall. Reviews*, Review 201, 20:166-184.

31. Hatch, J.E. 1984. *Aluminum, Properties and Physical Metallurgy*, ASM.

32. Howden, D.G., and Milner, D.R. 1963. Hydrogen Absorption in Arc Welding. *Brit. Weld. J.*, 10(6):304-316.

33. Campbell, J. 1968. Pore Nucleation in Solidifying Metals. *The Solidification of Metals*, ISI Pub. # 110, pp. 18-26.

34. Grigorenko, G.M. 1970. Formation of Pores in Welds. *Avt. Svarka.*, 10:13-17.

35. Howden, D.G. 1971. An Up-to-Date Look at Porosity Formation in Aluminum Weldments. *Welding Journal*, 50(2):112-114.

36. Uda, M., and Ohno, S. 1974. Porosity Formation in Weld Metal – I. Effect of Hydrogen on Porosity Formation in Pure Aluminum At Non-Arc Melting. *Trans. National Res. Inst. for Metals*, 16(2):29-36.

37. Nikiforov, G.D., Trusov, S.A., and Silant'eva, S.A. 1980. The Redistribution of Hydrogen during the Solidification of Aluminum. *Svar. Proiz.*, 9:44-48.

38. D'Anessa, A.T. 1967. Microstructural Aspects of Weld Solidification. *Welding Journal*, 46(11):491s to 499s.

39. Opie, W.R., and Grant, N.J. 1950. Hydrogen Solubility in Aluminum and some Aluminum Alloys. *Trans. of AIME, J. of Metals*, 188(10):1237-1241.

40. Woods, R.A. 1974. Porosity and Hydrogen Absorption in Aluminum Welds. *Welding Journal*, 53(3):97s to 108s.

41. Chalmers, B. 1964. *Principles of Solidification.* John Wiley & Sons, NY.

42. Kubo, K., and Pehlke, R.D. 1985. Mathematical Modeling of Porosity Formation in Solidification. *Metall. Trans. B*, 16B(6):359-366.

43. American Society of Metals. 1983. *Welding, Brazing, and Soldering.* Metals Handbook, vol. 6, 9th ed., ASM.

44. Mazumder, J. 1982. Laser Welding: State of the Art Review. *J. Met.*, 34(7):16-24.

45. Block-Bolten, A., and Eager, T.W. 1982. Selective Evaporation of Metals from Weld Pools. *Trends in Welding Research*, , pp.53-73, ASM.

46. Khan, P.A.A., and DebRoy, T. 1984. Alloying Element Vaorization and Weld Pool Temperature during Laser Welding of AISI 202 Stainless Steel. *Metall. Trans. B*, 15B(12):641-644.

47. Schauer, D.A., Giedt, W.H., and Shintaku, S.M. 1978. Electron Beam Welding Cavity Temperature Distributions in Pure Metals and Alloys. *Welding Journal*, 57(5):127-s to 133-s.

48. Flemings, M.C. 1974. *Solidification Processing*. McGraw-Hill, New York.

49. Rosenthal, D. 1941. Mathematical Theory of Heat Distribution during Welding and Cutting. *Welding Journal*, 20(5):220-s to 234-s.

50. Myers, P.S., Uyehara, O.A., and Borman, G.L. 1967. *Fundamentals of Heat Flow in Welding*. WRC Bulletin 123, Welding Research Council, NY.

51. Christensen, N.,Davies, V. de L., and Gjermundsen, K. 1965. Distribution of Temperatures in Arc Welding. *Brit. Weld. J.*, 12(2):54-75.

52. Malmuth, N.D. 1976. Temperature Field of a Moving Point Source with Change of State. *Int. J. Heat Mass Transfer*, 19(4):349-354.

53. Trivedi, R., and Srinivasan, S.R. 1974. Temperature Distribution Around a Moving Cylindrical Source. *J. Heat Transfer*, 96(8):427-428.

54. Swift-Hook, D.T., and Gick, E.F. 1973. Penetration Welding with Lasers. *Welding Journal*, 52(11):492-s to 499-s.

55. Gray, W.H., Schnurr, N.M. 1975. A Comparison of the Finite Element and Finite Difference Methods for the Analysis of Steady Two Dimensional Heat Conduction Problems. *Comp. Methods in Appl. Mech. and Engn.*, 6:243-245.

56. Fujii, H. 1973. Some Remarks on Finite Element Analysis of Time-Dependent Field Problems. *Theory and Practice in Finite Element Structural Analysis*, Proc. of 1973 Tokyo Seminar on FE Analysis. Univ. of Tokyo Press.

57. Zienkiewicz, O.C., and Parekh, C.J. 1970. Transient Field Problems: Two-Dimensional Analysis by Isoparametric Finite Elements. *Int. J. of Num. Methods in EngN.*, 2:61-71.

58. Hsiao, J.S. 1985. An Efficient Algorithm for Finite-Difference Analysis of Heat Transfer with Melting and Solidification. *Num. Heat Transfer*, 8:653-666.

59. Friedman, E. 1974. *A Direct Iteration Method for the Incorporation of Phase Change in Finite Element Heat Conduction Programs*. AEC Research and Development Report WAPD-TM-1133.

60. Comini, G., Del Guidice, S., Lewis, R.W., and Zienkiewicz, O.C. 1974. Finite Element Solution of Non-Linear Heat Conduction Problems with Special Reference to Phase Change. *Int. J. for Num. Methods in Engn.*, 8:613-624.

61. Pham, Q.T. 1987. A Note on Some Finite-Difference Methods for Heat Conduction with Phase Change. *Num. Heat Transfer*, 11:353-359.

62. Myers, G.E. 1977. *Numerically Induced Oscillations and Stability Characteristics of Finite Element Solutions to Two-Dimensional Heat-Conduction Transients*. Engineering Experimentation Report No. 43, Univ. of Wisconsin.

63. Bathe, Klaus-Jürgen. 1982. *Finite Element Procedures in Engineering Analysis*. Prentice-Hall, NJ.

64. Wood, W.L., and Lewis, R.W. 1975. A Comparison of Time Marching Schemes for the Transient Heat Conduction Equation. *Int. J. for Num. Methods in Engn.*, 9:679-689.

65. Donea, J. 1974. On the Accuracy of Finite Element Solutions to the Transient Heat-Conduction Equation. *Int. J. for Num. Methods in Engn.*, 8:103-110.

66. Hultgren, R., Orr, R.L., Anderson, P.D., and Kelley, K.K. 1963. *Selected Values of Thermodynamic Properties of Metals and Alloys*. John Wiley and Sons, NY.

67. Dushman, S., and Lafferty, J.M. 1962. *Scientific Foundations of Vacuum Technique*. 2nd ed., John Wiley and Sons, NY.

68. Cobine, J.D., and Burger, E.E., 1955. Analysis of Electrode Phenomenon in the High-Current Arc. *J. Appl. Phys.*, 26(7):895-900.

69. Andersson, B. A. B. 1978. Thermal Stresses in a Submerged-Arc Welded Joint Considering Phase Transformations. *Trans. of ASME, J. of Engn. Matl. and Tech.*, 100(10):356-362.

70. Friedman, E. 1975. Thermomechanical Analysis of the Welding Process using the Finite Element Method. *Trans. of ASME, J. of Pressure Vessel Tech.*, (8):206-213.

71. Rao, S.S. 1982. *The Finite Element Method in Engineering*. Pergamon Press, NY.

72. Wilson, E.L., Bathe, K.J., and Peterson, F.E. 1974. Finite Element Analysis of Linear and Nonlinear Heat Transfer. *Nuclear Engn. and Design*, 29:110-124.

73. Bathe, Klaus-Jürgen, and Khoshgoftaar, M.R. 1979. Finite Element Formulation and Solution of Nonlinear Heat Transfer. *Nuclear Engn. and Design*, 51:389-401.

74. Weiner, J.H. 1955. Transient Heat Conduction in Multiphase Media. *Brit. J. Appl. Phys.*, 6(10):361-363.

75. Hibbitt, H.D., and Marcal, P.V. 1973. A Numerical, Thermo-Mechanical Model for the Welding and Subsequent Loading of a Fabricated Structure. *Comp. and Structures*, 3:1145-1174.

76. Lazardis, A. 1970. A Numerical Solution of the Multidimensional Solidification (or Melting) Problem. *Int. J. Heat Mass Transfer*, 13:1459-1477.

77. Friedman, E. Oct., 1987. Personal Communications.

78. Krutz, G.W., and Segerlind, L.J. 1978. Finite Element Analysis of Welded Structures. *Welding Journal*, 57(7):211s to 216s.

79. Chong, L.M. 1982. *Predicting Weld Hardness*. M. Eng. Thesis, Carleton Univ, Ottawa, Canada.

80. Locke, E., Hoag, E., and Hella, R. 1972. Deep Penetration Welding with High Power CO_2 Lasers. *Welding Journal*, 51(5):245-s to 249-s.

81. Touloukian, Y.S., and Ho, C.Y. 1973. *Properties of Aluminum and Aluminum Alloys*. Thermomechanical Properties Research Center, Purdue Univ., IN.

82. American Society of Metals. 1979. *Properties and Selection: Nonferrous Alloys and Pure Metals*. Metals Handbook, vol. 2, 9th ed., ASM.

83. Kurz, W., and Fisher, D.J. 1986. *Fundamentals of Solidification*. Trans Tech Publications, Switzerland.

84. American Society of Metals. 1985. *Metallography and Microstructures*. Metals Handbook, vol. 9, 9th ed., ASM.

APPENDIX

INPUT AND OUTPUT DATA FILES

To solve a transient heat conduction problem using THERM, two separate input data sets are required. The first called INPUT consists of a description of the overall problem and domain, the welding parameters including the terms describing the spatial distribution of the energy, and the material thermal properties. The second data set called MESH describes the finite element mesh used to discretise the domain being analysed. Following sections briefly describe each of these data sets.

INPUT

A sample INPUT file for a 10 kw, 1.27 cm/sec (30 ipm), on-focus laser weld in alloy 2219 is shown below.

```
      136        170       2000         10          0
        5          2          1          1          0
 2219.000  10000.000      1.270      0.000      0.350
    1.270      1.000      0.040     -0.040      0.040
  0.00050    0.00100    2.00000  300.00000  300.00000
  816.000    916.000   1015.750      0.150      4.000
        4          5          1
  273.000      1.170
  323.000      1.280
  816.000      1.840
  916.000      1.963
  300.000      2.426
  366.000      2.576
  589.000      2.908
  816.000      3.515
  916.000      3.783
  300.000      0.000
    0.000
```

Each line in the above example is described in the following paragraphs and tables.

Line 1 (Format 5I10)

Item	Name	Description
1	NELEM	# of elements
2	NNODE	# of nodes
3	NTIMES	# of time steps to be analysed
4	NPRINT	Freq. at which output is reqd.
5	NCHECK	0 : Actual run; 1 : Check input

Line 2 (Format 5I10)

Item	Name	Description
1	NITER	Max # of iterations/timestep
2	NG	# of gauss integration points
3	NMATL	# of materials in the domain
4	NLUMP	0 : Consistent C; 1 : Lumped C
5	NBATCH	0 : Batch run; 1 : Interactive run

Line 3 (Format 5F10.3)

Item	Name	Description
1	ALLOY	Alloy identification
2	POWER	Welding heat input
3	SPEED	Welding travel speed
4	FOCUS	Location of focus
5	EFF	Absorptivity

Line 4 (Format 5F10.3)

Item	Name	Description
1	YMAX	Plate thickness
2	Y0	Effective depth of internal heat source
3	R0	Effective radius of heat source
4	ZARC	Location of energy source at start
5	ZEND	Location of energy source at end

Line 5 (Format 5F10.5)

Item	Name	Description
1	DELT1	Initial time increment
2	DELT2	Time increment after melting
3	CONVCR	Criteria for convergence test
4	TINIT	Initial Temperature
5	TAMB	Ambient Temperature

Line 6 (Format 5F10.3)

Item	Name	Description
1	TS	Solidus temperature
2	TL	Liquidus temperature
3	HLAT	Latent Heat; 0 for enthalpy method
4	EMISS	Emissivity for radiation loss
5	CMULTP	Multiplier for ther. cond. in liquid

Line 7 (Format 3I10)

Item	Name	Description
1	N(1)	# of temp. where ther. cond. is declared
2	N(2)	# of temp. where sp. heat is declared
3	N(3)	# of temp. where enthalpy is declared

Line 8 Onwards

Next few lines declare the thermal conductivity, volumetric specific heat and the enthalpy at N(1), N(2) and N(3) temperatures respectively. Also, line 7 through end are repeated NMATL times for each material in the domain.

MESH

An example of the MESH file used for the finite element mesh shown in figure 5.33 is listed at the end of this section. The first set of lines (Format 15I5) describe the nodal connectivity array for each of the elements. Item 1 is the element number. Wherever similar patterns of elements exist, node numbers and other characteristics of the element are generated. For instance, based on the values in lines 5 and 6 for elements 5 and 37 respectively, the node numbers etc. for elements 5, 9, 13, 17, ..., and 37 are generated – item 2 defines the increment in element numbers NDIFF.

Item 3 in these lines defines NE for each element which identifies any edge in the quadrilateral element which lies on the surface. This is required for calculating the convective and radiation losses from the element surface.

NE	Description
1	Edge connecting nodes 1 and 2
2	Edge connecting nodes 2 and 3
3	Edge connecting nodes 3 and 4
4	Edge connecting nodes 4 and 1

Item 4 defines IMATL which identifies the element to a material number in order to use the associated material properties. Item 5 gives the number of nodes (4 to 8) being used in the particular element, and item 6 to last give the associated elemental node numbers.

In the second set of lines, the nodal coordinates (x and y) are listed (Format 2I5, 2F10.5). Again, the coordinates may be generated if a repeating pattern occurs in the mesh using NDIFF - the node numbers increment in the pattern.

```
 1    0    2    1    4    19    1    2    20
 2    0    2    1    4    38   19   20    39
 3    0    2    1    4    58   38   39    59
 4    0    2    1    4    78   58   59    79
 5    0    0    1    4    20    2    3    21
37    4    0    1    4    28   10   11    29
 6    0    0    1    4    39   20   21    40
34    4    0    1    4    46   27   23    47
 7    0    0    1    4    59   39   40    60
31    4    0    1    4    65   45   46    66
 8    0    0    1    4    79   59   60    80
28    4    0    1    4    84   64   65    85
32    0    0    1    4    85   65   66    67
35    0    0    1    4    66   46   47    48
36    0    0    1    4    67   66   48    68
38    0    0    1    4    47   28   29    30
39    0    0    1    4    48   47   30    49
40    0    0    1    4    68   48   49    50
41    0    0    1    5    30   11   12    31   29
42    0    0    1    5    50   30   31    51   49
43    0    0    1    4    31   12   13    32
53    2    0    1    4    36   17   18    37
44    0    0    1    4    51   31   32    52
54    2    0    1    4    56   36   37    57
55    0    1    1    5    78   80   87    86   79
56    0    0    1    5    80   82   88    87   81
57    0    0    1    4    88   82   83    89
59    1    0    1    4    90   84   85    91
60    0    0    1    4    91   85   67    92
```

61	0	0	1	4	92	67	68	69	
62	0	0	1	4	69	68	69	70	
63	0	0	1	4	70	68	69	71	
69	0	0	1	4	75	86	87	77	
70	0	0	1	4	93	86	87	94	
71	0	0	1	4	94	87	88	95	
75	0	0	1	4	98	91	92	99	
76	0	0	1	4	99	92	69	100	
77	0	0	1	4	100	69	70	101	
84	0	0	1	4	107	76	77	108	
85	0	1	1	5	93	95	110	109	94
86	0	0	1	5	95	97	111	110	96
87	0	0	1	5	97	99	112	111	98
88	0	0	1	5	99	101	113	112	100
89	0	0	1	5	101	103	114	113	102
90	0	0	1	4	114	103	104	115	
94	0	0	1	4	118	107	108	119	
95	0	2	1	4	120	109	110	121	
96	0	0	1	4	121	110	111	122	
104	0	0	1	4	129	118	119	130	
105	0	1	1	5	120	122	132	131	121
106	0	0	1	5	122	124	133	132	123
107	0	0	1	5	124	126	134	133	125
108	0	0	1	5	125	128	135	134	127
109	0	0	1	5	128	130	136	135	129
110	0	2	1	4	137	131	132	138	
125	5	2	1	4	155	149	150	156	
111	0	0	1	4	138	132	133	139	
114	0	0	1	4	141	135	136	142	
116	0	0	1	4	144	138	139	145	
119	0	0	1	4	147	141	142	148	
121	0	0	1	4	150	144	145	151	
124	0	0	1	4	153	147	148	154	
126	0	0	1	5	150	152	157	156	151
127	0	0	1	5	152	154	158	157	153
128	0	2	1	4	159	155	156	160	
134	3	2	1	4	167	163	164	168	
129	0	0	1	4	160	156	157	161	
135	3	0	1	4	168	164	165	169	
130	3	0	1	4	161	157	158	162	
136	3	0	1	4	169	165	166	170	
1	0	0.00000	1.27000						
5	0	0.00000	1.14300						
6	0	0.00000	1.07950						
12	0	0.00000	0.69850						
13	0	0.00000	0.63500						
18	0	0.00000	0.00000						
19	0	0.02000	1.27000						
23	0	0.02000	1.14300						
24	0	0.02000	1.07950						
29	0	0.02000	0.76200						
30	0	0.04000	0.76200						
32	0	0.04000	0.63500						
33	0	0.04000	0.50800						
37	0	0.04000	0.00000						
38	0	0.04000	1.27000						
42	0	0.04000	1.14300						
43	0	0.04000	1.07950						
47	0	0.04000	0.82550						
48	0	0.06000	0.82550						
49	0	0.06000	0.76200						
50	0	0.08000	0.76200						

52	1	0.08000	0.63500
53	0	0.08000	0.50800
57	1	0.08000	0.00000
58	0	0.06000	1.27000
62	1	0.06000	1.14300
63	0	0.06000	1.07950
66	1	0.06000	0.88900
67	0	0.08000	0.88900
68	0	0.08000	0.82550
69	0	0.12000	0.82550
72	1	0.12000	0.63500
73	0	0.12000	0.50800
77	1	0.12000	0.00000
78	0	0.08000	1.27000
82	1	0.08000	1.14300
83	0	0.08000	1.07950
85	1	0.08000	0.95250
86	0	0.12000	1.27000
92	1	0.12000	0.88900
93	0	0.16000	1.27000
103	1	0.16000	0.63500
104	0	0.16000	0.50800
108	1	0.16000	0.00000
109	0	0.28000	1.27000
119	1	0.28000	0.00000
120	0	0.40000	1.27000
130	1	0.40000	0.00000
131	0	0.60000	1.27000
136	1	0.60000	0.00000
137	0	0.80000	1.27000
142	1	0.80000	0.00000
143	0	1.00000	1.27000
148	1	1.00000	0.00000
149	0	2.00000	1.27000
154	1	2.00000	0.00000
155	0	4.00000	1.27000
167	4	10.00000	1.27000
156	0	4.00000	1.01600
168	4	10.00000	1.01600
157	0	4.00000	0.50800
169	4	10.00000	0.50800
158	0	4.00000	0.00000
170	4	10.00000	0.00000

OUTPUT

The OUTPUT data file prints the nodal temperatures at a frequency of NPRINT timesteps. From the temperature histories, cooling rates, solidification times, and thermal gradients are easily calculated.